

**EFFECT OF INTERFACE CHEMICAL COMPOSITION ON THE HIGH
STRAIN RATE DEPENDENT MECHANICAL BEHAVIOR OF AN
ENERGETIC MATERIAL**

by

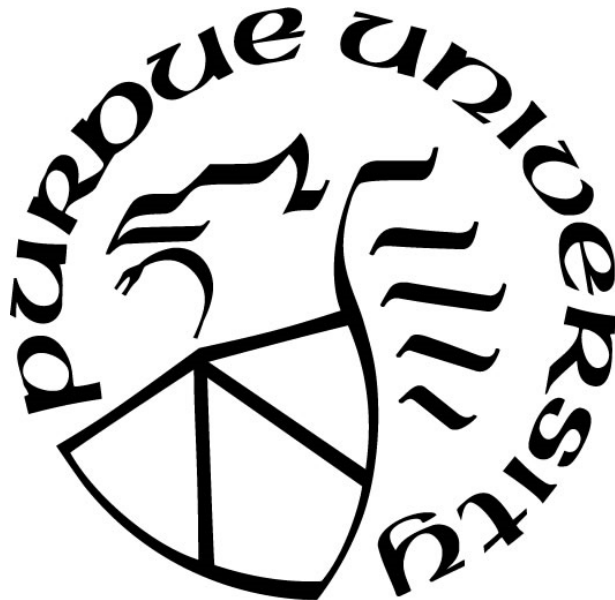
Chandra Prakash

A Dissertation

Submitted to the Faculty of Purdue University

In Partial Fulfillment of the Requirements for the degree of

Doctor of Philosophy



School of Aeronautics & Astronautics

West Lafayette, Indiana

December 2018

**THE PURDUE UNIVERSITY GRADUATE SCHOOL
STATEMENT OF COMMITTEE APPROVAL**

Dr. Vikas Tomar, Co-Chair

School of Aeronautics and Astronautics

Dr. Ibrahim E. Gunduz, Co-Chair

School of Mechanical Engineering

Dr. Jeffrey F. Rhoads

School of Mechanical Engineering

Dr. Marcial Gonzalez

School of Mechanical Engineering

Approved by:

Dr. Weinong Chen

Head of the Graduate Program

*Dedicated to
my parents
and my brother*

ACKNOWLEDGMENTS

First and foremost I would like to thank Dr. Vikas Tomar and Dr. I. E. Gunduz for their continuous guidance and support through this research. It has been an honor for me to work with them as a Ph.D. student.

Prof. Tomar is not only an outstanding mentor but a truly inspirational human being. His patience, adamant work ethic and inspiring nature have been a great source of motivation throughout my doctoral research. I cannot thank him enough for all of the positive things he has instilled into me to help me grow and prosper in the future.

I am also thankful to Dr. Gunduz for his continued support throughout my PhD. He has personally guided me through the extremely time consuming experimental processes. I have been extremely lucky to have him as one of my supervisors who cared so much about my work.

I would also like to sincerely thank Dr. Jeffrey F. Rhoads and Dr. Marcial Gonzalez for consenting to serve as my committee members. A special thanks to Dr. Rhoads and Dr. Gonzalez for their critical assessment of my work during the preliminary examination, which helped me tremendously in improving my research.

The help and encouragement from my friends and colleagues are greatly appreciated. I would like to thank all of my past and current lab mates in the Interfacial Multiphysics Laboratory: Devendra Verma, Tao Qu, Yang Zhang, Sudipta Biswas, Maithilee Motlag, Debapriya Pinaki, Hao Wang, Bing Li, Vikas Yettela, Abhijeet Dhiman and Ayotomi Olokun. The time spent with everyone made it an incredible experience, and provided me with many great friendships. I would also like to thank Devendra Verma for his special help in explaining experimental setups. In addition, I would also like to thank all of the faculty and staff in the School of Aeronautics and Astronautics at Purdue.

Financial support from the Air Force Office of Scientific Research, Dynamic Materials and Interactions program (Grant No.: FA9550-15-1-0202, Program Manager: Dr. Martin Schmidt) is greatly appreciated.

Last but not least, I would like to thank my mother, my father, and my brother for their understanding, love and moral support.

TABLE OF CONTENTS

TABLE OF CONTENTS.....	6
LIST OF TABLES.....	8
LIST OF FIGURES	9
ABSTRACT.....	13
INTRODUCTION	15
CHAPTER 1. EFFECT OF INTERFACE CHEMISTRY AND STRAIN RATE ON PARTICLE-MATRIX DELAMINATION IN AN ENERGETIC MATERIAL.....	17
1.1 Introduction.....	19
1.2 Experimental Methods.....	21
1.2.1 A Dynamic Impact Experiment Setup for Rate Dependent Property Measurements	22
1.2.1.1 Fitting a Viscoplastic Constitutive Model to Dynamic Impact Experiment Data	26
1.2.2 Mechanical Raman Spectroscopy Measurements of Interface Decohesion	29
1.2.2.1 Cohesive Finite Element Method Framework.....	31
1.3 Results And Analyses	34
1.3.1 Viscoplastic Model Parameters Measured using the Dynamic Impact Experiment..	34
1.3.2 Interface Separation Parameters Measured using MRS	39
1.3.3 Validation of Constitutive and Cohesive Parameters	42
1.3.4 Prediction of Interface Property Influence on High Rate Deformation Behavior	45
1.4 Conclusions.....	53
CHAPTER 2. EXPERIMENTAL INTERFACE SHOCK VISCOSITY MEASUREMENT IN AN ENERGETIC MATERIAL USING PULSE LASER INDUCED PARTICLE IMPACT LOADING COMBINED WITH MECHANICAL RAMAN SPECTROSCOPY	63
2.1 Introduction.....	65
2.2 Experimental Methods	67
2.3 Cohesive Finite Element Method Framework	70
2.3.1 Viscoplastic Constitutive Model.....	73
2.4 CFEM Model Validation and Rise Time Prediction As a Function of Impact Position...	75
2.4.1 Shock Compression Model Validation.....	76
2.4.2 Interface Shock Wave Rise Time Prediction.....	78

2.5	Interface Shock Viscosity Measurement and its Effect on the Interface Rise time.....	85
2.5.1	Experimental Measurement of Interface Shock Viscosity	85
2.5.2	Effect of Interface Shock Viscosity.....	91
2.6	Conclusions.....	93
CHAPTER 3. THE EFFECT OF INTERFACE SHOCK VISCOSITY ON THE STRAIN RATE INDUCED TEMPERATURE RISE IN AN ENERGETIC MATERIAL ANALYZED USING THE COHESIVE FINITE ELEMENT METHOD.....		101
3.1	Introduction.....	103
3.2	Experimental Methods.....	106
3.2.1	Constitutive Model for HTPB, AP and Interface	106
3.2.2	Cohesive Zone Model Parameters for HTPB-AP Interface	107
3.2.3	Shock Viscosity for HTPB-AP Interface.....	107
3.2.4	Thermal Conductivity for HTPB-AP Interface	108
3.3	Cohesive Finite Element Method Framework	110
3.4	Results and Analysis.....	113
3.4.1	Experimental Measurement of Thermal Conductivity	113
3.4.2	Numerical Simulation of Shock Behavior of HTPB-AP Energetic Material	116
3.5	Conclusions.....	131
CHAPTER 4. CONCLUSION.....		138
CHAPTER 5. FUTURE WORK.....		143
PUBLICATIONS.....		145

LIST OF TABLES

Table 1 Viscoplastic model parameters for AP, HTPB and the HTPB/AP interface.	37
Table 2 Cohesive zone parameters for the constituents of the HTPB/AP composite obtained using MRS.....	42
Table 3 Cohesive zone parameters for constituents of HTPB-AP composite for dynamic simulation.	52
Table 4 Constitutive model parameters for bulk and interface obtained from nanoscale dynamic impact experiment [36].....	69
Table 5 Cohesive zone model parameters for bulk and interface obtained from MRS experiment [36]	70
Table 6 Parameters used for Mie-Gruneisen equation of state [31]	76
Table 7 Constitutive model parameters for bulk and interface [18]	106
Table 8 Cohesive zone model parameters for bulk and interface [18]	107
Table 9 Shock viscosity of the HTPB, AP and HTPB-AP interface (Sample 1 is without Binding Agent and Sample 2 is with Binding Agent: Tepanol).....	108
Table 10 Mie-Gruneisen parameters for bulk HTPB and AP [47].	112
Table 11 Thermal properties of HTPB, AP and the HTPB-AP Interface.....	116

LIST OF FIGURES

Figure 1 Nanoscale dynamic impact experimental setup.	23
Figure 2 Representative depth versus time obtained from dynamic impact experiment and calculated velocity versus time data.	24
Figure 3 (a) A typical Raman spectra observed in an AP-HTPB sample of type 1 and (b) the corresponding stress versus shift calibration curve.	31
Figure 4 (a) Finite element mesh used and (b) mesh convergence analysis.	32
Figure 5 (a) log-log plot for the viscoplastic parameters and (b) stress-strain curve-fitting using the power law model for HTPB binder in the case of the HTPB-AP sample as a function of strain rate and (c) fitted curve with the current model to the experimental stress-strain data for HTPB obtained from an Split-Hopkinson pressure bar (SHPB) test performed by Cady and co-workers [88].	36
Figure 6 Stress-strain response of (a) AP phase and (b) AP-HTPB Interface in HTPB-AP sample as a function of strain rate.	37
Figure 7 Stress-strain model fitted to the dynamic impact experiment data for (a) HTPB binder, (b) HTPB-AP Interface, and (c) AP phase for different sample types. Sample 1 is without Tepanol and Sample 2 is with Tepanol.	38
Figure 8 (a) Schematic of dynamic impact finite element model, (b) impact velocity (from experiment), (c) spherical Impactor profile and (d) comparison of depth-time output obtained from experiment (sample type 1) and simulation.	39
Figure 9 (a) Sample configuration used for the MRS based measurements of interface delamination, (b) sample dimensions and (c) the load-displacement curve obtained during loading for HTPB-AP-Tepanol (type 2) sample (shaded area shows energy spent in the observed crack extension).	40
Figure 10 Stress distribution around the HTPB-AP interface for different load until failure for HTPB-AP-Tepanol (type 2) sample. Red dots are the positions where Raman spectra are recorded.	41
Figure 11 Stress distribution around the interface at different load for sample type 2.	43
Figure 12 (a) A schematic of the finite element model used in simulation and (b) comparison of load-displacement curve with that obtained from experiment for HTPB-AP-Tepanol sample.	44
Figure 13 A comparison of stress contour obtained from (a) finite element simulation and (b) from MRS for HTPB-AP-Tepanol (type 2) sample.	45

Figure 14 Kolsky bar simulation sample and load-profile [47] used in experiments.....	46
Figure 15 Interface separation evolution in the (a) Kolsky bar tension experiment [47] and (b) in the simulation as a function of time (sample type 1).	47
Figure 16 Validation of delamination mode obtained using CFEM with quasi-static experimental measurements (sample type 1).	48
Figure 17 (a) Cohesive energy and (b) cohesive energy at failure with time for different strain rates (sample type 1) predicted using CFEM simulation.....	49
Figure 18 (a) HTPB-AP sample (type 1) tensile model for dynamic failure simulation and delamination mode at time $t = 0.4 \mu\text{s}$ for strain rates of (b) 800 s-1 (c) 1000 s-1 (d) 2000 s-1 (e) 3000 s-1. IFAIL is the damage parameter used to represent fracture with a value of 1 indicating full separation and a value of 0 no separation [74].....	50
Figure 19 Stress contour for sample type 1 at strain rates (a) 800 s-1 (b) 1000 s-1 (c) 2000 s-1 (d) 3000 s-1 at time $t = 0.4 \mu\text{s}$. (First row- normal stress and Second row- shear stress)51	
Figure 20 (a) Cohesive energy with time and (b) cohesive energy near the initiation of delamination for different cohesive strengths predicted using CFEM simulation.....	52
Figure 21 Effect of the (a) cohesive strength and (b) strain rate on the initiation time of delamination predicted using CFEM simulation.....	53
Figure 22 (a) Finite element mesh of a single particle AP-HTPB impact model and (b) mesh convergence analysis and (c) the element deformation near the interface at a strain rate of 105 s-1 at $0.5 \mu\text{s}$	72
Figure 23 (a) Shock compression model and (b) comparison of the Hugoniot-curve obtained from experiment (Boteler et al., 1996) [25] and CFEM simulation.....	77
Figure 24 Stress-strain rate relation for AP	78
Figure 25 A single particle impact model for shock Hugoniot prediction with (a) a flat punch impact at the particle, (b) a flat punch impact at the interface, and (c) a flyer plate impact.	79
Figure 26 Shock stress wave profile for a strain rate of 1000 s-1 for (a) a flat punch impact at the particle, (b) a flat punch impact at the interface, and (c) a flyer plate impact.....	79
Figure 27 Shock pressure profile at the HTPB-AP interface at different time steps (0.01 μs -0.12 μs) with an impact velocity of 300 m/s for (a) a flat punch impact at the particle, (b) a flat punch impact at the interface, and (c) a flyer plate impact.	80
Figure 28 Interface particle velocity profile at the HTPB-AP interface at different time steps (0.01 μs -0.12 μs) with an impact velocity of 300 m/s for (a) a flat punch impact at the particle, (b) a flat punch impact at the interface, and (c) a flyer plate impact.....	81

Figure 29 (a) A representative interface particle velocity at different applied strain rates and (b) shock wave rise time as a function of applied strain rate for flyer-plate impact on an HTPB-AP sample.	82
Figure 30 (a) Shock velocity as a function of the impact velocity and (b) shock pressure as a function of impact velocity as a function of impact position analyzed earlier in Fig. 4.	83
Figure 31 Shock wave rise time as a function of (a) cohesive strength and (b) strain rate as a function of impact position analyzed earlier in Fig. 4.	84
Figure 32 Experimental Setup for shock viscosity measurement. (a) Streak camera, delay generator and CMOS camera used for particle velocity measurement, (b) a combined pulse laser and MRS setup used for stress measurement and (c) a representative sample used in the particle impact experiment.	85
Figure 33 (a) Schematic of pulse laser induced particle impact and velocity measurement, (b) streak images and (c) velocity measurement from the streak images.	87
Figure 34 (a) Representative HTPB-AP impact sample, (b) particle velocity and strain rate at different pulse energy, (c) Stress obtained in the scan area using MRS and (d) shock viscosity in the scan area for HTPB-AP-Tepanol sample. Red dots are the positions where Raman spectra were recorded.	88
Figure 35 A qualitative comparison of (a) the interface shock viscosity measured using the current experimental setup for both samples (Sample 1 is without Tepanol and Sample 2 is with Tepanol) and (b) the shock viscosity for Al determined using the wave profile data obtained from VISAR (Reprinted with permission from [22]. Copyright (2018) AIP Publishing).	89
Figure 36 Single particle finite element model and corresponding mesh for the impact simulation.	91
Figure 37 Shock pressure history at the interface as a function of (a) shock viscosity and (b) strain rate.	92
Figure 38 Shockwave rise time at the interface as a function of (a) shock viscosity at a constant strain rate of $100,000 \text{ s}^{-1}$ and (b) strain rate at a constant shock viscosity of $6 \text{ Pa}\cdot\text{s}$	93
Figure 39 (a) Experimental set-up for Raman shift versus temperature change calibration, (b) a representative Raman spectra of HTPB and (c) calibration curve for Raman shift versus Temperature change.	110
Figure 40 The finite element model of HTPB-AP microstructure (50% AP density) showing boundary conditions, and the mesh details as well as cohesive surfaces.	111

- Figure 41 (a) HTPB-AP tensile sample, (b) sample dimensions, boundary conditions and the scan area and (c) thermal conductivity near the HTPB-AP-Tepanol interface. Red dots are the position where Raman spectra were recorded. 115
- Figure 42 Pressure map in the HTPB-AP microstructure (for loading conditions shown in Fig. 2) at time (a) 0.001 μs , (b) 0.002 μs , (c) 0.004 μs and (d) 0.006 μs 117
- Figure 43 Normal stress profile in the microstructure along a selected cross-section at two different time steps..... 118
- Figure 44 Normal stress distribution in the (a) microstructure at the HTPB-AP interface near position A shown in Fig. 5, (b) HTPB, (c) AP and (d) the HTPB-AP interface at $t = 0.006 \mu\text{s}$ 119
- Figure 45 Shear stress distribution in the HTPB-AP microstructure at time (a) 0.001 μs , (b) 0.002 μs , (c) 0.004 μs and (d) 0.006 μs 120
- Figure 46 Shear stress distribution in the (a) microstructure at the HTPB-AP interface near position A shown in Fig. 43, (b) HTPB, (c) AP and (d) the HTPB-AP interface at 0.006 μs 121
- Figure 47 Effective viscoplastic strain distribution in the (a) microstructure at the HTPB-AP interface near position A shown in Fig. 43, (b) HTPB, (c) AP and (d) the HTPB-AP interface at 0.006 μs 122
- Figure 48 Temperature distribution in the HTPB-AP microstructure at (a) 0.001 μs , (b) 0.002 μs , (c) 0.004 μs and (d) 0.006 μs 123
- Figure 49 (a) Effective normal compressive stress and (b) effective shear stress history as a function of shock viscosity in the HTPB-AP microstructure..... 124
- Figure 50 Normal stress (a, b, c) and shear stress (d, e, f) history in HTPB, AP and HTPB-AP interface phase as a function of interface shock viscosity..... 125
- Figure 51 (a) HTPB-AP microstructure, (b) normal stress, (c) shear stress and (d) temperature profile as a function of interface shock viscosity along the selected cross-section at $t = 0.006 \mu\text{s}$ 127
- Figure 52 (a) Viscoplastic and (b) frictional energy dissipation history in the HTPB-AP microstructure as a function of interface shock viscosity. 128
- Figure 53 (a) Maximum temperature in the microstructure and (b) the hot-spot density history as a function of interface shock viscosity..... 129
- Figure 54 (a) Plastic dissipation energy, (b) maximum temperature and (b) the hot-spot density in the HTPB-AP microstructure at $t = 0.01 \mu\text{s}$ as a function of interface shock viscosity. 130

ABSTRACT

Author: Prakash, Chandra. PhD

Institution: Purdue University

Degree Received: December 2018

Title: Effect of Interface Chemical Composition on High Strain Rate Dependent Mechanical Behavior of an Energetic Material

Committee Chair: Vikas Tomar and Ibrahim Emre Gunduz

A combined experimental and computational study has been performed in order to understand the effect of interface chemical composition on the shock induced mechanical behavior of an energetic material (EM) system consisting of Hydroxyl-Terminated Polybutadiene (HTPB) binder and an oxidizer, Ammonium Perchlorate (AP), particle embedded in the binder. The current study focuses on the effect of interface chemical composition between the HTPB binder material and the AP particles on the high strain rate mechanical behavior. The HTPB-AP interface chemical composition was changed by adding cyanoethylated polyamine (HX-878 or Tepanol) as a binding agent. A power law viscoplastic constitutive model was fitted to nanoscale impact based experimental stress-strain-strain rate data in order to obtain the constitutive behavior of the HTPB-AP interfaces, AP particle, and HTPB binder matrix. An *in-situ* mechanical Raman spectroscopy framework was used to analyze the effect of binding agent on cohesive separation properties of the HTPB-AP interfaces, AP particle, and HTPB binder matrix. In addition, a combined mechanical Raman spectroscopy and laser impact set up was used to study the effect of strain rate, as well as the interface chemical composition on the interface shock viscosity. Finally, high velocity strain rate impact simulations were performed using an explicit cohesive finite element method framework to predict the effect of strain rate, interface strength, interface friction, and

interface shock viscosity on possible strain rate dependent temperature rises at high strain rates approaching shock velocities.

A modified stress equation was used in the cohesive finite element framework in order to include the effect of shock viscosity on the shock wave rise time and shock pressure during impact loading with strain rates corresponding to shock impact velocities. It is shown that increasing the interface shock viscosity, which can be altered by changing the interface chemical composition, increases the shock wave rise time at the analyzed interfaces. It is shown that the interface shock viscosity also plays an important role in determining the temperature increase within the microstructure. Interface shock viscosity leads to a decrease in the overall density of the possible hot-spots which is caused by the increase in dissipation at the shock front. This increase in shock dissipation is accompanied by a decrease in the both the maximum temperature, as well as the plastic dissipation energy, within the microstructure during shock loading.

INTRODUCTION

Prediction of the impact induced temperature rise in a hydroxyl-terminated polybutadiene (HTPB) - Ammonium Perchlorate (AP) energetic material (EM) requires knowledge of several material models to simulate the deformation behavior, such as the relevant strain rate dependent constitutive model, fracture failure model, the shock viscosity at the HTPB-AP interface level, and various thermal properties. In this work, a combined computational and experimental study is performed to investigate the effect of interface chemical composition on high strain rate impact induced deformation and associated temperature rise behavior in a HTPB-AP EM. The aforementioned thermomechanical properties are measured experimentally. The HTPB-AP interface chemical composition was altered by adding cyanoethylated polyamine (HX-878 or Tepanol) as a binding agent. A cohesive finite element method (CFEM) based computational framework that incorporated experimental properties was used to simulate impact induced failure and associated temperature rise in an idealized HTPB-AP microstructure.

Chapter 1 details the experiments that were conducted on the HTPB-AP interfaces to obtain the constitutive and interface separation behavior with varying amount of binding agent Tepanol. Dynamic impact experiments were performed to obtain constitutive model for the HTPB phase, the AP phase, and the HTPB-AP interface with and without binding agent Tepanol. An in-situ mechanical Raman spectroscopy (MRS) setup was used to analyze the effect of Tepanol on interface level stress variation and the corresponding interface delamination strength and interface fracture energy. The measured cohesive separation parameters capture the effect of interface chemical composition variation.

Chapter 2 details an experimental method to measure HTPB-AP interface level shock viscosity with and without a binding agent. Shock induced material behavior of interfaces was

investigated. It was observed that in order to obtain the upper bound on interface shock viscosity, an in-situ measurement of interface level shock induced stress under direct interface impact can be performed. Based on this observation, a pulse laser induced particle impact experiment was setup in combination with in-situ MRS measurements. A high-speed streak camera was used to measure the particle velocity as particles impact the sample interface. In-situ MRS measurements were used to measure the stress at the material interface due to impact. It was shown that altering the interface chemical composition changes the interface shock viscosity which then leads to an increase in the shock wave rise time at the interface.

Chapter 3 details a Raman thermometry based technique to measure HTPB-AP interface thermal conductivity. The experimentally measured thermomechanical properties were then used in a CFEM framework to simulate local temperature rise in a HTPB-AP EM microstructure under shock induced impact. The effect of interface chemical composition, through a change in interface shock viscosity, on the deformation behavior and temperature rise was investigated. The increase in the interface shock viscosity led to a decrease in both viscoplastic and frictional dissipation. This resulted in a decrease in the maximum temperature in the investigated microstructure. HTPB-AP interface regions with high density of particles were found to be more susceptible to local temperature rise due to the presence of viscoplastic dissipation, as well as frictional heating. A power law relation for the decrease in viscoplastic energy dissipation, temperature rise, and the density of the local temperature rise with the interface shock viscosity was obtained.

Chapter 4 summarizes the key findings of this work.

CHAPTER 1.
EFFECT OF INTERFACE CHEMISTRY AND STRAIN RATE ON
PARTICLE-MATRIX DELAMINATION IN AN ENERGETIC
MATERIAL

Chandra Prakash^a, I. Emre Gunduz^b, Caglar Oskay^c, Vikas Tomar^{a,*}

^a School of Aeronautics and Astronautics, Purdue University-IN, 47907, USA

^b School of Mechanical Engineering, Purdue University-IN, 47907, USA

^c Civil and Environmental Engineering, Vanderbilt University-TN, 37235, USA

*Corresponding author, Phone: (765)-494-3006 Fax: (765) 494-0307 Email: tomar@purdue.edu

Published in Engineering Fracture Mechanics 191 (2018) 46–64.

<https://doi.org/10.1016/j.engfracmech.2018.01.010>

ABSTRACT

In this work, the interface mechanical strength of a set of Hydroxyl-terminated polybutadiene (HTPB)-Ammonium Perchlorate (AP) interfaces is characterized using dynamic microscale impact experiments at strain rates up to 100 s^{-1} . The experiments were conducted on the interfaces with varying amounts of the binding agent Tepanol with an impactor of radius $1 \text{ }\mu\text{m}$. Measurements of strain rates and plastic-residual depths were correlated to obtain the interface level strains and stresses. A power law viscoplastic constitutive model was fitted to the stress-strain-strain rate data in order to predict rate dependent constitutive behaviors of the interfaces, particle, and matrix. An *in-situ* mechanical Raman spectroscopy (MRS) setup was used to analyze the effect of binding agent on interface level stress variation at different temperatures. The MRS setup was also used to obtain cohesive fracture separation properties in the analyzed samples including interface delamination strength and interface fracture energy. The measured cohesive fracture parameters capture the effect of interface chemistry variation. The cohesive parameters and the viscoplastic model obtained from the experiment were implemented in a cohesive finite element scheme to simulate dynamic crack propagation, as well as delamination, in model energetic material samples. The presented results quantify the influence of the rate of loading and interface binding agent variation on rate dependent fracture. The results show that the time at which the interface delamination starts increases linearly with the increase in cohesive strength and decreases exponentially with an increase in loading rate.

KEYWORDS: Energetic Material, Interface, Binding Agent, HTPB, AP, NMRS, CFEM

1.1 Introduction

Energetic materials are used in a large number of applications, such as, explosive, propellant, and pyrotechnic formulations. An example of such a material is a crystalline oxidizer (e.g., ammonium perchlorate-AP) embedded in a polymeric binder (e.g., Hydroxyl Terminated Polybutadiene-HTPB). A typical industrial solid propellant consists of ~70% AP, ~10% HTPB and around 20% Al by weight, [1]. These materials are sensitive to heat and mechanical shock, which may be triggered by fire or by impact with bullets or fragments. The complex mechanical behavior of these materials is due to complicated microstructure and physical processes occurring at multiple length scales. Accurate prediction of the mechanical behavior of an energetic material can be made based on an understanding of their physical properties and their response under impact or shock. The main failure mechanisms in energetic materials have been identified as particle fracture, interfacial failure, and cavitation in the binder [2]. The effect of interface on the failure of these materials have been studied in literature both experimentally and numerically. Polymer bonded explosives (PBXs) under tensile loading have shown that interface debonding was the dominant failure mode [2] indicating that interfaces are weaker than the main phases. The macroscopic crack propagates mainly along the particle-matrix interface [3, 4]. The fracture resistance of such materials has been shown to be strongly affected by the toughness of the interface between the constituents. Interface strength depends on the constituent material, i.e., particle, matrix and/or binding agents, [5, 6]. Rae et al. [3] as well as other experimental efforts [3, 7-10] have shown a particle size effect on the performance of energetic materials. Drodge et al. [10] showed that increasing the particle size decreases the yield strain. Chen [11] used a digital image correlation technique combined with scanning electron microscope (SEM) imaging system to measure the displacement and strain fields at the micro-scale in PBX-9501. Their analyses showed that the trans-granular cracking is the most dominant fracture mode. Yeager [12] has

shown the effect of interface chemical structure and the microstructure on the mechanical behavior of PBX. Interfacial structure was altered by adding a plasticizer. The plasticizer inhibited the formation of a large interface/interphase. The difference in interfacial properties had a significant effect on the crack initiation and explosive sensitivity in such materials. The present work focuses on *in-situ* measurements of interface level rate dependent mechanical properties as well as the cohesive fracture properties of model AP-HTPB interfaces and on using such measurements for material behavior prediction under high strain rate loading.

Numerical studies based on cohesive zone models (CZMs) [13-31] have been performed to analyze particle/matrix interface debonding. Several studies [32-41] have used CZM for particle/matrix debonding analyses in energetic materials using a nonlinear three stage cohesive law to simulate the debonding, e.g., see the work of Tan and coauthors [37]. The approach makes use of the minimum potential energy principle with respect to interface displacement jump. It has been shown that small particles in energetic materials lead to hardening behavior while large particles soften the composites. The debonding of large particles is unstable and may lead to catastrophic failure. The effect of interface debonding on a PBX sample containing an elastic particle and a viscoelastic matrix [35] has shown that the strain rate strongly affects the mechanical behavior of the composite. However, such studies assume a cohesive law for particle/matrix interfaces based on the macroscopic behavior of the material, which may not accurately represent the local microscopic behavior. Atomistic simulations have also been performed in order to examine the deformation behavior, mainly under shock, in energetic materials [42-45] with some simulations providing good guidelines for developing interface level constitutive behavior descriptors.

In this work, the effect of local rate dependent interface level strength and the strain rate on the rate dependent failure and debonding in model HTPB-AP composites is analyzed. A strain rate dependent viscoplastic constitutive model is developed based on dynamic high strain rate experiments performed on a set of analyzed HTPB-AP interfaces. A mechanical Raman spectroscopy (MRS) setup [46] is used to obtain cohesive fracture separation properties in the analyzed samples including interface delamination strength and interface fracture energy. The measured cohesive fracture parameters capture the effect of interface chemistry variation. The cohesive parameters and the viscoplastic model were implemented in a cohesive finite element method (CFEM) scheme to simulate dynamic crack propagation, as well as delamination, in simulated HTPB-AP samples. A qualitative validation of the delamination with the Kolsky bar experiment has also been considered.

The chapter is organized in the following manner: Section 2 describes the details of experimental setup. The CFEM modeling approach that incorporates the material model parameters obtained using the experiments is also discussed. Section 3 analyzes the results obtained using the CFEM model and experiments. Finally, a summary discussion of the results and concluding remarks are presented in Section 4.

1.2 Experimental Methods

In this section, the experimental methods used in this work are explained. First, the steps to fabricate samples are explained. There are two separate types of mechanical property measurement experiments: (1) A dynamic impact setup to measure the rate dependent stress-strain relations that are used to calibrate a viscoplastic constitutive model; and (2) Interface de-cohesion experiments using MRS that are used to measure the interface cohesive separation properties for the CFEM model used in this work. In the following subsection, first the dynamic impact

experiments used to obtain the viscoplastic constitutive model parameters is discussed. Finally, the MRS setup to obtain the CFEM model parameters is described.

The samples used in the experiments consist of AP particles embedded in an HTPB binder. Two types of samples: the first type with a binding agent (cyanoethylated polyamine (HX-878 or Tepanol)) and the second type without any binding agent; were prepared to analyze the effect of interface chemistry. Spherical AP particles (supplied by Firefox Enterprise Inc.) in the size range of 600-800 μm were manually selected. HTPB was fabricated using a mixture of R-45M liquid polybutadiene (Firefox Enterprise Inc.) and isophorone diisocyanate (IPDI) at an OH index ratio of 1.05. In both sample types, AP particles were carefully placed, one by one, in the binder so that many single particle samples could be cut from the cured mixture. The largest available particles were chosen so that during experimentation, visual inspections of the AP particle and the AP-HTPB interface could be performed. In the second sample type, a surface binding agent (Tepanol) was added to the binder at a mass ratio of 0.5 % to fabricate samples with higher surface adhesion, while keeping the same index ratio. The constituents were manually mixed and degassed in vacuum for 30 minutes. They were poured into PTFE molds with a depth of 1 mm and the particles were added. The samples were cured at 60° C in a convection oven for 7 days. After the cure, they were removed from the molds and cut into the desired dimensions for testing, [47].

1.2.1 A Dynamic Impact Experiment Setup for Rate Dependent Property Measurements

The mechanical properties of solid propellants have been shown to depend upon the size and type of filler material (oxidizer) used [48]. In order to understand the underlying mechanisms along with their mechanical strength, characterization techniques with sufficient resolution are needed.

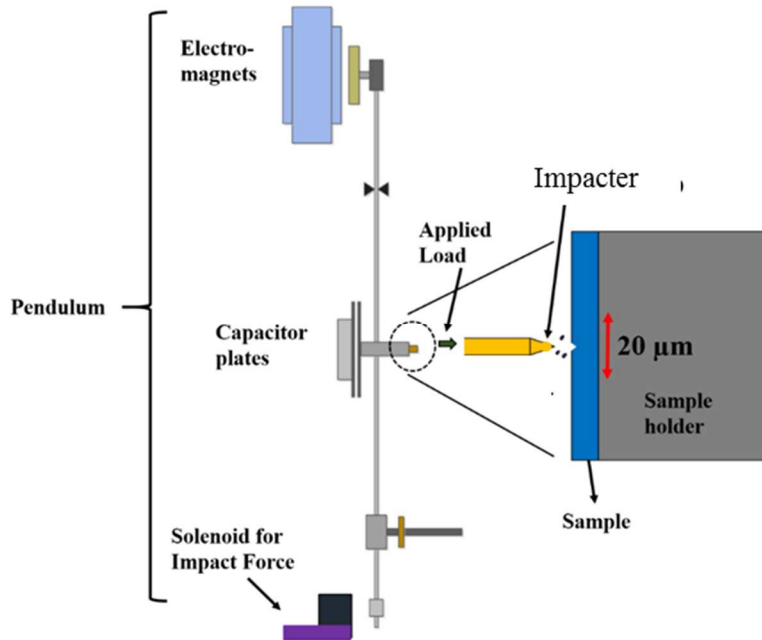


Figure 1 Nanoscale dynamic impact experimental setup.

The experimental procedure for measuring the interface level dynamic properties involves impacting the surface of the material being tested by an impactor (Fig. 1). The strain rates in such a setup is typically up to 100 s^{-1} [49, 50]. The experimental data includes information of depth of penetration (or the position of the impactor) during impacts with respect to time (Fig. 2). The derivative of depth versus time gives the information of velocity during impacts (Fig. 2).

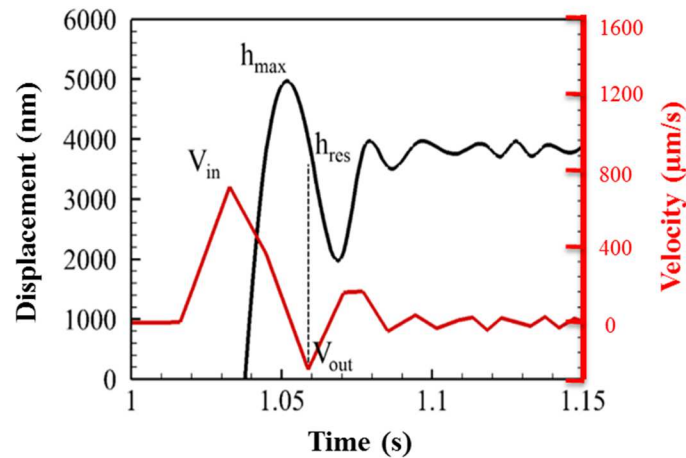


Figure 2 Representative depth versus time obtained from dynamic impact experiment and calculated velocity versus time data.

The dynamic impact experiments were performed using a modification of the high strain rate impact schedule of Micro Materials, UK [46-49]. Similar high rate compressive impact techniques have been successfully applied to model site specific behavior such as at the interface between two materials at high strain rates [45]. The novelty of the experiments lies in the fact that impacts are precisely at the interfaces in the precision range of nanometers to micrometers. The impactor tip impacts at the analyzed interfaces precisely thus making sure that the energy from the impact is delivered at the interfacial region. The experimental set up consists of a 3D stage to mount the sample that allows it to move in x, y, and z Cartesian directions. The interface impact measurements were performed with a spherical impactor of radius 1 μm . The impactor is mounted on a pendulum that is hanging vertically on frictionless springs to let it move freely. The force on the pendulum is applied through the electromagnets as shown in Fig. 1. From its initial stationary solenoid position, the impactor position is monitored continuously as a function of time t , including the initial impact trajectory and the initial rebound from the material surface [49]. During single impact experiments, a typical depth versus time history is shown in Fig. 2. The depth in this case

corresponds to the position of impactor with respect to the sample surface. The velocity of the impactor can be calculated as the first derivative of the response marked with V in Fig. 2. The maximum depth (h_{max}), the initial contact velocity (V_{in}), the outgoing velocity (V_{out}) and the residual depth (h_{res}) are obtained as shown in Fig. 2. The residual depth is the position at the point of detachment from the sample on the first rebound which is the depth corresponding to the outgoing velocity as shown in Fig. 2. The strain rate, $\dot{\epsilon}$, of the impact changes with the depth of impact. An average strain rate characterizing the impact can be approximated by the expression,

$$\dot{\epsilon} \approx \frac{V_{in}}{h_{max}}, \quad (1)$$

where h_{max} is the maximum depth and V_{in} is the maximum velocity. The strain and stress are given by [49, 50],

$$\begin{aligned} \epsilon &= \frac{h_{res}^2}{h_{max}^2} & \text{and} \\ \sigma &= \frac{P}{\pi h_{max}^2} \end{aligned}, \quad (2)$$

where h_{res} and h_{max} are defined in Fig. 2. The strain rate was in the range of 10 to 100 s⁻¹. The strain rates in the current experiment depends on the maximum load applied at the impact points. The highest load was applied to observe the behavior of material under the highest deformation state. The impacts were conducted at the interface of HTPB-AP and in the bulk phase of both materials. The impact stress-strain data from the experiments are fitted to power law viscoplastic constitutive model to define the material mechanical behavior.

1.2.1.1 Fitting a Viscoplastic Constitutive Model to Dynamic Impact Experiment Data

Heat dissipation during impact has been discussed in literature using theories similar to the work of Clayton [51]. However, in this work, since experiments cannot measure the heat dissipation directly or indirectly, the viscoplastic model neglects the heat dissipation. We use the standard assumption for finite strain inelastic problems: the multiplicative decomposition of the deformation gradient \mathbf{F} into an elastic and an inelastic part \mathbf{F}^e and \mathbf{F}^{vp} , i.e.,

$$\mathbf{F} = \mathbf{F}^e \cdot \mathbf{F}^{vp} . \quad (3)$$

The plastic deformation gradient tensor \mathbf{F}^{vp} maps a material tangent vector from the reference configuration to the relaxed configuration, which is obtained from the reference state by a pure plastic deformation and rotation. Subsequently, the elastic deformation gradient tensor \mathbf{F}^e maps this material tangent vector from the relaxed to the current configuration, which is obtained from the relaxed configuration by purely elastic deformation and rotation. The relaxed configuration is not completely defined, since an arbitrary rigid rotation can be superimposed on it and leave it unstressed. The velocity gradient tensor \mathbf{L} in the current configuration is defined by,

$$\mathbf{L} = \dot{\mathbf{F}} \cdot \mathbf{F}^{-1} = \mathbf{D} + \mathbf{W} , \quad (4)$$

where \mathbf{D} and \mathbf{W} are the rate of deformation and material spin tensors, respectively, defined as,

$$\begin{aligned} \mathbf{D} &= \frac{1}{2}(\mathbf{L} + \mathbf{L}^T), \quad \text{and} \\ \mathbf{W} &= \frac{1}{2}(\mathbf{L} - \mathbf{L}^T) \end{aligned} . \quad (5)$$

Taking into account Eq. (4), the tensor L is accordingly given by,

$$\begin{aligned} L &= D + W = \dot{F} \cdot F^{-1} \\ &= \dot{F}^e \cdot F^{e-1} + F^e \cdot \dot{F}^{vp} \cdot F^{vp-1} \cdot F^{e-1} \end{aligned} \quad (6)$$

which can be written as

$$\begin{aligned} D^e + W^e &= \dot{F}^e \cdot F^{e-1}, \\ D^{vp} + W^{vp} &= F^e \cdot \dot{F}^{vp} \cdot F^{vp-1} \cdot F^{e-1} \end{aligned} \quad (7)$$

In the region of finite deformations, the elastic strain is generally assumed to be smaller than the plastic one. The deformation rate tensor D requires constitutive laws for D^e and D^{vp} . The constitutive law for D^{vp} is the flow rule under finite deformations, while the constitutive law for D^e is related to the theory of hypoelasticity. The general form of the objective stress-rate and strain-rate relation, according to Rivlin [52] and Truesdell [53], is given by,

$$\hat{\boldsymbol{\tau}} = f(\boldsymbol{\tau}, D^e), \quad (8)$$

where $\boldsymbol{\tau}$ is the Cauchy stress tensor, D^e is the elastic part of the deformation rate tensor D , and $\hat{\boldsymbol{\tau}}$ is an objective rate of the stress tensor. There are a number of objective rates that can be defined, leading to different results. The selection of a specific type of the objective rate that will be used is still an open problem, as is also mentioned by Khan and Huang [54]. In our work, the objective rate of the Cauchy stress tensor is taken to be as,

$$\hat{\boldsymbol{\tau}} = \dot{\boldsymbol{\tau}} - \mathbf{W} \cdot \boldsymbol{\tau} + \boldsymbol{\tau} \cdot \mathbf{W}. \quad (9)$$

Following Eqs. (7) and (9), the definition of the sub-structural spin \mathbf{W} requires a constitutive equation for \mathbf{W}^{vp} , which appears in the objective rate and, as a consequence, in the rate type constitutive equations. Therefore, according to Dafalias [55], under finite plastic deformations

constitutive laws for both tensors \mathbf{D}^{vp} and \mathbf{W}^{vp} are required. Based on the linear form of hypoelasticity,

$$\hat{\boldsymbol{\tau}} = \mathbf{C} : [\mathbf{D} - \mathbf{D}^{vp}], \quad (10)$$

where \mathbf{C} is a fourth order tensor. In the case of an isotropic material, it is given by

$$\mathbf{C} = \frac{E}{1+\nu} \left[\mathbf{I}' + \frac{\nu}{1-2\nu} \mathbf{I} \otimes \mathbf{I} \right]. \quad (11)$$

Here, E is the Young's modulus, ν is the poisson ration and \mathbf{I} is the 3x3 identity matrix.

For an isotropically hardening viscoplastic solid, \mathbf{D}^{vp} is given by,

$$D_{ij}^{vp} = \frac{\partial f}{\partial \tau_{ij}} \dot{\lambda} = \frac{3}{2\bar{\sigma}} \tau'_{ij} \dot{\lambda}, \quad (12)$$

where f is the Mises yield function, $\dot{\lambda}$ is the equivalent viscoplastic strain rate given by [56],

$$\dot{\lambda} = \dot{\bar{\epsilon}}^{vp} = \frac{d\bar{\epsilon}^{vp}}{d\bar{\sigma}} \dot{\bar{\sigma}}, \quad (13)$$

$$\bar{\sigma} = \sqrt{\frac{3}{2} \tau'_{ij} \tau'_{ij}}, \quad \boldsymbol{\tau}' = \boldsymbol{\tau} - \frac{1}{3} tr(\boldsymbol{\tau}) \mathbf{I}, \quad (14)$$

and $\bar{\epsilon}^{vp}$ is the equivalent viscoplastic strain, which is given by,

$$\bar{\epsilon}^{vp} = \chi \left(\dot{\bar{\epsilon}}^{vp} \right)^m \left(\bar{\sigma} \right)^n. \quad (15)$$

Using Eq. (13) and (15), $\dot{\lambda}$ is calculated and substituted back into Eq. (12) to obtain the viscoplastic rate of deformation. $\dot{\bar{\sigma}}$ is the effective stress rate obtained by differentiating Eq. (14) with respect to time,

$$\dot{\bar{\sigma}} = \frac{d\bar{\sigma}}{dt} = \frac{3}{2\bar{\sigma}} \tau'_{ij} \dot{\tau}'_{ij}, \quad (16)$$

where $\dot{\tau}'_{ij}$ is the time rate of change of Kirchoff's stress, which is obtained by substituting Eq. (10) into Eq. (9). Here, we assume the viscoplastic spin rate $\mathbf{W}^{vp} = 0$ as suggested by Boyce et al. [57]. In other words, a relaxed configuration which is not spinning is chosen. Eq. (10) and Eq. (11) give the material rate of Kirchoff's stress as,

$$\hat{\boldsymbol{\tau}} = \dot{\boldsymbol{\tau}} - \mathbf{W} \cdot \boldsymbol{\tau} + \boldsymbol{\tau} \cdot \mathbf{W} = \mathbf{C} : [\mathbf{D} - \mathbf{D}^{vp}], \quad (17)$$

which results in

$$\dot{\boldsymbol{\tau}} = \hat{\boldsymbol{\tau}} + \mathbf{W}^e \cdot \boldsymbol{\tau} - \boldsymbol{\tau} \cdot \mathbf{W}^e. \quad (18)$$

The updated Kirchoff's stress at $t + \Delta t$ is then given by,

$${}^{t+\Delta t} \tau_{ij} = {}^t \tau_{ij} + \Delta \tau_{ij}, \quad (19)$$

where

$$\Delta \boldsymbol{\tau} = \dot{\boldsymbol{\tau}} \cdot \Delta t.$$

1.2.2 Mechanical Raman Spectroscopy Measurements of Interface Decohesion

Micro-Raman spectroscopy is a technique by which stress in microscale structures can be extracted based on Raman shift measurements [49]. The first experimental investigation of the effect of external stress on the Raman modes was done by Anastassakis et al. [58] on silicon. Raman scattering measurements in the presence of externally applied stress have been performed by a large number of investigators on different kinds of samples [59]. Raman shifts are typically reported in wavenumbers, which have units of inverse length, as this value is directly related to

energy. Raman spectroscopy of AP and polybutadiene has been reported in literature, [60-68]. The pressure dependence of internal mode frequency in AP was studied [60, 67], and it was reported that as the pressure increases, the Raman shift of internal mode frequency of NH_4^+ and ClO_4^- both increases. However the N-H stretching mode Raman shift decreases with an increase in pressure, [64]. The temperature dependence of Raman active modes in the single crystal AP has also been investigated, [62]. Nallasamy et al. [65] analyzed the Raman spectra of cis- and trans-1,4-polybutadiene and assigned the vibration modes to the observed frequency. McNesby et al. [63] used the Fourier transform Raman spectroscopy to characterize different samples of energetic materials and propellant formulations. Raman spectra of several energetic materials were measured to be in the range of 100 to 3000 cm^{-1} .

In the MRS approach [46], *in-situ* measurements of Raman shifts in a material are performed during loading. Based on a separately performed calibration under identical boundary conditions, the Raman shifts are converted to stresses. In the current study, Raman shifts are calibrated on samples under uniaxial tensile loading. A Deben loading stage was used to load the sample at a rate of 0.1 mm/min until the failure. A HORIBA Xplora Plus micro-Raman spectrometer was used to obtain the Raman spectra of the scan area at an excitation wavelength of 532 nm and a grating size of 2400. The resolution of the micro-Raman spectrometer near the CH_2 stretching zone is 1.4 cm^{-1} . Raman shifts were observed and recorded in the CH_2 stretching zone, see Fig. 3(a), as a function of applied stress. Peaks on the spectra corresponds to different vibration modes are also indicated as reported in [65]. Raman shifts were measured and the shift versus stress at a cross-section was plotted, as shown in Fig. 3(b). A linear relation between the stress and Raman shift was then obtained as [69]

$$\sigma = C\Delta w, \quad (20)$$

where Δw is the shift in wavenumber due to loading and C is a constant which is the slope of the Raman shift versus stress curve as shown in Fig. 3(b). This calibration constant is then used to obtain stress around the interface in a one particle HTPB-AP sample for the two types of samples: one without the binding agent and other with binding agent.

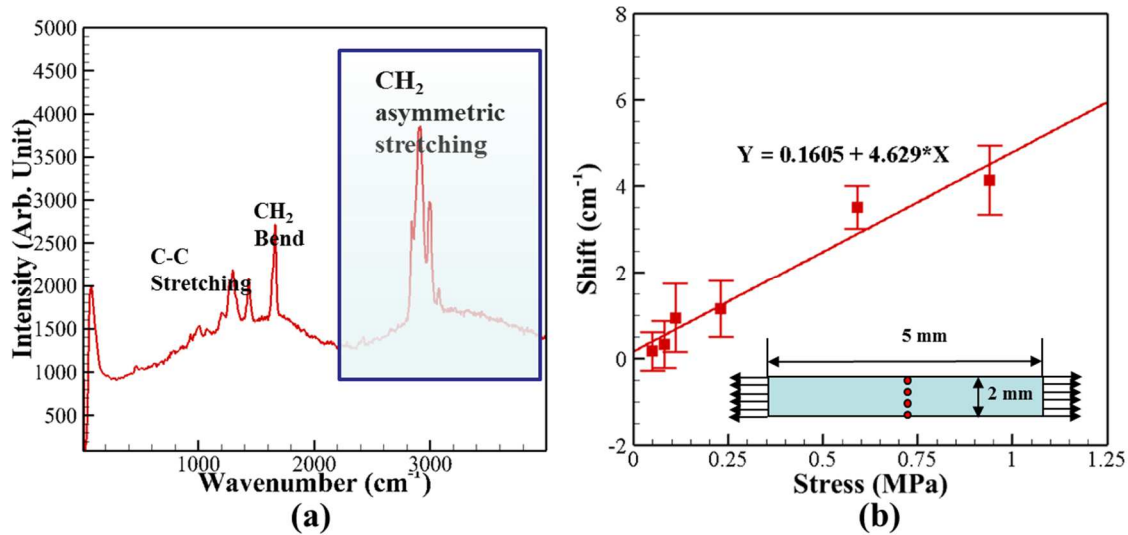


Figure 3 (a) A typical Raman spectra observed in an AP-HTPB sample of type 1 and (b) the corresponding stress versus shift calibration curve.

MRS measurements are used to measure stresses during delamination of the particle-binder interface as outlined in the results section. The combination of stresses and energy spent in delamination is used to derive cohesive zone parameters as shown in Section 3 later. The cohesive zone parameters are used in the cohesive finite element framework described in the next section to predict interface property dependent material behavior.

1.2.2.1 Cohesive Finite Element Method Framework

The dynamic behavior of the composite material system is modeled using the explicit cohesive finite element method (see e.g. [70, 71]). The cohesive finite element method (CFEM) provides a means for quantitative analysis of fracture behavior through explicit simulation of

fracture processes. The cohesive crack approach dates back to the work of Barenblatt [72] for brittle materials and the work of Dugdale [73] for elastoplastic materials. It has been extensively used to model crack growth in concrete, ceramics, polymers, composites, and metals. It has also been used to analyze fracture along interfaces, [74].

An explicit time-integration scheme based on the Newmark β -method is employed. The time step Δt needs to be small enough to ensure that the increment of the cohesive separation Δ be sufficiently small in each numerical step to avoid numerical instability. Based on the material properties and the Courant–Freidrichs–Lewy criterion with material-related numerical stability considerations, the average time step is of the order of 1 ns in our current research, [75]. The single particle sample shown in Fig. 4 were modeled using CFEM. The weak form of the CFEM model is given by,

$$\int_V \boldsymbol{\tau} : \delta \mathbf{F} dV - \int_{S_{int}} \mathbf{T} \cdot \delta \Delta dS = \int_{S_{ext}} \mathbf{T} \cdot \delta \mathbf{u} dS - \int_V \rho \frac{\partial^2 \mathbf{u}}{\partial t^2} \cdot \delta \mathbf{u} dV, \quad (21)$$

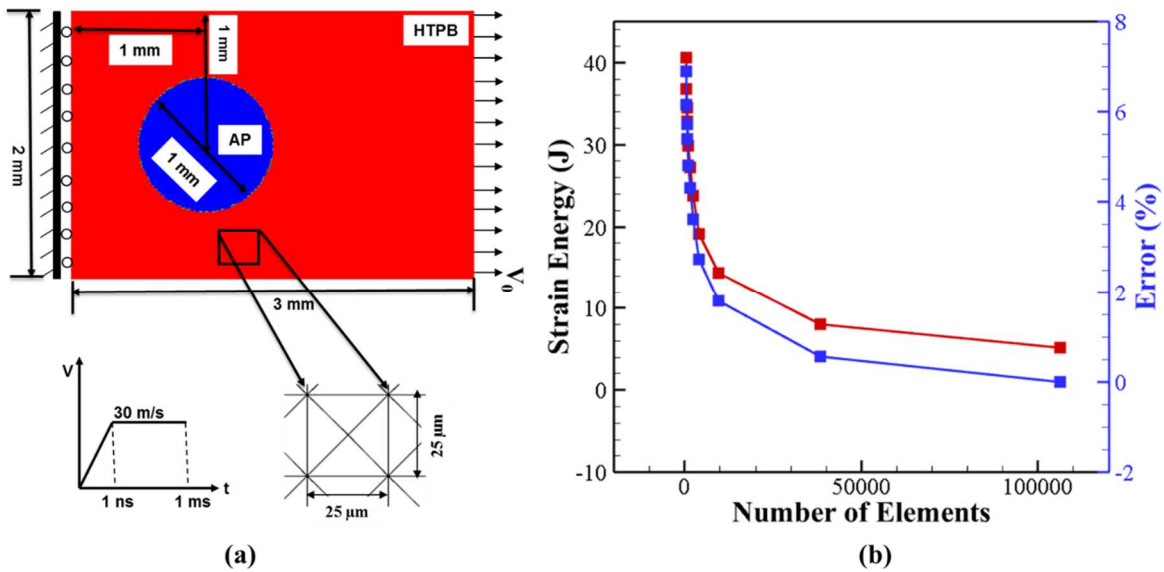


Figure 4 (a) Finite element mesh used and (b) mesh convergence analysis.

In the cohesive model used, the traction T applied on material points coinciding at and occupying position x on the cohesive surface in the reference configuration is work-conjugate to surface separation Δ . In the reference configuration, the cohesive law is given by,

$$\mathbf{T}(\mathbf{x}) = \mathbf{T}[\Delta(\mathbf{x})], \quad (22)$$

and the work of separation under this traction at any stage of deformation is [76]

$$W_{sep} = \int_{S_0} \int_0^{\Delta} \mathbf{T}(\mathbf{x}, \Delta) \cdot \mathbf{d} \Delta \mathbf{d}x . \quad (23)$$

Here, we have assumed that cohesive traction-separation relations are locally determined, i.e., the cohesive traction at one point is fully determined by the separation at the point itself. Several constitutive relationships of the cohesive zone model have been developed based on an effective separation (Δ) and an effective traction (\mathbf{T}). The relation between effective separation and traction are defined by various cohesive relations such as cubic polynomial, trapezoidal, smoothed trapezoidal, exponential, linear softening and bilinear softening functions [74]. In this work we have used an irreversible bilinear cohesive zone model [74]. In order to prevent the penetration due to the large deformation, a penalty traction is used to apply sufficient normal traction. The penalty traction is taken to be of the form [20],

$$T_n = T^{\max} \exp(\Delta_n / \Delta_c), \quad (24)$$

where T_n is the normal traction, T^{\max} is the cohesive strength, Δ_n is the normal penetration and Δ_c is the critical displacement.

The CFEM simulations are carried out under plane strain assumptions. To track complex crack/microcrack patterns, and crack branching, cohesive surfaces are specified along all of the finite element boundaries as an intrinsic part of the finite element model. All of the cohesive surfaces serve as potential crack paths in the microstructure; therefore, fracture inside each microstructural phase and along interphase boundaries can be explicitly resolved, [74, 77]. Accordingly, the analyses are able to take into account the matrix/particle failure, as well as interfacial fracture. The finite element meshes used have a uniform structure with “cross-triangle” elements of equal dimensions arranged in a quadrilateral pattern, see Fig. 4. This type of triangulation is used since it gives the maximum flexibility for resolving crack extensions and semi-arbitrary fracture patterns, [78].

1.3 Results And Analyses

In this section, we analyze the effect of interface chemistry and strain rate on the failure behavior of a single particle HTPB-AP sample using CFEM. First, parameters for a viscoplastic constitutive model fitted to dynamic impact experiments are obtained. The viscoplastic constitutive model is then validated by comparing results from an AP-HTPB sample deformation experiment. Cohesive fracture parameters are then obtained using the MRS experiments. Together, all of the parameters are used in a rate dependent CFEM formulation to qualitatively validate the used CFEM framework with the existing results from a Kolsky bar tensile experiment [47]. Thereafter, predictions from the CFEM formulation are analyzed.

1.3.1 Viscoplastic Model Parameters Measured using the Dynamic Impact Experiment

Energetic material mechanical behavior has been modeled using viscoelastic [79, 80] as well as elasto-viscoplastic [81, 82] constitutive models. For high strain rate loading, viscoplastic

models are used frequently [83-85]. Kalayciogly [82] et al. modeled an HTPB/AP composite propellant using Perzyna's viscoplastic model. In this work, following Tsai and Sun [86], we assume an effective stress-effective viscoplastic strain curve by a power law model

$$\bar{\epsilon}^{vp} = A(\bar{\sigma})^n, \quad (25)$$

where $\bar{\epsilon}^{vp}$ and $\bar{\sigma}$ are the equivalent strain and equivalent stress respectively. A is a power law function of effective plastic strain rate, given as [86],

$$A = \chi(\dot{\bar{\epsilon}}^{vp})^m. \quad (26)$$

The viscoplastic model then can be given as,

$$\bar{\epsilon}^{vp} = \chi(\dot{\bar{\epsilon}}^{vp})^m (\bar{\sigma})^n. \quad (27)$$

Figure 5 (a) shows amplitude A as a function of effective plastic strain rate on the log-log scale for the HTPB binder. Multiple impacts were done to obtain several stress-strain-strain rate data in order to fit a power law model as shown in Fig. 5. The parameters χ and m are then determined from these plots as the intercept and the slope, respectively. Once m and χ are determined, this model can be extrapolated to predict the material behavior at different strain rates. Using this fitting procedure on the experimental data for different strain rates, we obtain the corresponding stress-strain curves shown in Fig. 5 (b).

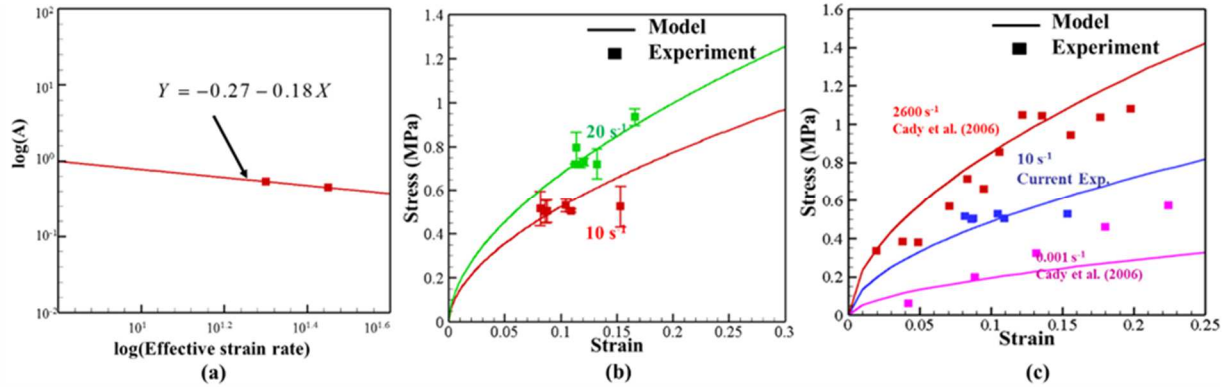


Figure 5 (a) log-log plot for the viscoplastic parameters and (b) stress-strain curve-fitting using the power law model for HTPB binder in the case of the HTPB-AP sample as a function of strain rate and (c) fitted curve with the current model to the experimental stress-strain data for HTPB obtained from an Split-Hopkinson pressure bar (SHPB) test performed by Cady and co-workers [88].

In order to show the validity of the values of parameters χ , n and m found from the fitting of the stress strain data obtained during nano-scale impact test, these values were used to fit the stress strain data obtain from an SHPB test done by Cady and coworkers [88], as shown in Fig. 5 (c). The power law viscoplastic model is also fitted to the experimental data as shown in Fig. 6 for the AP phase and the HTPB/AP interface.

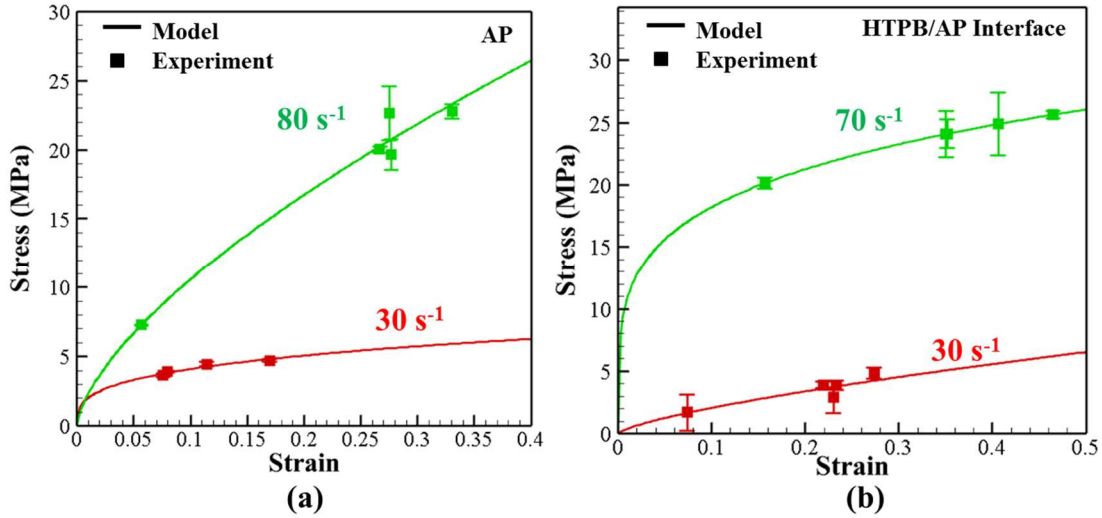


Figure 6 Stress-strain response of (a) AP phase and (b) AP-HTPB Interface in HTPB-AP sample as a function of strain rate.

Table 1 Viscoplastic model parameters for AP, HTPB and the HTPB/AP interface.

Parameter		χ (MPa) ⁻ⁿ	m	n
HTPB		0.54	-0.18	1.8
AP		3.7E10	-9.8	5.9
HTPB/AP Interface	Sample 1	1.0E5	-5.0	2.5
	Sample 2	1.0E4	-4.2	2.0

Table 1 shows the viscoplastic model parameters for the interface, the matrix (HTPB) and the particle (AP) for the two sample types. Sample 1 corresponds to the HTPB-AP sample and Sample 2 corresponds to the HTPB-AP-Tepanol sample. Figure 8 shows the stress-strain curves obtained from the impact experiment for HTPB, AP and the HTPB/AP interface for the two

samples. As can be seen from Fig. 7, the effect of binding agent Tepanol is the most significant on the stress-strain curve for interface. This shows that the interface properties can be altered using a binding agent.

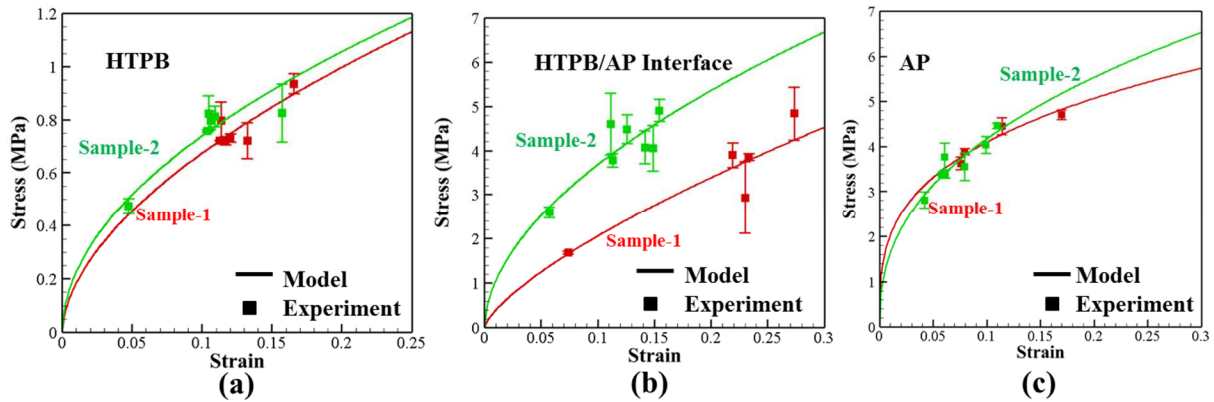


Figure 7 Stress-strain model fitted to the dynamic impact experiment data for (a) HTPB binder, (b) HTPB-AP Interface, and (c) AP phase for different sample types. Sample 1 is without Tepanol and Sample 2 is with Tepanol.

In order to evaluate the validity of the power law viscoplastic stress-strain model proposed above, a 2-dimensional plane strain finite element simulation is carried out in ABAQUS to model the dynamic impact experiment, as shown in Fig 8. The impactor is chosen to be a spherical impactor of radius 1 μm , Fig. 8 (c), which is the size used in the experiment. The viscoplastic constitutive power law model parameters given in Table 1 are used. The cohesive zone model parameters given in Table 2 is used for the bilinear cohesive zone model in ABAQUS. A quadrilateral plane strain element (CPE4) was used for both the HTPB and the AP phases. The impactor is given an initial velocity equal to the maximum velocity obtained in experiment with 1mN load. The simulation was run for the time 0.24 s which was the time at which the residual depth was reached in the experiment. The resulting depth-time curve obtained from the simulation is compared to that from the experiment. Here the depth corresponds to the impactor position with

respect to the sample surface. The result in Fig. 8 (d) show the comparison of depth profile obtained from experiment and simulation qualitatively validating the viscoplastic material model.

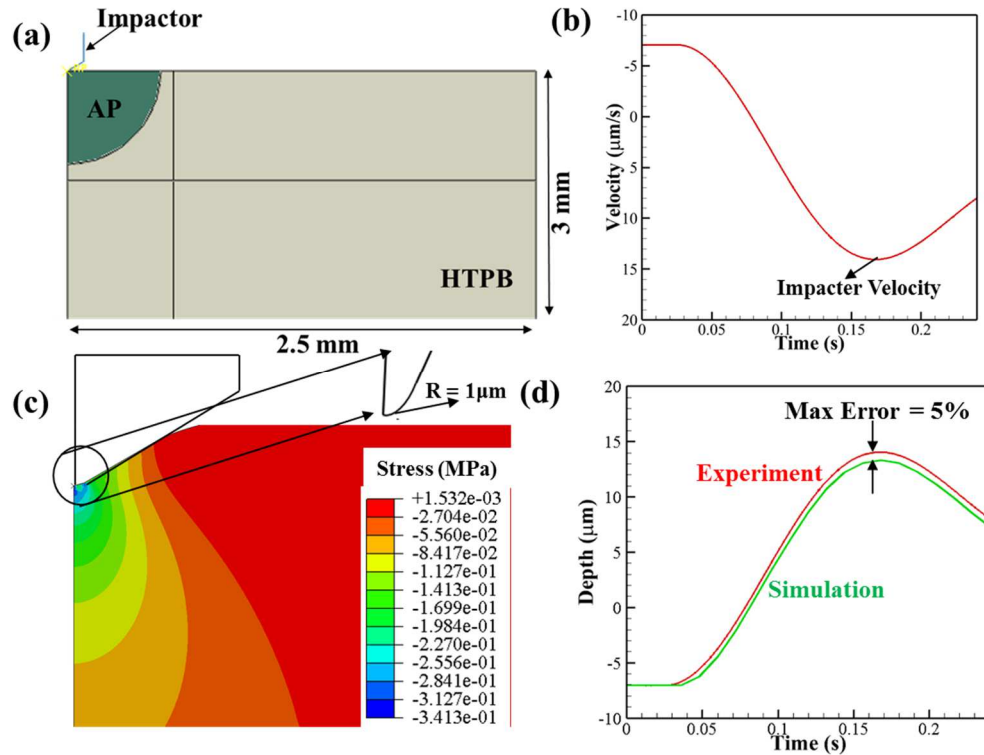


Figure 8 (a) Schematic of dynamic impact finite element model, (b) impact velocity (from experiment), (c) spherical Impactor profile and (d) comparison of depth-time output obtained from experiment (sample type 1) and simulation.

1.3.2 Interface Separation Parameters Measured using MRS

Cohesive zone parameters for the AP and HTPB phases can be obtained based on surface energy and maximum tensile strength values. Due to the lack of experimental data for AP, the tensile strength is assumed to be $E/10$ [74], where E is the Young's modulus of AP. Critical separation for AP is taken to be equal to $5 \mu\text{m}$ [20]. To obtain cohesive parameters for HTPB, a tensile specimen with an edge crack was loaded until failure [89]. The maximum stress required to propagate the crack through the specimen was taken to be the cohesive strength. The cohesive energy is calculated from the area under the load-displacement curve. In order to obtain the

cohesive zone parameters for the AP-HTPB interfaces, delamination experiments at AP-HTPB interfaces in the analyzed samples are performed. The experiments start with an initial crack at the analyzed AP-HTPB interfaces in samples loaded in tensile loading Fig. 9. As load and displacement are applied, the interface crack further extends. The crack extension energy can be calculated based on the load displacement relation, see Fig. 9 (c). The stresses at the crack tip during crack extension are calculated using MRS. A combination of these measurements is used to derive cohesive law parameters.

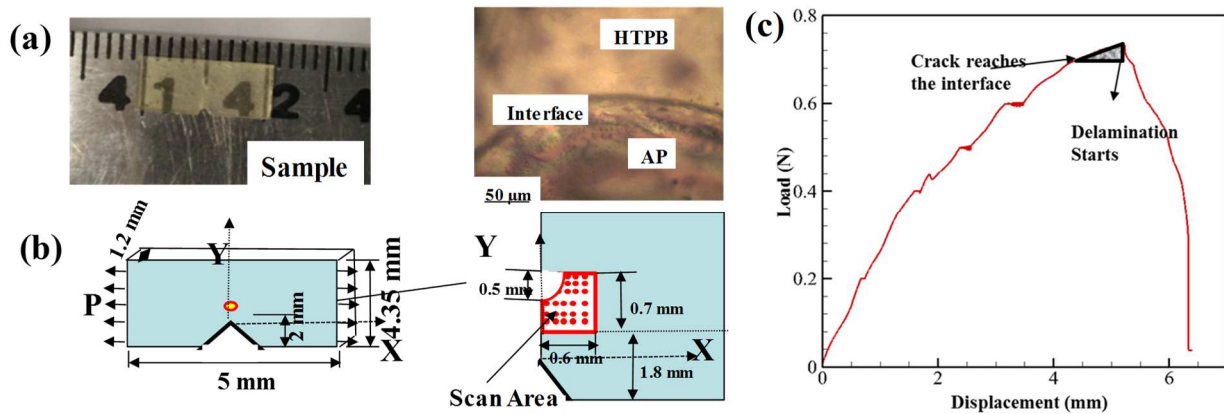


Figure 9 (a) Sample configuration used for the MRS based measurements of interface delamination, (b) sample dimensions and (c) the load-displacement curve obtained during loading for HTPB-AP-Tepanol (type 2) sample (shaded area shows energy spent in the observed crack extension).

The stress distribution around one such HTPB-AP interface obtained using MRS scanning is shown in Fig. 10 as a function of load change during crack propagation. The stress distribution around the interface was plotted by interpolating the stress evaluated at the scan points, as shown in Fig. 9. As can be seen from the load-crack opening curve, see Fig. 9 (c), the delamination starts at just after 0.6 N load. The area under the load displacement curve, see Fig. 9 (c), between the

point where the crack reaches the interface and the point where interface delaminates is the total energy required for delamination [49], which is taken as the cohesive energy at failure. Here, it is assumed that once the crack reaches the interface, a simple brittle fracture takes place. In the future, detailed measurements done in combination with electron microscopy will focus on local heat dissipation in order to develop more complex thickness dependent ductile interface fracture models.

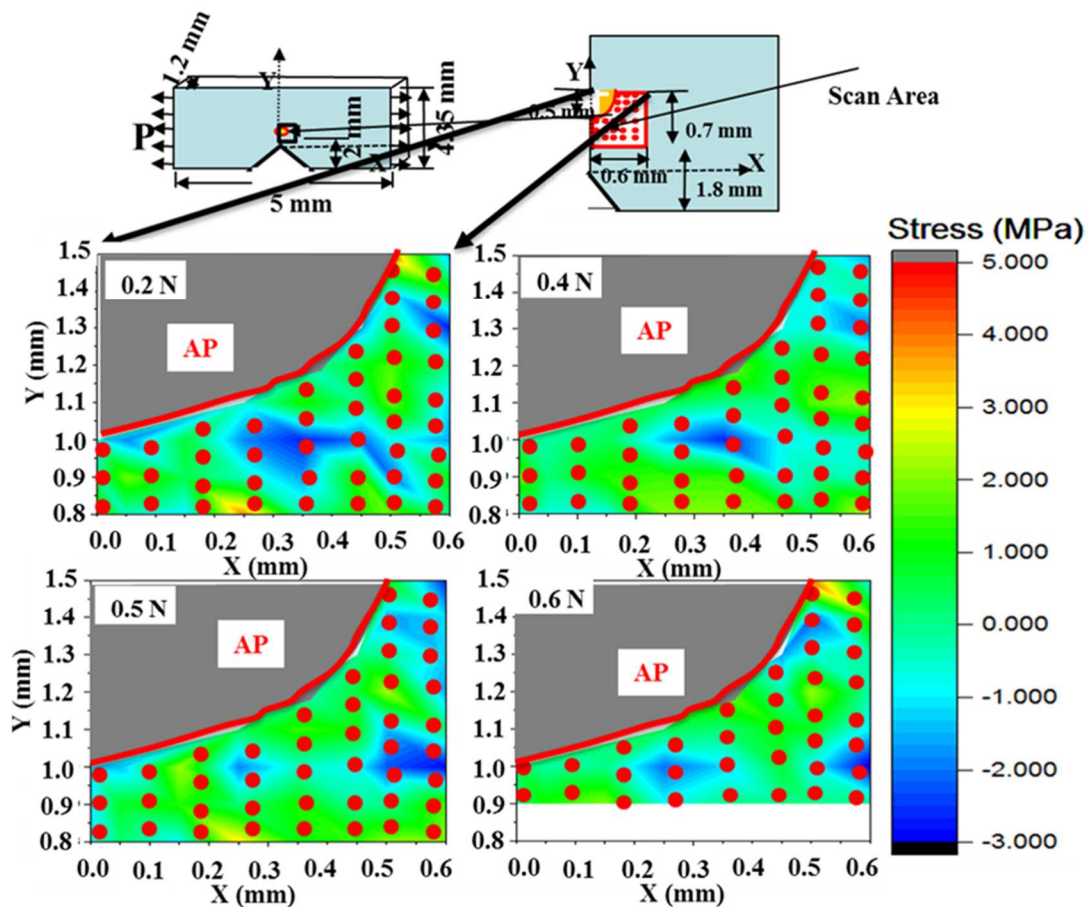


Figure 10 Stress distribution around the HTPB-AP interface for different load until failure for HTPB-AP-Tepanol (type 2) sample. Red dots are the positions where Raman spectra are recorded.

The strength of the interface was evaluated from the stress map obtained using MRS by assuming the strength to be equal to the stress at the start of the delamination. The strength of the interface in sample type 2 is found to be 2.91 MPa and for sample type 1 is equal to 1.1 MPa. Cohesive zone parameters used in the simulation are given in Table 2.

Table 2 Cohesive zone parameters for the constituents of the HTPB/AP composite obtained using MRS.

Material/Interface		Cohesive Strength (MPa)	Critical Displacement (mm)	Cohesive Energy (N/mm)
HTPB		0.8	0.5	0.2
AP		2×10^3	5×10^{-3}	5.0
Interface	Sample 1	1.1	0.12	0.065
	Sample 2	2.91	0.11	0.16

1.3.3 Validation of Constitutive and Cohesive Parameters

As shown in Fig. 11, the samples were loaded in tension at a loading rate of 0.1 mm/min until fracture. During the loading, a set of points on the sample near interface can be scanned to get Raman shifts and the corresponding stresses based on Eq. (26). These Raman shifts can be

obtained at different loads until the interface debonding occurs. A stress map around the HTPB-AP interface obtained by interpolating these values are shown in Fig. 11 for sample type 2.

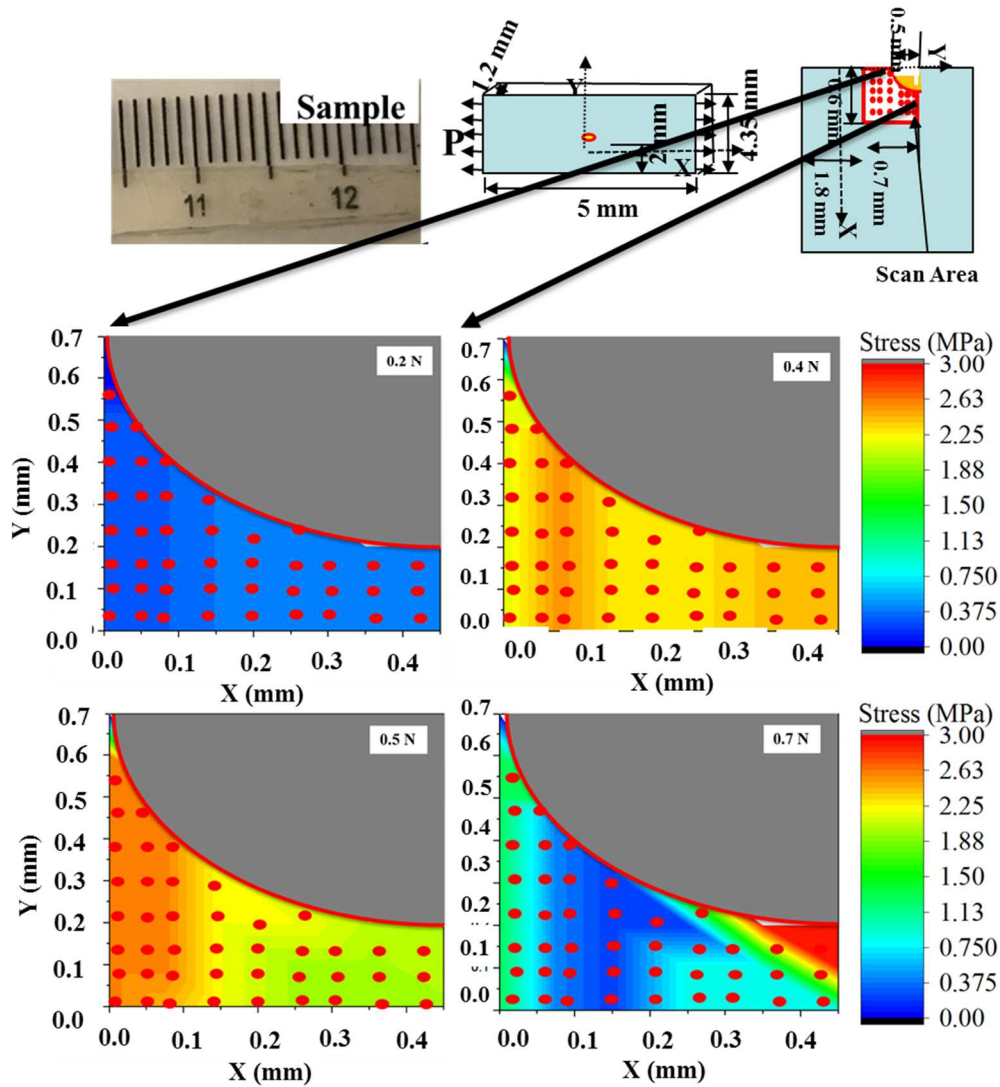


Figure 11 Stress distribution around the interface at different load for sample type 2.

In order to validate the stress map obtained from the MRS measurements a 2-dimensional, plain strain, finite element simulation was carried out using a cohesive element model that incorporates the obtained material property relationships in ABAQUS. The power law viscoplastic model obtained in previous section was used as material model. Cohesive zone properties were

used based on the bilinear cohesive model obtained from the MRS measurements as discussed in the Section 3.1.

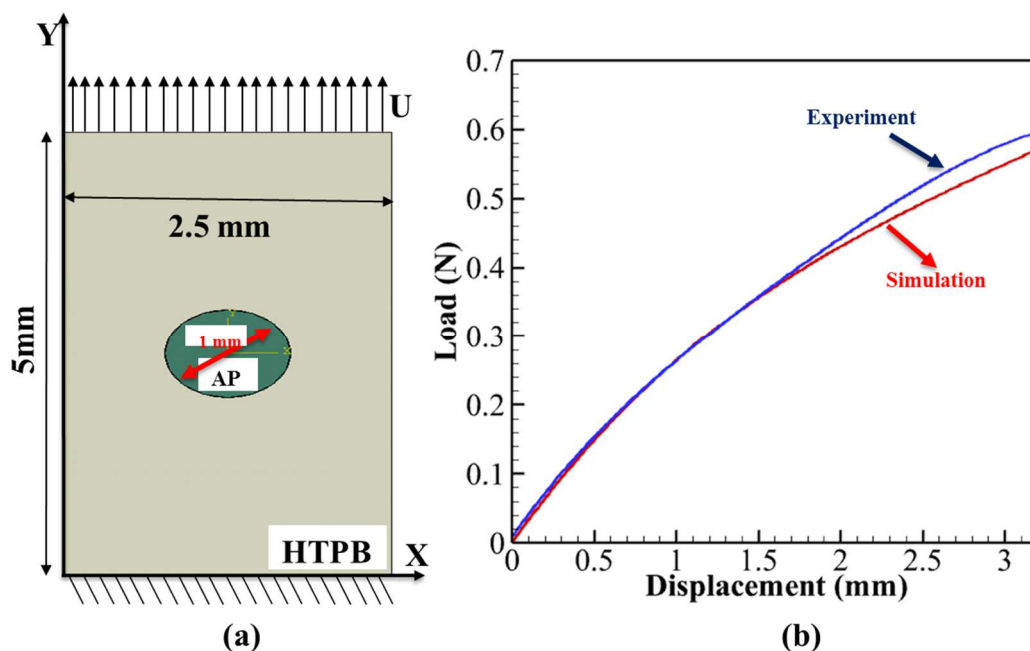


Figure 12 (a) A schematic of the finite element model used in simulation and (b) comparison of load-displacement curve with that obtained from experiment for HTPB-AP-Tepanol sample.

Figure 12(a) shows the model used to simulate the experimental loading in Fig. 10. The goal of this simulation is to compare with the stress map obtained in the MRS experiments. Hence, the displacement is applied in order to reach a load for which the stress map from MRS is available. As shown in Fig. 12(b), the resulting load-displacement curve closely follows the experimentally obtained curve, with less than 5% error. In order to maintain the stress level at the positions where Raman spectra are recorded while obtaining the Raman maps, loads were kept constant. Figure 13(a) shows the stress maps obtained from finite element simulation and Fig. 13(b) shows that obtained from MRS at corresponding loads. Figure 13 shows a good match between the stress

profile obtained from experiment and simulation, which provides a validation of experimental approach used in this paper.

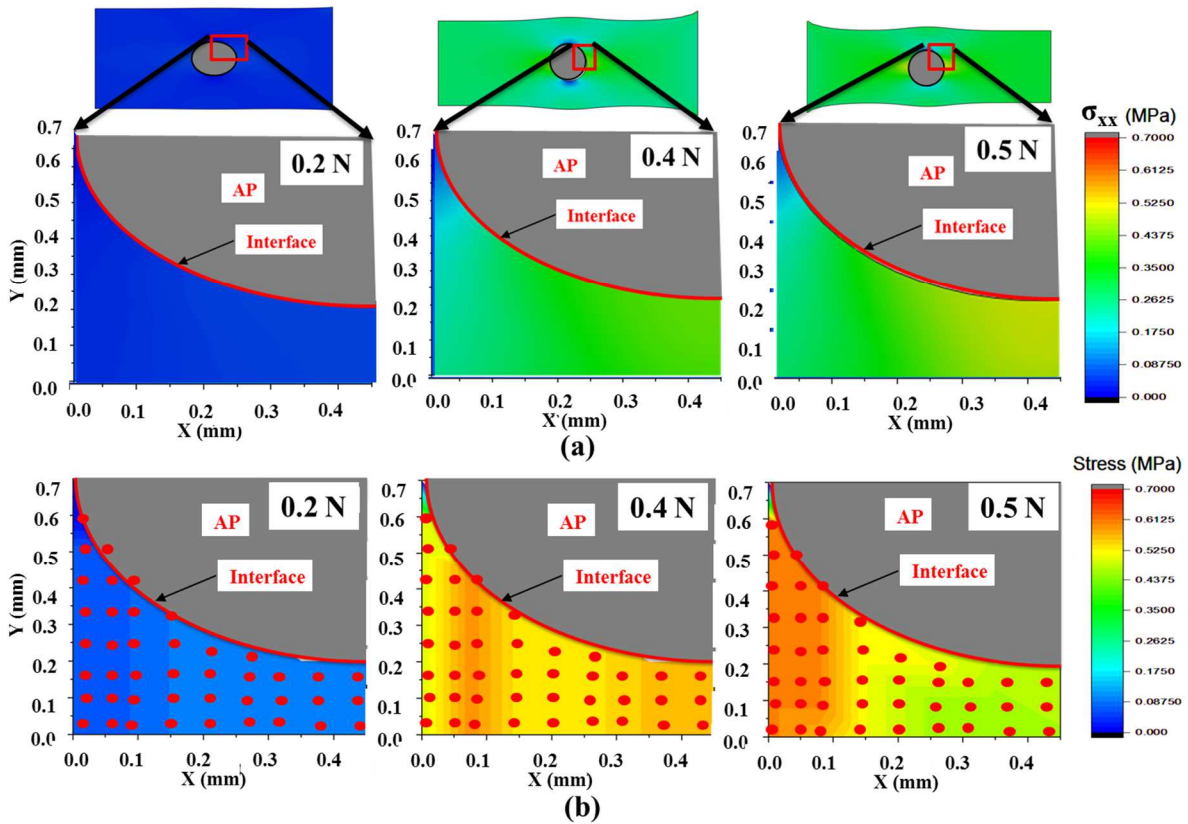


Figure 13 A comparison of stress contour obtained from (a) finite element simulation and (b) from MRS for HTPB-AP-Tepanol (type 2) sample.

1.3.4 Prediction of Interface Property Influence on High Rate Deformation Behavior

Dynamic failure of the one particle sample was simulated using a cohesive finite element method. A two dimensional numerical simulation is carried out for the AP-HTPB specimen with a single AP particle embedded in HTPB binder to simulate the separation observed in the Kolsky bar experiment [47]. Figure 4 illustrates the geometry and boundary conditions employed in the numerical simulation. The length and width of the specimen is set to be $L = 3$ mm and $W = 2$ mm, respectively. The AP particle is idealized as a circle with diameter $D = 1$ mm. While the particle

geometry in the experiment deviates from this approximation, the region of initial debonding observed in the experiments does not contain observable stress concentrations due to irregular shape. The loading condition in the Kolsky bar tension test is idealized as the step-wise-increasing displacement as shown in Fig. 14 [47]. The simulation model and the boundary conditions are shown in Fig. 4 (a). All of the material properties and model parameters used in the simulation are obtained from the experiment as discussed in the previous section. Mesh sensitivity study is performed to ensure that further refinement of mesh does not significantly affect the results.

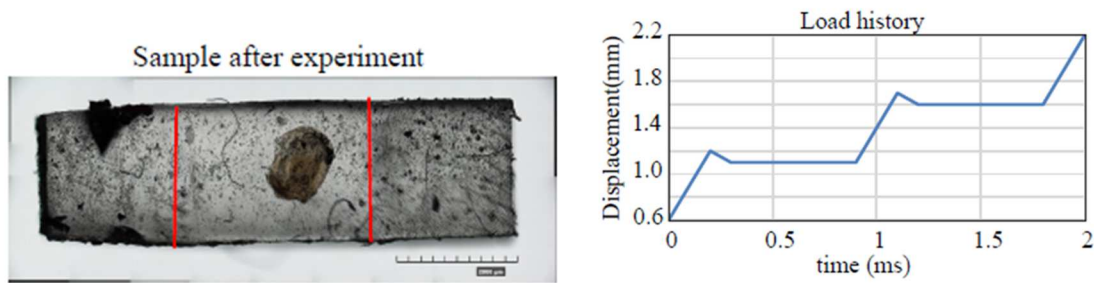


Figure 14 Kolsky bar simulation sample and load-profile [47] used in experiments.

The loading rate of 1000 s^{-1} is used based on the first ramp in the experimental loading profile (see Fig. 14). In order to investigate the mesh size effects on the total energy of the system, the sample without pre-loading and with only elastic properties of HTPB and AP is used. The size of the element was chosen such that it satisfies the bounds given in [74], which is equal to $25 \mu\text{m}$.

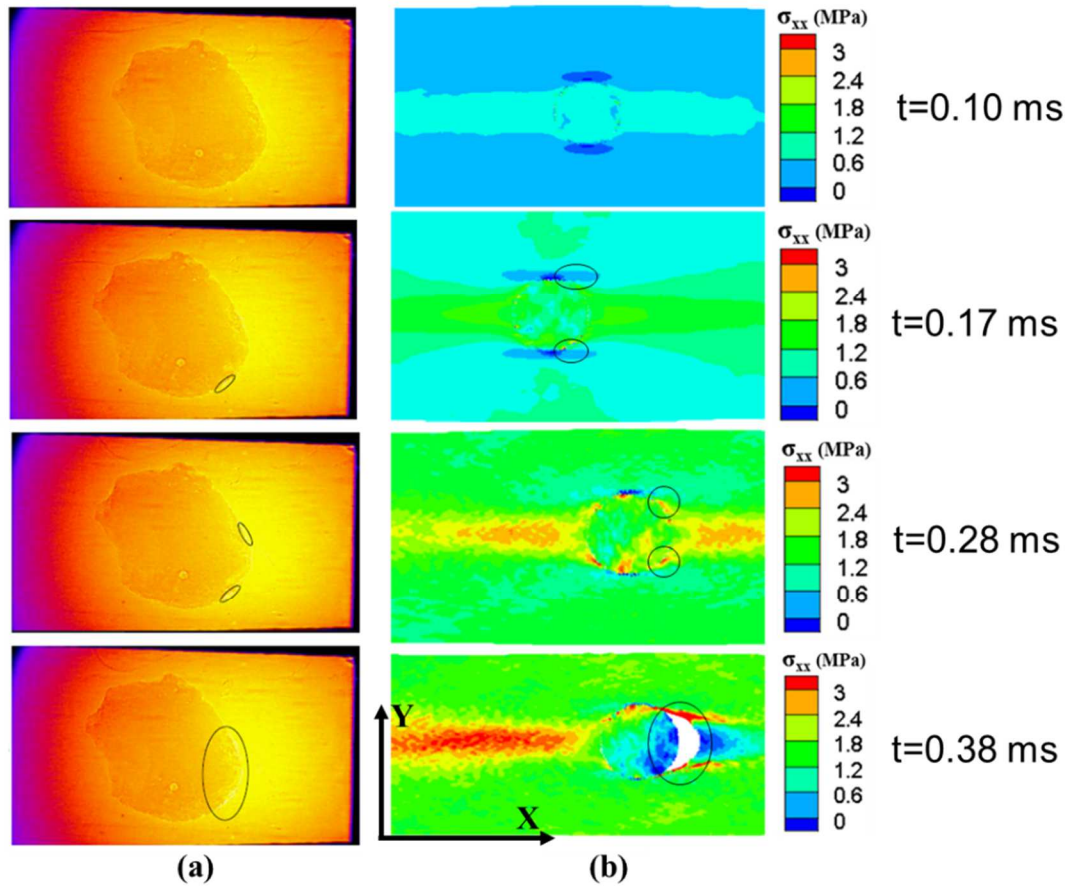


Figure 15 Interface separation evolution in the (a) Kolsky bar tension experiment [47] and (b) in the simulation as a function of time (sample type 1).

Figure 15 (a) shows the experimentally observed deformed state of the specimen during the loading process, compared with stress contours from the simulation, Fig. 15 (b). The time of debonding shown in the figure corresponds to the simulation. A complete comparison with the experiment cannot be made here as the loading profile in the experiment and simulation are different. Although the time required in each step shown in Fig. 15 were not equal in two cases, a qualitative comparison can be made here. The debonding initiates at a small interface region at an angle of -45° from the positive X-axis (see Fig. 15 (a)) first in the experiment while the remainder of the interface remains fully bonded. In the simulation (see Fig. 15(b)), we observe that the

debonding simultaneously initiates at 45° and 135° from the positive X-axis due to the symmetry of the geometry. Figure 16 shows the similarity in the opening mode of delamination observed in both numerical and experimental observations. The small delamination near the fixed end in the simulation is due to the reflected wave generated at the fixed end. However we do not see this in the experiment because it is a quasi-static tensile experiment.

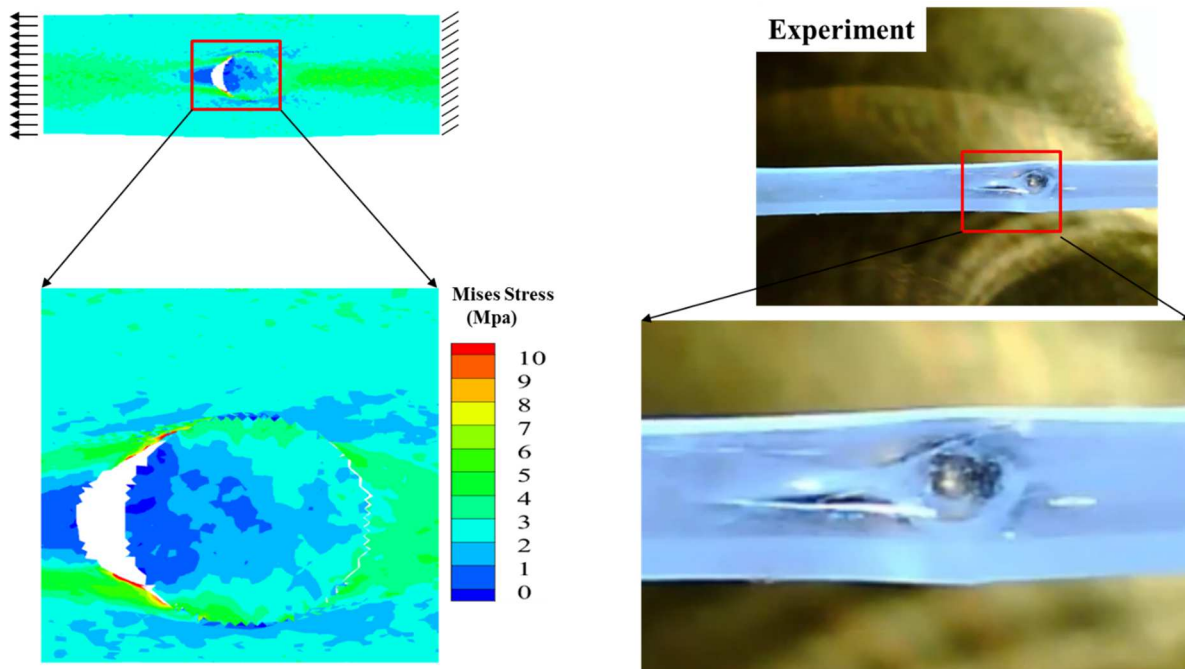


Figure 16 Validation of delamination mode obtained using CFEM with quasi-static experimental measurements (sample type 1).

The strain rate effect on deformation of the one particle samples were also investigated. Strain rates of 100, 200, 800, 1000, 2000, 3000 s^{-1} were applied in terms of the velocity boundary condition at the top boundary. Figure 17(a) shows the effect of strain rates on the cohesive energy of the system. Cohesive energy increases with time as the deformation increases, even when the cohesive zone parameters are constant. This is due to the fact that the material model used is a rate dependent viscoplastic material.

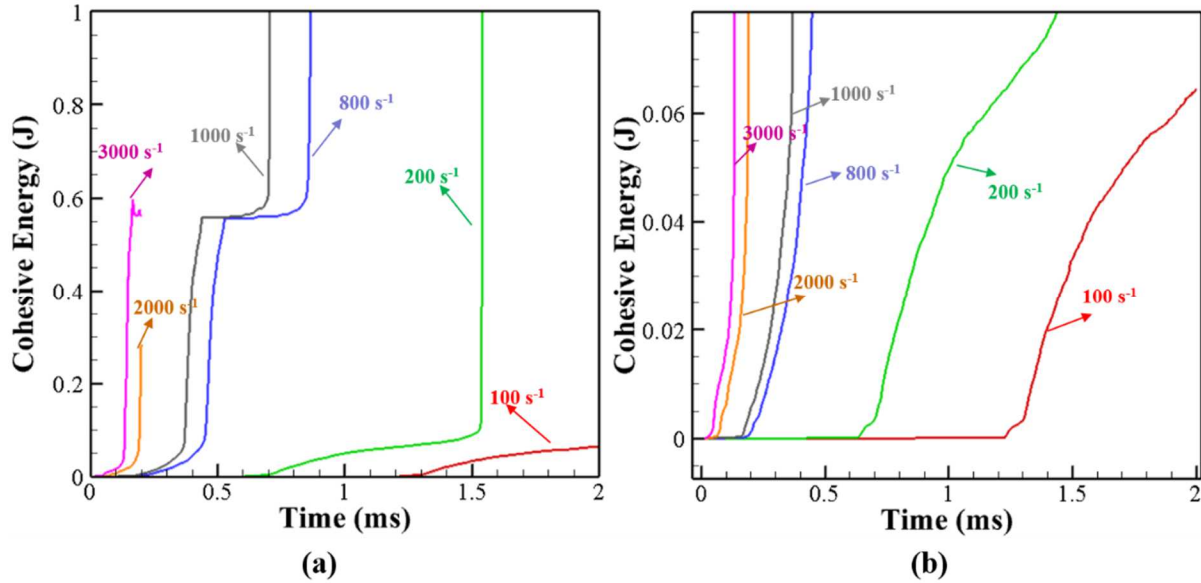


Figure 17 (a) Cohesive energy and (b) cohesive energy at failure with time for different strain rates (sample type 1) predicted using CFEM simulation.

Figure 17 (b) shows the effect of strain rates on the cohesive energy at the time when delamination starts. The delamination initiates when the cohesive energy at the interface reaches the critical value. As can be seen in the Fig. 17 (b), the time, at which the delamination initiation occurs, decreases with increasing strain rates. The rate at which the cohesive energy increases also increase with strain rate. Failure modes at each strain rates are shown in Fig. 18. The color map shows a failure index, *IFAIL*, which is a ratio of cohesive energy at the current time step and the critical cohesive energy. Delamination starts near the fixed boundary at low strain rates (800 s⁻¹ and 1000 s⁻¹). However, as the strain rate increases the delamination occurs on the loading side (3000 s⁻¹).

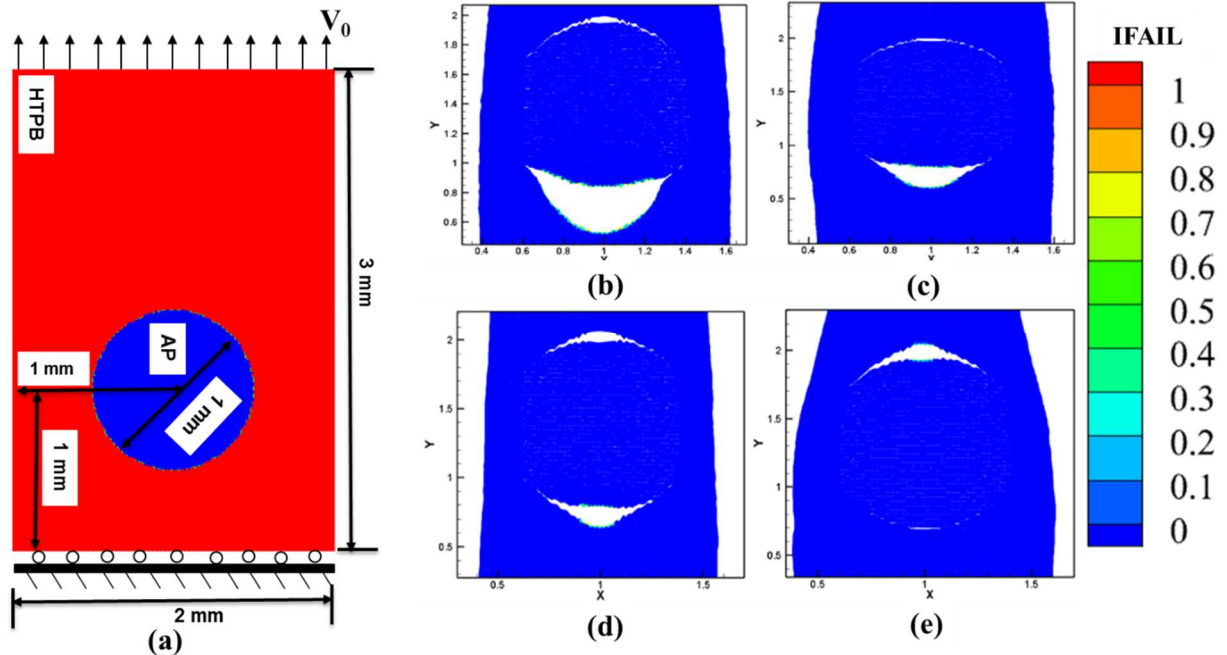


Figure 18 (a) HTPB-AP sample (type 1) tensile model for dynamic failure simulation and delamination mode at time $t = 0.4 \mu\text{s}$ for strain rates of (b) 800 s^{-1} (c) 1000 s^{-1} (d) 2000 s^{-1} (e) 3000 s^{-1} . IFAIL is the damage parameter used to represent fracture with a value of 1 indicating full separation and a value of 0 no separation [74].

The reason for this can be explained from the stress profile shown in Fig. 19, where the position of maximum stress is different for different strain rates. Both the normal (S22) and shear (S12) stresses are shown. The delamination initiation occurs due to the maximum shear stress at that position as shown in Fig. 19. Maximum shear stress occurs at 45° from the load axis (vertical axis, Fig. 18 (a)). The reason for different delamination position at high and low strain rates is due to the difference in the time rate of change of the material properties of the two constituent materials. The position of the delamination changes at different strain rates due to the difference in stress wave speed, which is a function of strain rate in the viscoplastic material region.

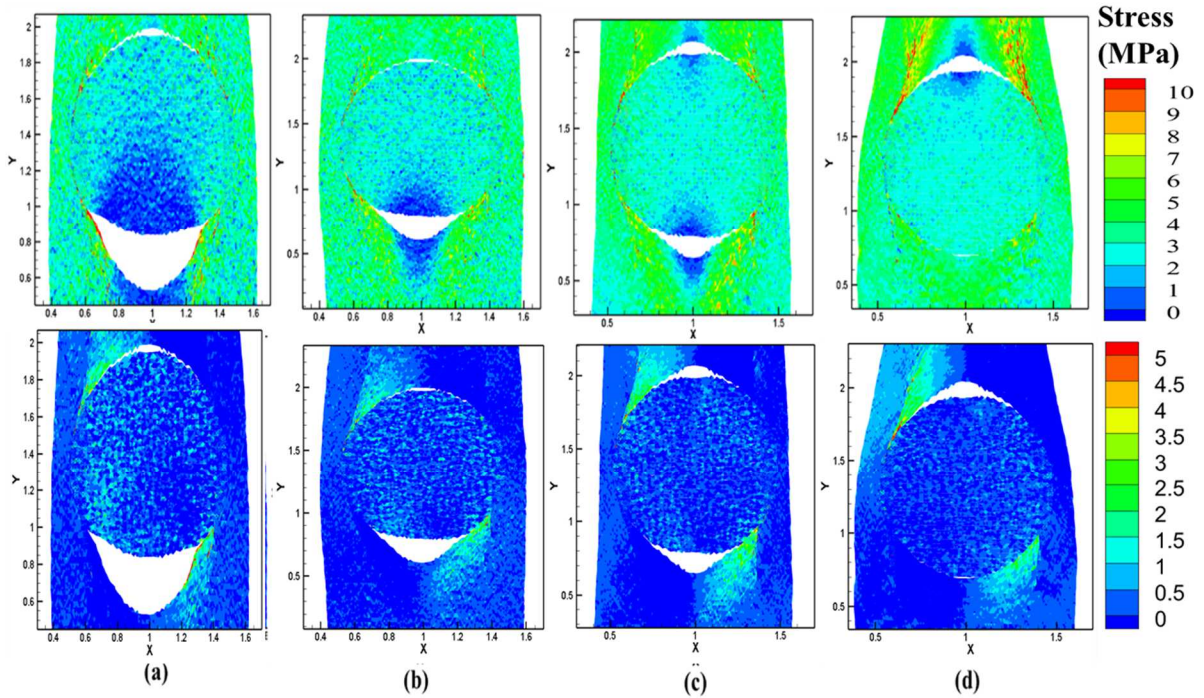


Figure 19 Stress contour for sample type 1 at strain rates (a) 800 s⁻¹ (b) 1000 s⁻¹ (c) 2000 s⁻¹ (d) 3000 s⁻¹ at time $t = 0.4 \mu\text{s}$. (First row- normal stress and Second row- shear stress)

The effect of interface chemistry is studied next. A series of single particle HTPB-AP models loaded in tension was simulated by changing the cohesive strength of the interface between the particle and matrix. In the previous section, it has been shown that the change in the interface chemistry changes the interface strength. In this work, the HTPB-AP interface cohesive strength used to study the effect is given in Table 3. Figure 20 (a) shows the effect of cohesive strength on the interface failure.

Table 3 Cohesive zone parameters for constituents of HTPB-AP composite for dynamic simulation.

Material/Interface	Cohesive Strength (MPa)	Critical Displacement (mm)	Cohesive Energy (N/mm)
HTPB	0.8	0.5	0.2
AP	2×10^3	5×10^{-3}	5.0
Interface	0.5-6	0.11	0.02-0.33

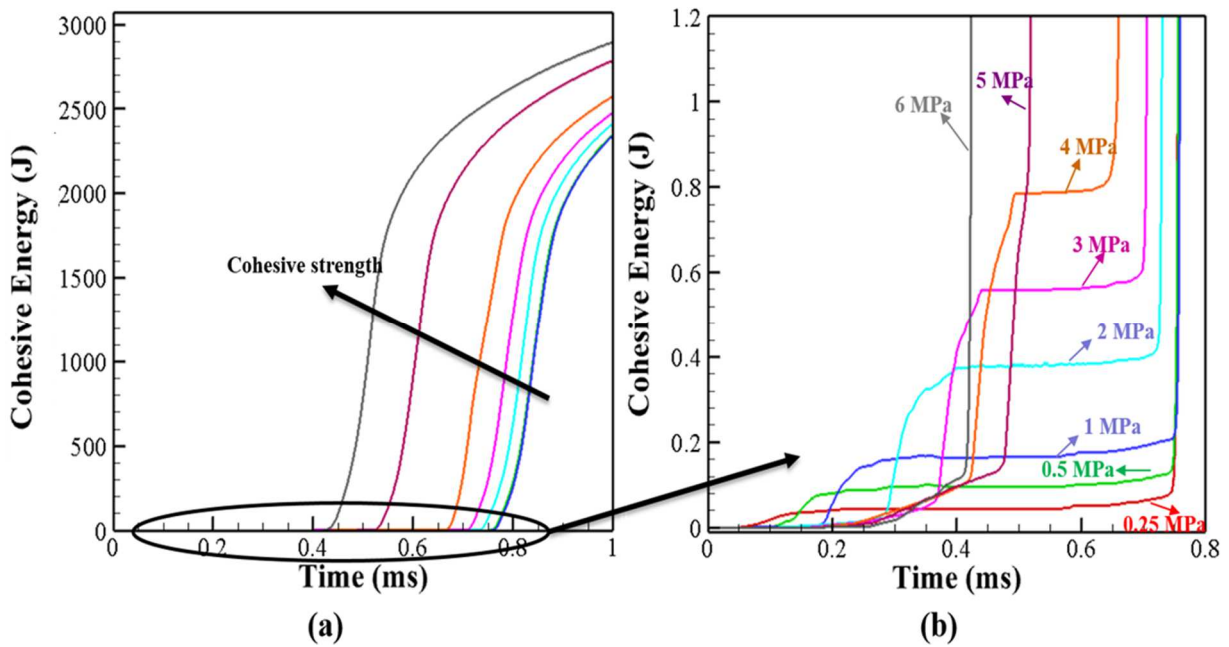


Figure 20 (a) Cohesive energy with time and (b) cohesive energy near the initiation of delamination for different cohesive strengths predicted using CFEM simulation.

As the cohesive strength increases, the time at which delamination starts increases. However, it is noted from Fig. 20 (b) that the rate at which the failure occurs also increases with the increase in cohesive strength. Figure 21 shows the effect of cohesive strength and strain rate on the time at which interface delamination starts. The time at which the HTPB-AP interface starts to delaminate increases linearly with the increase in cohesive strength (Fig. 21(a)). An exponential decrease is observed in the same with an increase in strain rate (Fig. 21(b)).

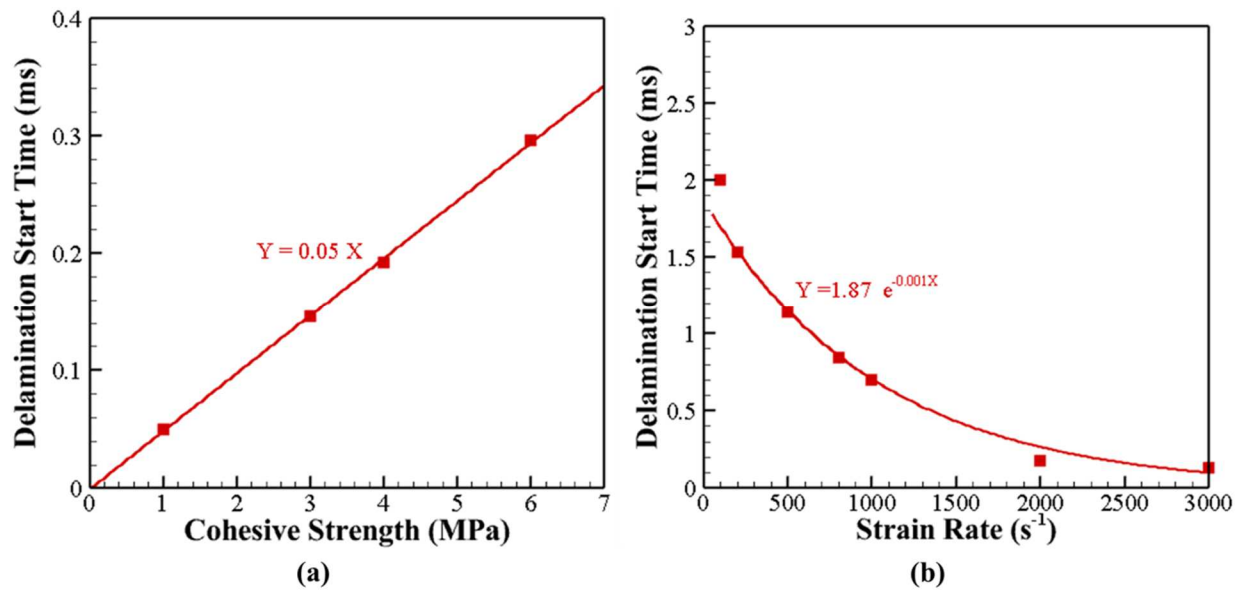


Figure 21 Effect of the (a) cohesive strength and (b) strain rate on the initiation time of delamination predicted using CFEM simulation.

1.4 Conclusions

A combined computational-experimental study of the fracture behavior of AP-HTPB energetic material under dynamic loading conditions is presented. The study considered the viscoplastic constitutive models of the composite constituents, which are obtained using nano-impact experiments. Quasi-static simulation was done in ABAQUS using a surface based cohesive zone model. The dynamic fracture behavior is simulated for the HTPB/AP sample with CFEM and

is qualitatively compared with the Kolsky bar tension experiment. The CFEM simulation accurately captures the initiation and mode of delamination. This has been confirmed by comparing it qualitatively with a quasi-static tensile experiment. Strain rate effects are considered and shown to affect the delamination in the sample. The effect of interface chemistry on delamination mode can eventually effect the possible hot-spots in the material as has been suggested by Yeager [12]. Further study would be needed to quantify this effect in multi-particle energetic materials. An important area of further investigation is the dynamic behavior of realistic energetic composite microstructures that incorporate many particles, which requires the use of multiscale approaches [89-91].

References

1. Gallier, Stany and Hiernard, Fabrice, *Microstructure of Composite Propellants Using Simulated Packings and X-Ray Tomography*. Journal of Propulsion and Power, 2008. **24**(1): p. 154-157.
2. Palmer, S.J.P., Field, J.E., and Huntley, J.M., *Deformation, Strengths and Strains to Failure of Polymer Bonded Explosives*. Proceedings of The Royal Society A: Mathematical, Physical and Engineering Science, 1993. **440**(1909): p. 399-419.
3. Rae, P.J., Goldrein, H.T., Palmer, S.J.P., Field, J.E., and Lewis, A.L., *Quasi-Static Studies of The Deformation and Failure of β -HMX Based Polymer Bonded Explosives*. Proceedings of The Royal Society A: Mathematical, Physical and Engineering Science, 2002. **458**(2019): p. 743-762.
4. Rae, P.J., Palmer, S.J.P., Goldrein, H.T., Field, J.E., and Lewis, A.L., *Quasi-Static Studies of The Deformation and Failure of PBX 9501*. Proceedings of The Royal Society A: Mathematical, Physical and Engineering Science, 2002. **458**(2025): p. 2227-2242.
5. Stacer, R.G., Hubner, C., and Husband, M., *Binder/Filler Interaction and The Nonlinear Behavior of Highly-Filled Elastomers*. Rubber Chemistry and Technology, 1990. **63**(4): p. 488-502.
6. Stacer, R.G. and Husband, M., *Small Deformation Viscoelastic Response of Gum and Highly Filled Elastomers*. Rheologica Acta, 1990. **29**(2): p. 152-162.
7. Fleming, K.A., Bird, R., Burt, M.W.G., and Whatmore, C.E. *The Influence of Formulation Variables on The Growth Of Reaction in Plastic Bonded Explosives*. In *Proceedings of The 8th International Detonation Symposium*, 1985. Albuquerque, NM, USA: Naval Surface Weapons Center, USA.
8. Kimura, E. and Oyumi, Y., *Shock Instability Test For Azide Polymer Propellants*. Journal of Energetic Materials, 1998. **16**(3): p. 173-185.
9. Khasainov, B.A., Ermolaev, B.S., Presles, H.N., and Vidal, p., *On The Effect of Grain Size on Shock Sensitivity of Heterogeneous High Explosives*. Shock Waves, 1997. **7**(2): p. 89-105.
10. Drodge, Daniel R. and Proud, William G., *The Effects of Particle Size and Separation on PBX Deformation*, AIP Conference Proceedings 2009. **1195**(1): p. 1381-1384.
11. Chen, Pengwan, Zhou, Zhongbin, and Huang, Fenglei, *Macro-Micro Mechanical Behavior of a Highly-Particle-Filled Composite Using Digital Image Correlation Method*. Advances in Composite Materials - Analysis of Natural and Man-Made Materials, Ed. Pavla Tesinova. 2011: Intech.

12. Yeager, John David, *Microstructural Characterization of Simulated Plastic Bonded Explosives*, in Mechanical and Materials Engineering. 2011, Washington State University: Washington.
13. Tvergaard, V. and Hutchinson, J. W., *The Relationship Between Crack Growth Resistance and Fracture Process Parameters In Elastic-Plastic Solids*. Journal of Mechanics and Physics of Solids, 1992. **40**(6): p. 1377-1397.
14. Tvergaard, V. and Hutchinson, J. W., *The Influence of Plasticity on Mixed Mode Interface Toughness*. Journal of Mechanics and Physics of Solids, 1993. **41**(6): p. 1119-1135.
15. Camacho, G.T. and Ortiz, M., *Computational Modeling of Impact Damage in Brittle Materials*. International Journal of Solids and Structures, 1996. **33**(20-22): p. 2899-2938.
16. Zhong, X. Allan and Knauss, W. G., *Analysis of Interfacial Failure in Particle-Filled Elastomers*. Journal of Engineering Materials and Technology, 1997. **119**(3): p. 198-204.
17. Zhong, Z. and Meguid, S.A., *On The Elastic Field Of A Spherical Inhomogeneity With An Imperfectly Bonded Interface*. Journal Of Elasticity, 1997. **46**(2): p. 91-113.
18. Zhong, X. Allan, *On The Stability Of Phase Separation In A Finite Solid With Interfaces*. Mechanics Of Advanced Materials and Structures, 1999. **6**(1): p. 1-7.
19. Zhong, X. Allan and Knauss, Wolfgang, *Effects of Particle Interaction and Size Variation on Damage Evolution in Filled Elastomers*. Mechanics of Advanced Materials and Structures, 2000. **7**(1): p. 35-53.
20. Barua, Ananda and Zhou, Min, *A Lagrangian Framework for Analyzing Microstructural Level Response of Polymer-Bonded Explosives*. Modelling and Simulation in Materials Science and Engineering, 2011. **19**(5): p. 055001.
21. Barua, A., Horie, Y., and Zhou, M., *Energy Localization in HMX-Estane Polymer-Bonded Explosives During Impact Loading*. Journal of Applied Physics, 2012. **111**(5): p. 054902.
22. Barua, A., Horie, Y., and Zhou, M., *Microstructural Level Response of HMX-Estane Polymer-Bonded Explosive Under Effects of Transient Stress Waves*. Proceedings of The Royal Society A: Mathematical, Physical and Engineering Sciences, 2012. **468**(2147): p. 3725-3744.
23. Barua, Ananda, Kim, Seok Pum, Horie, Yasuyuki, and Zhou, Min, *Computational Analysis of Ignition in Heterogeneous Energetic Materials*. Materials Science Forum, 2013. **767**(1): p. 13-21.
24. Barua, A., Kim, S., Horie, Y., and Zhou, M., *Prediction of Probabilistic Ignition Behavior of Polymer-Bonded Explosives From Microstructural Stochasticity*. Journal of Applied Physics, 2013. **113**(18): p. 184907.

25. Kim, Seokpum, Horie, Yasuyuki, and Zhou, Min, *Ignition Desensitization of PBX Via Aluminization*. Metallurgical and Materials Transactions A, 2014. **46**(10): p. 4578-4586.
26. Kim, S., Barua, A., Horie, Y., and Zhou, M., *Ignition Probability of Polymer-Bonded Explosives Accounting for Multiple Sources of Material Stochasticity*. Journal of Applied Physics, 2014. **115**(17): p. 174902.
27. Needleman, A. and Xu, X. P., *Void Nucleation by Inclusion Debonding in a Crystal Matrix*. Modelling and Simulation in Materials Science and Engineering, 1993. **1**(1): p. 111-132.
28. Kubair, Dharendra V., Geubelle, Philippe H., and Huang, Yonggang Y., *Analysis of a Rate-Dependent Cohesive Model for Dynamic Crack Propagation*. Engineering Fracture Mechanics, 2002. **70**(5): p. 685-704.
29. Kubair, Dharendra V., Geubelle, Philippe H., and Huang, Yonggang Y., *Intersonic Crack Propagation in Homogeneous Media Under Shear-Dominated Loading: Theoretical Analysis*. Journal of The Mechanics and Physics of Solids, 2002. **50**(8): p. 1547-1564.
30. Samudrala, O., Huang, Y., and Rosakis, A. J., *Subsonic and Intersonic Mode II Crack Propagation with a Rate-Dependent Cohesive Zone*. Journal of The Mechanics and Physics of Solids, 2002. **50**(6): p. 1231-1268.
31. Samudrala, O. and Rosakis, A. J., *Effect of Loading and Geometry on The Subsonic/Intersonic Transition of a Bimaterial Interface Crack*. Engineering Fracture Mechanics, 2003. **70**(2): p. 309-337.
32. Tan, H., *Viscoelastic Behaviors of Plastic-Bonded Energetic Materials Accounting for Nonlinear Interface Debonding*. 17th DYMAT Technical Meeting: The High Rate Mechanical Properties of Energetic Materials, Their Binder, or Simulants, Cavendish Laboratory, Department of Physics, University of Cambridge., 2007. p. 93-104.
33. Tan, H., *The Cohesive Law of Particle/Binder Interfaces in Solid Propellants*. Progress in Propulsion Physics, 2012. **2**(1): p. 59-66.
34. Tan, H., Huang, Y., and Geubelle, P. *An Energy Approach To a Micromechanics Model Accounting for Nonlinear Interface Debonding*. In *41st AIAA/ASME/SAE/ASEE Joint Propulsion Conference & Exhibit*. 2005. Tucson, Arizona.
35. Tan, H., Huang, Y., and Liu, C., *The Viscoelastic Composite with Interface Debonding*. Composites Science and Technology, 2008. **68**(15-16): p. 3145-3149.
36. Tan, H., Huang, Y., and Liu, C., *Effect of Nonlinear Interface Debonding on The Constitutive Model of Composite Materials*. International Journal for Multiscale Computational Engineering, 2006. **4**(1): p. 147-167.
37. Tan, H., Huang, Y., Liu, C., and Geubelle, P. H., *The Mori–Tanaka Method for Composite Materials with Nonlinear Interface Debonding*. International Journal of Plasticity, 2005. **21**(10): p. 1890-1918.

38. Tan, H., Huang, Y., Liu, C., Ravichandran, G., Inglis, H. M., and Geubelle, P. H., *The Uniaxial Tension of Particulate Composite Materials With Nonlinear Interface Debonding*. International Journal of Solids and Structures, 2007. **44**(6): p. 1809-1822.
39. Tan, Henry, Huang, Young, Liu, Cheng, Ravichandran, Guruswami, and Paulino, Glaucio H., *Constitutive Behaviors of Composites With Interface Debonding: The Extended Mori-Tanaka Method For Uniaxial Tension*. International Journal of Fracture, 2007. **146**(3): p. 139-148.
40. Tan, H., Liu, C., Huang, Y., and Geubelle, P., *The Cohesive Law for The Particle/Matrix Interfaces in High Explosives*. Journal of The Mechanics and Physics of Solids, 2005. **53**(8): p. 1892-1917.
41. Kulkarni, Mohan G., Geubelle, Philippe H., and Matouš, Karel, *Multi-Scale Modeling of Heterogeneous Adhesives: Effect of Particle Decohesion*. Mechanics of Materials, 2009. **41**(5): p. 573-583.
42. Agrawal, Paras M., Rice, Betsy M., and Thompson, Donald L., *Molecular Dynamics Study of The Melting of Nitromethane*. The Journal of Chemical Physics, 2003. **119**(18): p. 9617-9627.
43. Dawes, R., Siavosh-Haghighi, A., Sewell, T. D., and Thompson, D. L., *Shock-Induced Melting Of (100)-Oriented Nitromethane: Energy Partitioning and Vibrational Mode Heating*. The Journal of Chemical Physics, 2009. **131**(22): p. 224513.
44. Siavosh-Haghighi, A., Dawes, R., Sewell, T. D., and Thompson, D. L., *Shock-Induced Melting of (100)-Oriented Nitromethane: Structural Relaxation*. The Journal of Chemical Physics, 2009. **131**(6): p. 064503.
45. Siavosh-Haghighi, A., Sewell, T. D., and Thompson, D. L., *Molecular Dynamics Study of The Crystallization of Nitromethane From The Melt*. The Journal of Chemical Physics, 2010. **133**(19): p. 194501.
46. Gan, Ming and Tomar, V., *An in Situ Platform for The Investigation of Raman Shift In Micro-Scale Silicon Structures as a Function of Mechanical Stress and Temperature Increase*. Review of Scientific Instruments, 2014. **85**(1): p. 013902(1-10).
47. Hu, Ruize, Prakash, Chandra, Tomar, Vikas, Harr, Michael, Gunduz, Ibrahim Emre, and Oskay, Caglar, *Experimentally-Validated Mesoscale Modeling of The Coupled Mechanical-Thermal Response of AP-HTPB Energetic Material Under Dynamic Loading*. International Journal of Fracture, 2016. **203**(1-2): p. 1-22.
48. Wiegand, Jaames H., *Study of Mechanical Properties of Solid Propellant*. 1961, Armed Forces Technical Information Agency: Arlington.
49. Prakash, Chandra, Verma, Devendra, Exner, Matthias, Gunduz, Emre, and Tomar, Vikas, *Strain Rate Dependent Failure Of Interfaces Examined Via Nanoimpact Experiments*.

- Challenges In Mechanics Of Time Dependent Materials. Conference Proceedings of The Society for Experimental Mechanics Series, 2017.
50. Verma, Devendra, Exner, Matthias, and Tomar, Vikas, *An Investigation Into Strain Rate Dependent Constitutive Properties Of A Sandwiched Epoxy Interface*. Materials & Design, 2016. **112**(1): p. 345-356.
 51. Clayton, J.D., *Analysis Of Shock Compression of Strong Single Crystals With Logarithmic Thermoelastic-Plastic Theory*. International Journal of Engineering Science, 2014. **79**(1): p. 1-20.
 52. Rivlin, R. S., *Further Remarks on The Stress-Deformation Relations For Isotropic Material*. In Collected Papers of R.S. Rivlin: Volume I and II, Grigori Isaakovich Barenblatt and Daniel D. Joseph, Editors. 1997, Springer New York: New York, NY. p. 1014-1035.
 53. Truesdell, C., *The Simplest Rate Theory Of Pure Elasticity*. Communications on Pure and Applied Mathematics, 1955. **8**(1): p. 123-132.
 54. Khan, Akhtar S. and Huang, Sujian, *Continuum Theory Of Plasticity*. John Wiley & Sons, Inc. 1995.
 55. Dafalias, Y. F., *Issues On The Constitutive Formulation at Large Elastoplastic Deformations, Part I: Kinematics*. Acta Mechanica, 1987. **69**(1-4): p. 119-138.
 56. Thiruppukuzhi, Srikanth V. and Sun, C. T., *Models For The Strain-Rate-Dependent Behavior of Polymer Composites*. Composites Science and Technology, 2001. **61**(1): p. 1-12.
 57. Boyce, Mary C., Weber, G. G., and Parks, D. M., *On The Kinematics of Finite Strain Plasticity*. Journal of Mechanics and Physics of Solids, 1989. **37**(5): p. 647-665.
 58. Anastassakis, E., Pinczuk, A., Burstein, E., Pollak, F. H., and Cardona, M., *Effect of Static Uniaxial Stress On The Raman Spectrum of Silicon*. Solid State Communications, 1970. **8**(2): p. 133-138.
 59. De Wolf, Ingrid, *Micro-Raman Spectroscopy to Study Local Mechanical Stress in Silicon Integrated Circuits*. Semiconductor Science and Technology, 1996. **11**(2): p. 139-154.
 60. Brill, T. and Goetz, F. *Laser Raman Studies of Solid Oxidizer Behavior*. In *AIAA 14th Aerospace Sciences Meeting*. 1976. Washington, D.C.: American Institute of Aeronautics and Astronautics.
 61. Buback, M. and Schulz, K. R., *Raman Scattering of Pure Ammonia to High Pressures and Temperatures*. The Journal of Physical Chemistry, 1976. **80**(22): p. 2478-2482.

62. Chakraborty, T., Khatri, S. S., and Verma, A. L., *Temperature-Dependent Raman Study of Ammonium Perchlorate Single Crystals: The Orientational Dynamics of The Nh^{+4} Ions and Phase Transitions*. The Journal of Chemical Physics, 1986. **84**(12): p. 7018.
63. Fell, Nicholas F., Widder, Jeffrey M., Medlin, Stephen V., Morris, Jeffrey B., Pesce-Rodriguez, Rose A., and Mcnesby, Kevin L., *Fourier Transform Raman (FTR) Spectroscopy of Some Energetic Materials and Propellant Formulations Ii*. 1995, Army Research Laboratory: Aberdeen Proving Ground, MD. p. 34.
64. Lin, Y., Mao, W. L., Drozd, V., Chen, J., and Daemen, L. L., *Raman Spectroscopy Study of Ammonia Borane at High Pressure*. The Journal of Chemical Physics, 2008. **129**(23): p. 234509.
65. Nallasamy, P., Anbarasan, P. M., and Mohan, S., *Vibrational Spectra and Assignments of Cis- and Trans-1,4- Polybutadiene*. Turkish Journal of Chemistry, 2002. **26**(1): p. 105-111.
66. Ninet, S., Datchi, F., Saitta, A. M., Lazzeri, M., and Canny, B., *Raman Spectrum of Ammonia IV*. Physical Review B, 2006. **74**(10): p. 104101(1-11).
67. Peiris, Suhithi M., Pangilinan, G. I., and Russell, T. P., *Structural Properties of Ammonium Perchlorate Compressed to 5.6 GPa*, Journal of Physical Chemistry A, 2000. **104**(47): p. 11188-11193.
68. Winey, J. M., Gruzdkov, Y. A., Dreger, Z. A., Jensen, B. J., and Gupta, Y. M., *Thermomechanical Model and Temperature Measurements for Shocked Ammonium Perchlorate Single Crystals*. Journal of Applied Physics, 2002. **91**(9): p. 5650.
69. Wu, Xiaoming, Yu, Jianyuan, Ren, Tianling, and Liu, Litian, *Micro-Raman Spectroscopy Measurement of Stress in Silicon*. Microelectronics Journal, 2007. **38**(1): p. 87-90.
70. Fish, J., Oskay, C., Fan, R., and R., Barsoum, *Al 6061-T6-Elastomer Impact Simulation, Technical Report*. 2005, Rensselaer Polytechnic Institute.
71. Hui, T. and Oskay, C., *Computational Modeling Of Polyurea-Coated Composites Subjected to Blast Loads*. Journal of Composite Materials, 2012. **46**(18): p. 2167-2178.
72. Barenblatt, G.I., *The Mathematical Theory Of Equilibrium Cracks Formed In Brittle Fracture*. 1962, Armed Services Technical Information Agency: Arlington 12, Virginia.
73. Dugdale, D.S., *Yielding of Steel Sheets Containing Slits*. Journal of Mechanics and Physics of Solids, 1960. **8**(2): p. 100-104.
74. Tomar, Vikas, Zhai, Jun, and Zhou, Min, *Bounds for Element Size in a Variable Stiffness Cohesive Finite Element Model*. International Journal for Numerical Methods In Engineering, 2004. **61**(11): p. 1894-1920.

75. Zhai, J. and Zhou, M., *Finite Element Analysis of Micromechanical Failure Modes in a Heterogeneous Ceramic Material System*. International Journal of Fracture, 2000. **101**(1): p. 161-180.
76. Ortiz, M. and Pandolfi, A., *Finite-Deformation Irreversible Cohesive Elements for Three-Dimensional Crack-Propagation Analysis*. International Journal for Numerical Methods In Engineering, 1999. **44**(9): p. 1267-1282.
77. Zhai, Jun, Tomar, Vikas, and Zhou, Min, *Micromechanical Simulation of Dynamic Fracture Using The Cohesive Finite Element Method*. Journal of Engineering Materials and Technology, 2004. **126**(2): p. 179-.
78. Tomar, Vikas, *Insights Into The Effects of Tensile and Compressive Loadings on Microstructure Dependent Fracture of Trabecular Bone*. Engineering Fracture Mechanics, 2009. **76**(7): p. 884-897.
79. Wang, Z., Qiang, H., Wang, G. and Huang, Q., *Tensile Mechanical Properties and Constitutive Model For Htpb Propellant at Low Temperature and High Strain Rate*. Journal of Applied Polymer Science, 2015. **132**(24): p. 42104-42112.
80. Renganathan, K., Sarma, B. S. V. Rama, Rao, B. Nageswara, and Jana, M. K., *Tensile Fracture of HTPB Based Propellant Specimens*. Materials Science and Technology, 2013. **18**(11): p. 1408-1412.
81. Xu, F., Aravas, N., and Sofronis, P., *Constitutive Modeling of Solid Propellant Materials With Evolving Microstructural Damage*. Journal of The Mechanics and Physics of Solids, 2008. **56**(5): p. 2050-2073.
82. Kalaycioglu, Baris, Dirikolu, M. Husnu, and Çelik, Veli, *An Elasto-Viscoplastic Analysis Of Direct Extrusion of a Double Base Solid Propellant*. Advances in Engineering Software, 2010. **41**(9): p. 1110-1114.
83. Trumel, Harve, Dragon, andre, Fanget, Alain, and Lambert, Philippe, *A Constitutive Model for The Dynamic and High-Pressure Behaviour Of A Propellant-Like Material: Part II: Model Development and Applications*. International Journal for Numerical and Analytical Methods In Geomechanics, 2001. **25**(6): p. 581-603.
84. Trumel, Herve, Dragon, andre, Fanget, Alain, and Lambert, Philippe, *A Constitutive Model for The Dynamic and High-Pressure Behaviour of A Propellant-Like Material: Part I: Experimental Background and General Structure of The Model*. International Journal for Numerical and Analytical Methods in Geomechanics, 2001. **25**(6): p. 551-579.
85. Trumel, H., Fanget, A., and Deragon, A., *A Finite Strain Elastic-Plastic Model for The Quasi-Static Behaviour of Particulate Composites*. International Journal of Engineering Sciences, 1996. **34**(6): p. 677-698.

86. Tsai, J. and Sun, C.T., *Constitutive Model for High Strain Rate Response of Polymeric Composites*. Composites Science and Technology, 2002. **62** (10-11): p. 1289-1297.
87. Cady, C. M., Blumenthal, W. R., Gray, G. T., and Idar, D. J., *Mechanical Properties of Plastic-Bonded Explosive Binder Materials as a Function of Strain-Rate and Temperature*. Polymer Engineering & Science, 2006. **46**(6): p. 812-819.
88. Prasad, CH Devi Vara, Arunachalam, V., and Ranganathan, V., *Effect of The Formulation of Ingredients and The Process Parameters on The Fracture Toughness of HTPB Based Composite Solid Propellant*. Journal of Energy and Chemical Engineering, 2014. **2**(3): p. 94-105.
89. Hui, Tong and Oskay, Caglar, *A Nonlocal Homogenization Model for Wave Dispersion In Dissipative Composite Materials*. International Journal of Solids and Structures, 2013. **50**(1): p. 38-48.
90. Hui, Tong and Oskay, Caglar, *A High Order Homogenization Model For Transient Dynamics Of Heterogeneous Media Including Micro-Inertia Effects*. Computer Methods In Applied Mechanics and Engineering, 2014. **273**: p. 181-203.
91. Hui, Tong and Oskay, Caglar, *Laplace-Domain, High-Order Homogenization for Transient Dynamic Response of Viscoelastic Composites*. International Journal for Numerical Methods In Engineering, 2015. **103**(13): p. 937-957.

CHAPTER 2.
EXPERIMENTAL INTERFACE SHOCK VISCOSITY
MEASUREMENT IN AN ENERGETIC MATERIAL USING PULSE
LASER INDUCED PARTICLE IMPACT LOADING COMBINED
WITH MECHANICAL RAMAN SPECTROSCOPY

Chandra Prakash¹, I. Emre Gunduz², Vikas Tomar^{1*}

¹ School of Aeronautics and Astronautics, Purdue University-IN, 47907, USA

² School of Mechanical Engineering, Purdue University-IN, 47907, USA

*Corresponding author, Phone: (765)-494-3006 Fax: (765) 494-0307 Email: tomar@purdue.edu

Manuscript Under Preparation.

ABSTRACT

Experimental measurement of interface shock viscosity in a Hydroxyl-terminated polybutadiene (HTPB)-Ammonium Perchlorate (AP) material system are performed using mechanical Raman spectroscopy combined with laser pulse shock loading. First, HTPB-AP interface level shock wave propagation is studied using the cohesive finite element method (CFEM). The difference in the shock behavior of the analyzed HTPB-AP interfaces from that of the bulk AP and HTPB material is highlighted by numerical simulations of impacting a single AP particle in a HTPB-AP sample in three different ways: (1) a flyer plate is used to impact the whole HTPB-AP sample, (2) a flat impactor is used to impact the middle of AP particle embedded in HTPB matrix directly, and (3) a HTPB-AP interface is directly impacted with an impactor of radius 1 μm . Shock wave rise time at the interface is shown to differ for the three different impact modes. Based on the simulation results, a combined mechanical Raman spectroscopy and pulse laser induced particle impact test is used for measuring shock viscosity at HTPB-AP interfaces. It is observed that by changing the chemical composition of the interface, shock viscosity can be altered. A modified finite element model with viscous stress based on shock viscosity values added to the stress equation is then used for the shock impact simulation of a HTPB-AP material system. A power law relation was obtained between shock wave rise time and the shock viscosity. It is shown that the interface shock wave rise time increases with increasing interface shock viscosity.

KEYWORDS: HTPB; AP; Interface; Shock Viscosity; NMRS; CFEM

2.1 Introduction

Shock and vibration sensitivity of energetic materials (EM), such as high-energy explosives and propellants, has become an issue of increased concern. When a high-velocity impact launches a shock wave into an EM, a part of the mechanical energy gets converted into heat, which creates complex temperature and pressure profiles within the EM [1]. Due to the inhomogeneity (cracks, voids, interfaces etc.) present in the EM microstructure, shock energy gets accumulated near certain regions within the EM which leads to an increase in temperature. These regions of high energy spots are called hot-spots. In order to understand the mechanisms behind the hot-spots creation, a clear understanding of shock propagation in EM microstructure is required. Shock compression related temperature increase can be attributed to both compression and dissipation [2]. Solids, when compressed at high pressure, deform in a manner similar to fluids, which is considered to be a result of the concomitant motion of defects [3]. On the other hand, dissipative processes in the material in the shock regime are governed by material viscosity, called shock viscosity [4]. The shock viscosity is responsible for energy dissipation that control the rates of shear deformation as well as affects the temperature increase in the shocked material. Chhabildas et al. [5] have shown that the shock wave rise time can be used as a measure of shock viscosity. Many researchers have used experimental techniques such as VISAR [5-8], for shock wave rise time measurements in order to indirectly determine the shock viscosity. Kanel et al. [7] have observed from a VISAR experiment that the shock viscosity is significantly affected by the applied strain rate. Swegle and Grady [8] observed that for certain solids, the maximum strain rate in the plastic wave is proportional to the fourth power of the peak shock stress. Although such behavior in the case of steady shock waves has not been established [7]. Several researchers [7, 9, 10] have shown the dependence of the exponent in the power law relation between strain rate and shock stress on material properties, such as density, viscosity etc., as well as porosity, particle size

[9], the material heterogeneity [11] and the interface impedance mismatch [12]. The shock viscosity affects the shock wave rise time and a careful study of the wave profile at the interface can provide insights into the interface level shock wave behavior.

Several review articles [2, 13-17] have summarized experimental techniques for measuring dynamic yielding, index of refraction, and shock viscosity from the shock wave analysis data. Most of these properties can be related to shock velocity versus particle velocity behavior, as plotted as a Hugoniot relation. A large amount of literature is available for the study of shock wave propagation in bulk homogenous materials [1, 2, 5, 14, 18-23], as well as in composites [13, 24-31]. Zhuang et al. [12] have shown that in a layered structure, the role of the interface is to delay the shock stress to reach its maximum value. However, an explicit study of the shock behavior of the interface in composites has not yet been completed. In the previous studies, the authors have shown that the interfaces chemistry plays an important role in determining the overall mechanical behavior [32-34], as well as the failure of energetic materials [35, 36].

In this work, our goal is to propose an experimental technique to measure interface shock viscosity in a HTPB-AP material and use the measurements to analyze the influence of shock viscosity on interface level chemical composition dependent shock response. Constitutive behavior is obtained using interface level dynamic impact tests. Chemical composition dependent HTPB-AP interface separation properties are measured using in-situ mechanical Raman spectroscopy (MRS) experiments [35-37]. First, HTPB-AP interface level shock wave propagation is studied using the cohesive finite element method (CFEM). The difference in the shock behavior of the analyzed HTPB-AP interfaces from that of the bulk AP and HTPB material is highlighted by numerical simulations of impacting a single AP particle in a HTPB-AP sample in three different ways: (1) a flyer plate is used to impact the whole HTPB-AP sample, (2) a flat impactor is used to

impact the middle of AP particle embedded in HTPB matrix directly, and (3) a HTPB/AP interface is directly impacted with an impactor of radius 1 μm . Shock wave rise time at the interface is shown to differ for the three different impact modes. Based on simulation results, a combined mechanical Raman spectroscopy and pulse laser induced particle impact test is used for measuring shock viscosity at HTPB-AP interfaces. It is observed that by changing the chemical composition of the interface, shock viscosity can be altered. A modified finite element model with viscous stress based on shock viscosity values added to the stress equation is then used for the shock impact simulation of HTPB-AP material system.

The remaining part of this chapter is arranged as follows: Section 2 describes in brief, the nanoscale dynamic impact experiment and the *in-situ* MRS experiment. The CFEM approach including the details of the implementation of the material model are discussed in Section 3. In Section 4, the shock compression model validation and the results obtained from the simulations are described. Section-5 describes the details of the experimental technique based on a combined pulse laser and MRS. Thereafter, a summary of the results is presented in Section 6.

2.2 Experimental Methods

Two different types of experiments were performed: (1) dynamic impact to measure the strain rate dependent viscoplastic constitutive relations; and (2) *in-situ* MRS to measure the interface delamination properties [35, 36]. Energetic material samples consisted of single AP particle embedded in HTPB binder. The fabrication of single particle samples for the experiments are explained in detail in earlier work [37, 38]. Two types of HTPB-AP samples were fabricated: one without a binding agent (Sample 1) and other with a binding agent Tepanol (Sample 2). Several researchers have used viscoelastic [39, 40] as well as elasto-viscoplastic [41, 42] constitutive models for energetic materials. Especially, viscoplastic models are used frequently [43-45],

including Perzyna's viscoplastic model [42] for high strain rate loading conditions. In this work, the constitutive mechanical behavior of the materials, HTPB, AP and the HTPB-AP interface were modeled using a strain rate dependent power law viscoplastic model.

In order to characterize the rate dependent stress-strain behavior of material interfaces, experimental techniques with sufficient length and time scale resolution are needed. In this work a nanoscale impact experiment was used to obtain the high strain rate (up to 100 s^{-1}) stress-strain behavior of HTPB, AP and HTPB-AP interface. The nanoscale dynamic impact experiment used in this work is capable of performing precise impacts at the interfaces [46]. A detailed explanation of the experimental procedure and the analysis of the results are given in Prakash et al. [36]. Here, a brief overview of the procedure is outlined. This technique has been successfully used to obtain the mechanical properties of specific sites in the material such as at the interfaces at high strain rates [47]. An average strain rate for the impact is defined, in terms of the maximum depth (h_{max}) and the initial velocity (V_{in}), by the expression,

$$\dot{\epsilon} \approx \frac{V_{in}}{h_{max}}. \quad (28)$$

The strain (ϵ) and stress (σ) are then given as [37, 48],

$$\epsilon = \frac{h_{res}^2}{h_{max}^2} \quad \text{and} \quad (29)$$

$$\sigma = \frac{P}{\pi h_{max}^2},$$

where P is the applied load and h_{res} is the residual depth after the impacter leaves the sample.

Several impact experiments were performed to obtain multiple stress and strain relations as a

function of strain rates. The stress, strain and strain rate data is then fitted to define the material constitutive behavior [36], given by a power law viscoplastic constitutive model,

$$\bar{\epsilon}^{vp} = \chi \left(\dot{\bar{\epsilon}}^{vp} \right)^m (\bar{\sigma})^n. \quad (30)$$

Here, $\bar{\epsilon}^{vp}$ is the effective viscoplastic strain and $\bar{\sigma}$ is the equivalent stress. The parameters χ , m and n for the above viscoplastic model is given in Table for HTPB, AP and the interface for the two sample types. Here, Sample 1 is the HTPB-AP sample and Sample 2 is the HTPB-AP-Tepanol sample. Table 4 shows that the interface properties can be altered using a binding agent.

Table 4 Constitutive model parameters for bulk and interface obtained from nanoscale dynamic impact experiment [36].

Parameter		χ (MPa) ⁻ⁿ	m	n
HTPB		0.54	-0.18	1.8
AP		3.7E10	-9.8	5.9
HTPB/AP	Sample 1	1.0E5	-5.0	2.5
Interface	Sample 2	1.0E4	-4.2	2.0

As described in the next section, the impact induced failure is modeled using a bilinear cohesive zone model in the CFEM framework. A detailed explanation of the experimental procedure and the analysis of the results are given in Prakash et al. [36]. In order to obtain the interface cohesive zone parameters, Raman shifts in a HTPB-AP sample are measured, in-situ, using a Raman microscope with 532 nm laser wavelength using a 2400 grating size with a resolution of 1.4 cm⁻¹ (HORIBA Xplora Plus) [49]. TABLE 5 shows the cohesive zone parameters obtained from the in-situ MRS experiment of a single particle HTPB-AP tensile specimen loaded

until failure. The cohesive zone model parameters were obtained from a combination of stresses and energy spent in HTPB/AP delamination using a procedure outlined in [50].

Table 5 Cohesive zone model parameters for bulk and interface obtained from MRS experiment [36]

Material/Interface		Cohesive Strength (MPa)	Critical Displacement (mm)	Cohesive Energy (N/mm)
HTPB		0.8	0.5	0.2
AP		2×10^3	5×10^{-3}	5.0
Interface	Sample 1	1.1	0.12	0.065
	Sample 2	2.91	0.11	0.16

2.3 Cohesive Finite Element Method Framework

The CFEM model for the analysis of dynamic failure dates back to the work of Barenblatt [51] and Dugdale [52]. The current numerical framework is based on the framework of Prakash et al. [36] which uses an irreversible bilinear cohesive zone model to simulate fracture behavior. The cohesive zone model has been extensively used to model impact induced failure behavior in several materials, such as, polymers, metals, composites and fracture along interfaces [53]. As mentioned in the previous section, in-situ MRS is used to obtain the local cohesive zone parameters of the HTPB, AP and the HTPB-AP interface [36]. A CFEM model is created, Figure 22(a), for a single AP particle embedded in HTPB. The weak form of the cohesive finite element model is given by,

$$\int_V \boldsymbol{\tau} : \delta \mathbf{F} dV - \int_{S_{int}} \mathbf{T} \cdot \delta \boldsymbol{\Delta} dS = \int_{S_{ext}} \mathbf{T} \cdot \delta \mathbf{u} dS - \int_V \rho \frac{\partial^2 \mathbf{u}}{\partial t^2} \cdot \delta \mathbf{u} dV, \quad (31)$$

Here, $\boldsymbol{\tau}$ is the Kirchhoff's stress, \boldsymbol{F} is the deformation gradient, \boldsymbol{u} is the displacement, t is the time, V is the volume, S is the surface area, \boldsymbol{T} is the applied traction and $\boldsymbol{\Delta}$ is the surface separation, in the reference configuration, on material point on a cohesive surface. The cohesive zone parameters used in this study were obtained from the MRS experiment as explained in Section 2. The average time step in the simulation was taken to be of the order of 1 ns based on the Courant–Freidrichs–Lewy condition, which is a material dependent numerical stability criterion. This time step was considered in order to approximate the time in which the longitudinal wave traverse the smallest bulk element in at least ten steps as has been used in shock wave modeling by other researchers [54, 55]. In order to explicitly resolve the fracture path inside of the bulk material as well as at the interfaces, all of the element boundaries were considered to be cohesive surfaces, [53, 55]. The triangle elements were used in the mesh which enabled the model to be flexible for resolving crack pattern, Figure 22(a), [56].

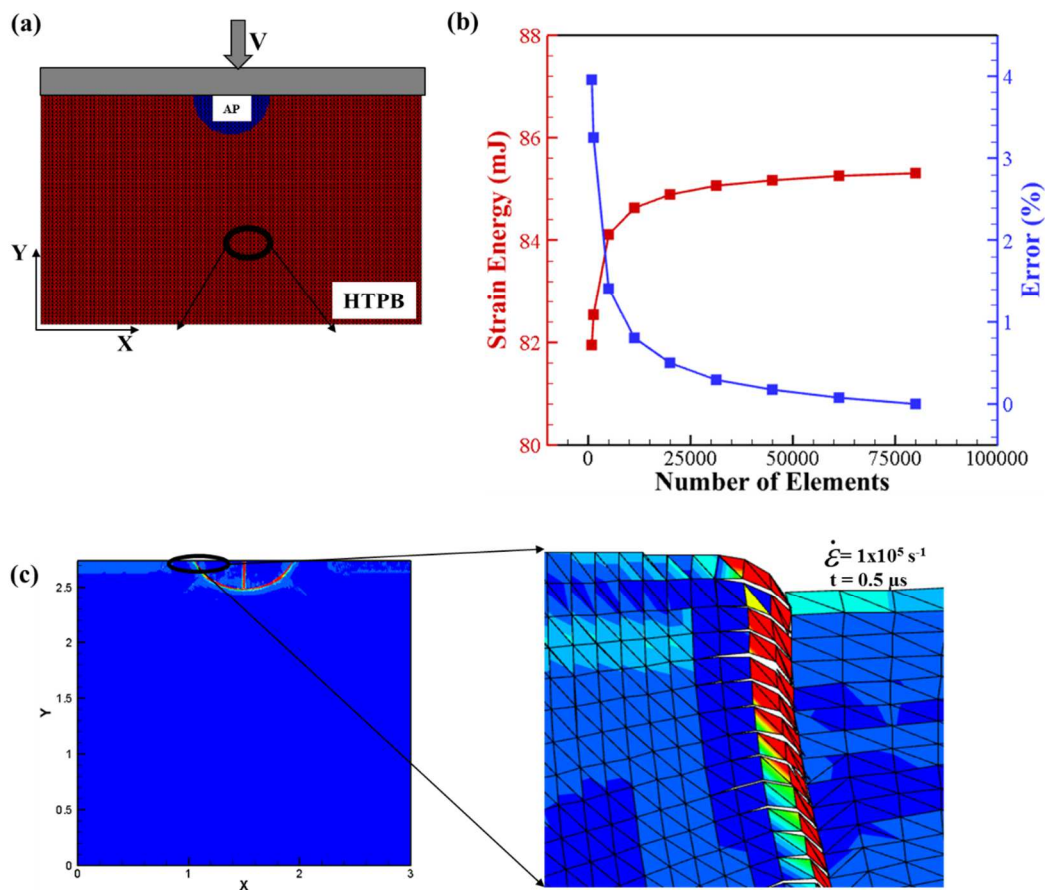


Figure 22 (a) Finite element mesh of a single particle AP-HTPB impact model and (b) mesh convergence analysis and (c) the element deformation near the interface at a strain rate of 10^5 s^{-1} at $0.5 \mu\text{s}$.

Mesh sensitivity study for dynamic deformation of a single particle HTPB-AP model was also performed under dynamic loading conditions, as shown in Figure 22(a). The size of the element in the interface region was taken to be 0.25 in order to include 4 elements along the thickness of the interface phase. By varying the number of elements in the bulk HTPB and AP phase, based on the convergence study, as shown in Figure 22(b), an average mesh size of $25 \mu\text{m}$ was chosen for the bulk HTPB and AP phases to ensure that the results obtained from the simulation remain independent of mesh size. A frictional cohesive contact model developed by Baek et al. [57] for large deformation impact is used to prevent the penetration between elements

due to impact. As can be seen in Fig. 22(c), the element penetration is insignificant even at $0.5 \mu\text{s}$ and impact strain rate of 10^5 s^{-1} .

2.3.1 Viscoplastic Constitutive Model

The utilized viscoplastic model is largely based on the work of Anand et al. [58-60]. However, in order to incorporate shock loading, a Mie-Gruneisen equation of state [61] is added. In this work, a standard multiplicative decomposition of the deformation gradient \mathbf{F} is used, i.e.

$$\mathbf{F} = \mathbf{F}^e \cdot \mathbf{F}^{vp} \quad (32)$$

Here, \mathbf{F}^e is the elastic deformation gradient and \mathbf{F}^{vp} a viscoplastic part of the deformation gradient. Also, since the heat dissipation cannot be measured experimentally, the viscoplastic model used in the current work neglects the heat dissipation. The velocity gradient tensor \mathbf{L} is decomposed into a rate of deformation, \mathbf{D} , and the spin tensor, \mathbf{W} , as,

$$\mathbf{L} = \dot{\mathbf{F}} \cdot \mathbf{F}^{-1} = \mathbf{D} + \mathbf{W}, \quad (33)$$

where \mathbf{D} and \mathbf{W} are defined as,

$$\begin{aligned} \mathbf{D} &= \frac{1}{2}(\mathbf{L} + \mathbf{L}^T) = \mathbf{D}^e + \mathbf{D}^{vp}, \quad \text{and} \\ \mathbf{W} &= \frac{1}{2}(\mathbf{L} - \mathbf{L}^T) = \mathbf{W}^e + \mathbf{W}^{vp} \end{aligned} \quad (34)$$

Here, \mathbf{D}^e is the elastic deformation rate related to the theory of hypo-elasticity and the constitutive law for \mathbf{D}^{vp} under finite deformations is given by the flow rule. The Jaumann objective rate is used in the model and the rate of Cauchy stress tensor is given as,

$$\hat{\boldsymbol{\tau}} = \dot{\boldsymbol{\tau}} - \mathbf{W} \cdot \boldsymbol{\tau} + \boldsymbol{\tau} \cdot \mathbf{W} \quad (35)$$

Based on the linear form of hypo-elasticity,

$$\hat{\boldsymbol{\tau}} = \mathbf{C} : [\mathbf{D} - \mathbf{D}^{vp}], \quad (36)$$

where \mathbf{C} is the stiffness tensor. For an isotropic material, the stiffness tensor is given by,

$$\mathbf{C} = \frac{E}{1+\nu} \left[\mathbf{I} + \frac{\nu}{1-2\nu} \mathbf{I} \otimes \mathbf{I} \right]. \quad (37)$$

Here, E is the Young's modulus, ν is the poisson ration and \mathbf{I} is the 3x3 identity matrix. The constitutive laws for the viscoplastic part of both \mathbf{D}^{vp} and \mathbf{W}^{vp} are required for a finite plastic deformations [62]. The flow rule for large deformation for an isotropic hardening solid, \mathbf{D}^{vp} , is given by,

$$D_{ij}^{vp} = \frac{\partial f}{\partial \tau_{ij}} \dot{\lambda} = \frac{3}{2\bar{\sigma}} \tau'_{ij} \dot{\lambda}, \quad (38)$$

where f is defined as the Mises yield function [63] and $\dot{\lambda}$ is equal to an effective viscoplastic strain rate, given by,

$$\dot{\lambda} = \sqrt{\frac{2}{3} D_{ij}^{vp} D_{ij}^{vp}} = \bar{\dot{\epsilon}}^{vp} = \frac{d\bar{\epsilon}^{vp}}{d\bar{\sigma}} \dot{\bar{\sigma}}, \quad (39)$$

$$\bar{\sigma} = \sqrt{\frac{3}{2} \tau'_{ij} \tau'_{ij}}, \quad \boldsymbol{\tau} = \boldsymbol{\tau}' - p\mathbf{I}, \quad (40)$$

and $\bar{\epsilon}^{vp}$ is the effective viscoplastic strain and is given by Eq. (32) as [36],

$$\bar{\epsilon}^{vp} = \chi \left(\bar{\dot{\epsilon}}^{vp} \right)^m \left(\bar{\sigma} \right)^n. \quad (41)$$

The parameters in Eq. (41) are evaluated by fitting the data obtained from the dynamic impact experiment given in Table . Using Eq. (40) and (41), substituting $\dot{\lambda}$ into Eq. (11), the viscoplastic deformation rate \mathbf{D}^{vp} is obtained. The time rate of change of effective stress, $\dot{\bar{\sigma}}$, given by differentiating Eq. (13),

$$\dot{\bar{\sigma}} = \frac{d\bar{\sigma}}{dt} = \frac{3}{2\bar{\sigma}} \tau'_{ij} \dot{\tau}'_{ij}, \quad (42)$$

where $\dot{\boldsymbol{\tau}}'_{ij}$ is the time rate of change of the deviatoric part of Kirchhoff's stress. The Kirchhoff's stress, $\boldsymbol{\tau}'_{ij}$, is composed of a deviatoric part $\boldsymbol{\tau}'_{ij}$, and a dilatational part (pressure) p , as given in Eq. (43). The pressure is calculated from a polynomial form of the Mie-Gruneisen equation of state as,

$$p = K\phi + A\phi^2 + B\phi^3 + \gamma(1 + \phi)e \quad (43)$$

where

$$\phi = \frac{\rho}{\rho_0} - 1 = \frac{1}{J} - 1 = \frac{1}{\det(\mathbf{F})} - 1,$$

e is the Internal Energy per unit Volume, γ is the Gruneisen parameter, K is the Bulk Modulus and, A , and B are parameters obtained by fitting a Hugoniot curve [31].

The time rate of change of the deviatoric part of Kirchhoff's stress, $\dot{\boldsymbol{\tau}}'_{ij}$, is obtained by equating Eq. (35) and Eq. (36), as,

$$\hat{\boldsymbol{\tau}}' = \dot{\boldsymbol{\tau}}' - \mathbf{W} \cdot \boldsymbol{\tau}' + \boldsymbol{\tau}' \cdot \mathbf{W} = \mathbf{C} : [\mathbf{D}' - \mathbf{D}^{vp'}], \quad (44)$$

which results in

$$\dot{\boldsymbol{\tau}}' = \hat{\boldsymbol{\tau}}' + \mathbf{W}^e \cdot \boldsymbol{\tau}' - \boldsymbol{\tau}' \cdot \mathbf{W}^e. \quad (45)$$

Here, it is assumed that the material is in a relaxed configuration which is not spinning, i.e., the viscoplastic spin rate $\mathbf{W}^{vp} = 0$, [64]. The deviatoric part of Kirchhoff's stress at the next time step, $t + \Delta t$, is then obtained from,

$${}^{t+\Delta t}\boldsymbol{\tau}'_{ij} = {}^t\boldsymbol{\tau}'_{ij} + \dot{\boldsymbol{\tau}}'_{ij} \cdot \Delta t. \quad (46)$$

2.4 CFEM Model Validation and Rise Time Prediction As a Function of Impact Position

First, the shock compression model is quantitatively validated by comparing the impact simulation results from a bulk AP sample impact experiments in literature [25]. After the model validation, the CFEM model is used to predict and identify the difference in interface shock

behavior by impacting HTPB-AP interfaces in three different ways: (1) a flyer plate is used to impact the whole HTPB-AP sample, (2) a flat impactor is used to impact the middle of AP particle embedded in HTPB matrix directly, and (3) a HTPB-AP interface is directly impacted with an impactor of radius 1 μm . Shock wave rise time at the interface is shown to differ for three different impact modes. Based on the simulation results, a combined mechanical Raman spectroscopy and pulse laser induced particle impact test is used for measuring the shock viscosity at the HTPB-AP interfaces. Based on the results of these three cases, an experimental method to characterize the interface shock viscosity is proposed. Next, this experimental setup is used to measure the interface shock viscosity of a single particle HTPB-AP sample with and without tepanol binding agent. Thereafter, a modified finite element model with viscous stress based on shock viscosity values added to the stress equation is used for the shock impact simulation of the HTPB-AP material system.

2.4.1 Shock Compression Model Validation

A CFEM model is developed to simulate the shock compression of HTPB-AP material as shown in Figure 233 (a). Mie-Gruneisen equation of state (EoS) parameters, given in Table 6, are used to calculate pressure using Eq. (33).

Table 6 Parameters used for Mie-Gruneisen equation of state [31]

	$K (10^5 \text{ MPa})$	$A (10^5 \text{ MPa})$	$B (10^5 \text{ MPa})$	γ	$\rho_0 \text{ g/cm}^3$
HTPB	0.02	0.294	0.0196	0.7	0.9
AP	0.15	0.225	0.1863	1.0	1.95

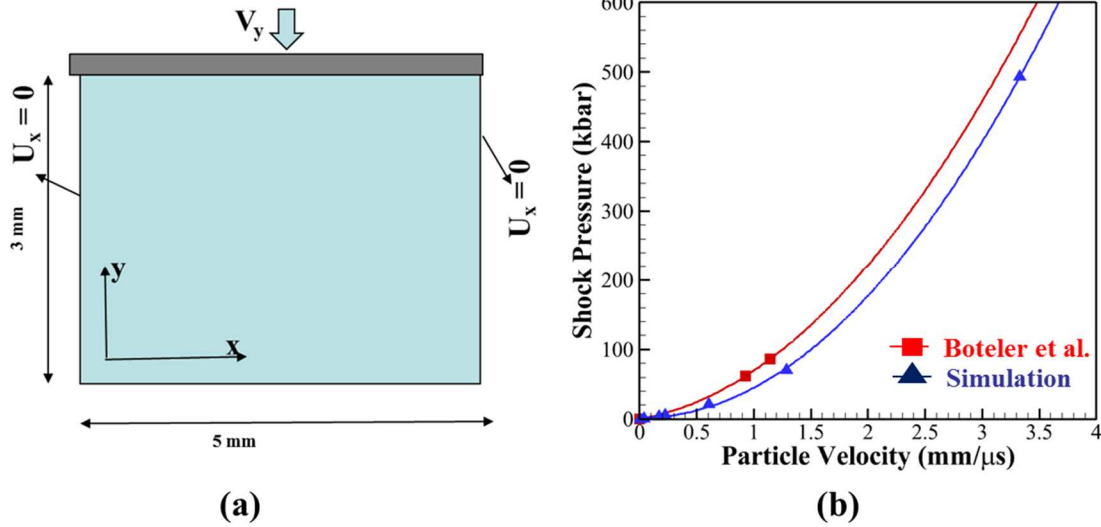


Figure 23 (a) Shock compression model and (b) comparison of the Hugoniot-curve obtained from experiment (Boteler et al., 1996) [25] and CFEM simulation.

As shown in Figure 233 (b), a close match between the experimental and simulated shock Hugoniot of AP validates the used CFEM model. The stress jump across the shock front was examined as a function of applied strain rate. Stress in the examined material varies with the strain rate following a power law relation as shown in Figure 24. The manner of the stress jump in the material due to the shock is consistent with the experimental results in literature [10], further providing the validation of the current shock compression model. Next, the shock compression model is used to study the interface shock behavior in a single particle HTPB-AP sample.

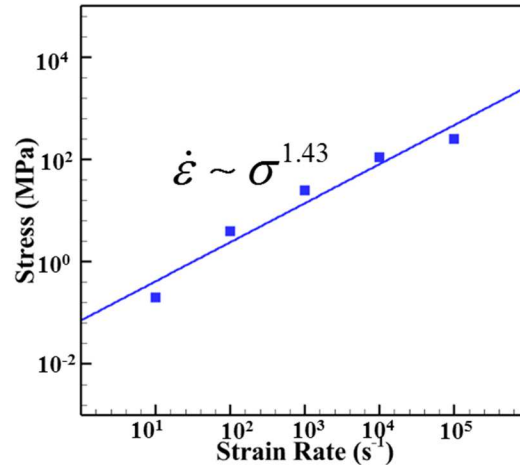


Figure 24 Stress-strain rate relation for AP

2.4.2 Interface Shock Wave Rise Time Prediction

The interface shock wave rise time behavior in the single particle HTPB/AP shock compression model is studied. A single particle sample model is shown in Figure 25. Three different cases are analyzed: particle impact (see Figure 25 (a)), interface impact (see Figure 25 (b)) and flyer plate impact (see Figure 25 (c)). The samples are impacted with velocities varying in the range of 0.3 m/s to 3000 m/s. The constitutive model parameters used in these simulation have been shown to be valid over this range in the case of AP in the previous section. The parameters for the HTPB and the HTPB-AP interface is also assumed to be valid over this range. In the simulations, parameters of shock wave propagation are recorded by monitoring the velocity and pressure histories at the HTPB-AP interface.

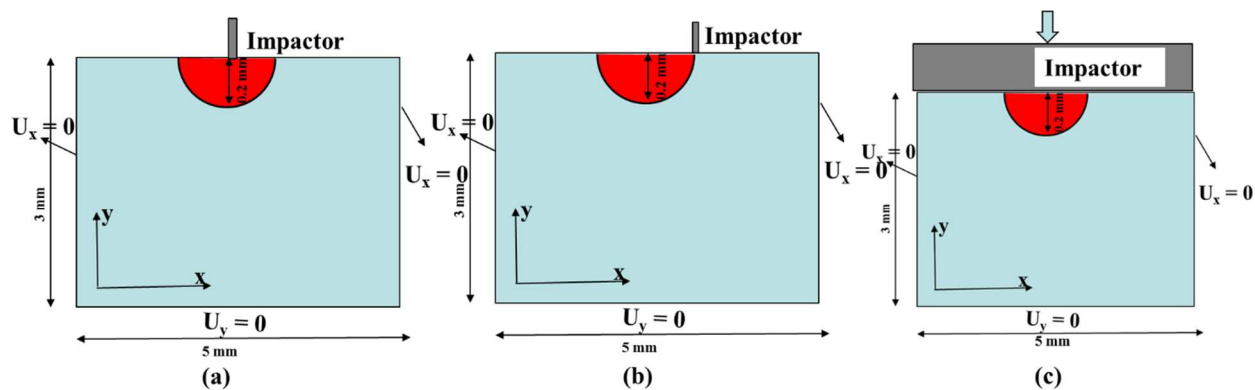


Figure 25 A single particle impact model for shock Hugoniot prediction with (a) a flat punch impact at the particle, (b) a flat punch impact at the interface, and (c) a flyer plate impact.

Figure 26 shows the shock wave propagation as a function of time in the analyzed HTPB-AP sample for the three different cases. As shown, stress concentration occurs at the interface in all of the cases. However, in Case a and Case c, the concentration is symmetric due to the symmetry of loading. In the interface impact Case b, stress wave follows the curved interface path.

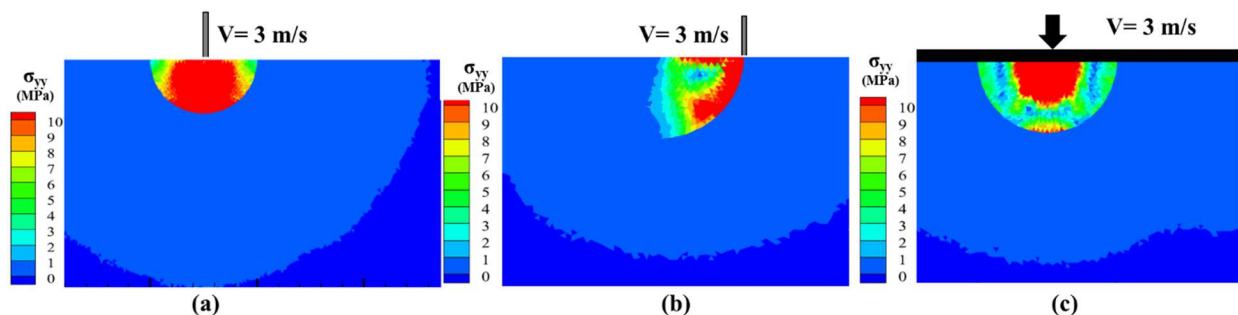


Figure 26 Shock stress wave profile for a strain rate of 1000 s^{-1} for (a) a flat punch impact at the particle, (b) a flat punch impact at the interface, and (c) a flyer plate impact.

Figure 27 shows the effect of impact position on the shock pressure. It can be seen that the pressure at the interface is low when impacted directly at the interface. As shown in Figure 28, the particle velocity at the interface increases with time and stays maximum in the case of interface level impact only. This is because the interface between HTPB and AP acts as a barrier to the stress

wave. When the shock wave reaches the interface, due to the mismatch between the impedances of HTPB and AP, a fraction of the shock bounces back from the interface. However, since a higher magnitude stress wave is approaching the interface from the top boundary (Fig. 26) and the stress being transmitted towards HTPB is limited due to the interface, a stress localization occurs. As can be seen in Fig. 26, stress is concentrated at the HTPB-AP interface in all of the cases. Due to the high stress localization, the shock energy gets localized at the interface which increases the possibility of higher interface dissipation and requires careful consideration.

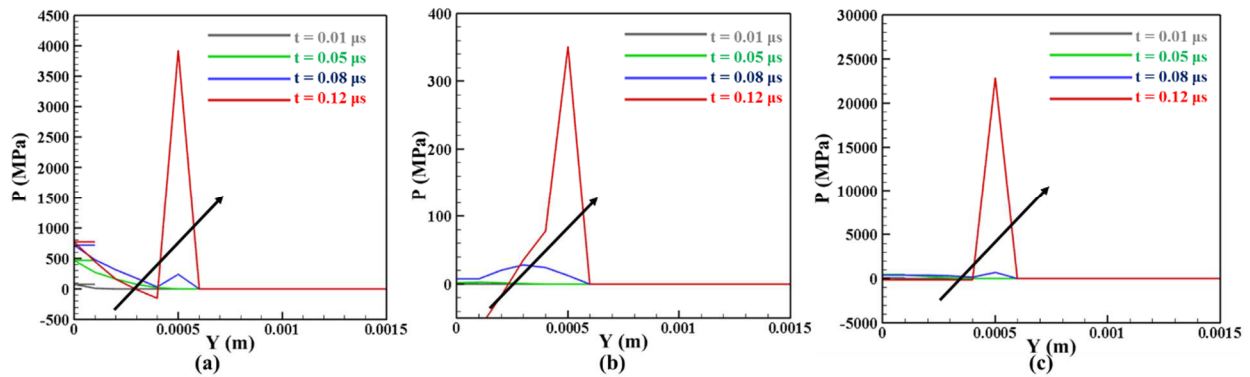


Figure 27 Shock pressure profile at the HTPB-AP interface at different time steps ($0.01 \mu\text{s}$ - $0.12 \mu\text{s}$) with an impact velocity of 300 m/s for (a) a flat punch impact at the particle, (b) a flat punch impact at the interface, and (c) a flyer plate impact.

Pressure at the interface is maximum when impacted by a plane wave, however the stress localization occurs over the entire interface. In the case of localized interface impact, the local stress is concentrated in only a particular section of the interface. This observation suggests that the interface is a critical position in the shock regime where stress localization is high.

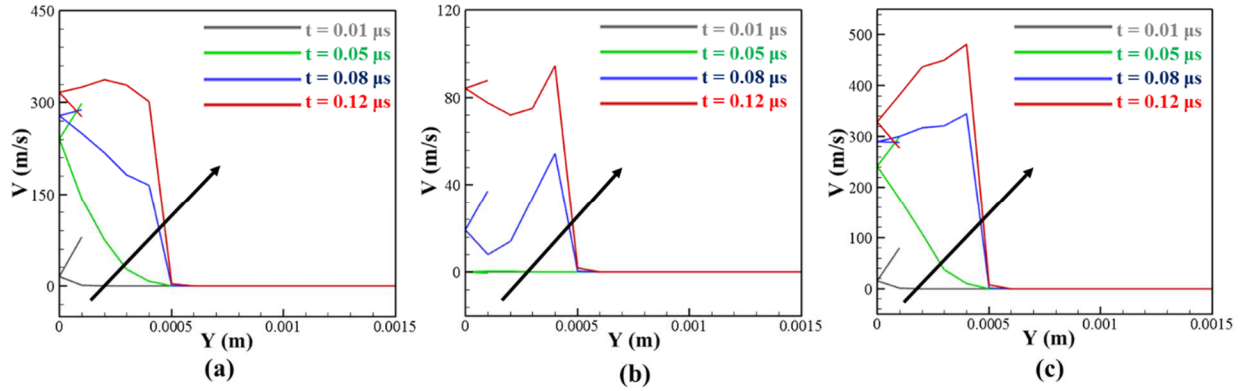


Figure 28 Interface particle velocity profile at the HTPB-AP interface at different time steps (0.01 μs -0.12 μs) with an impact velocity of 300 m/s for (a) a flat punch impact at the particle, (b) a flat punch impact at the interface, and (c) a flyer plate impact.

The variation of the shock wave rise time with the strain rate occurs due to shock energy dissipation in the material. The shock wave rise time is related to the shock viscosity, which affects the energy dissipation [5]. Shock wave rise time is calculated from the particle velocity profile as the time required for the velocity to reach a maximum value from the rest [8, 9]. Several researchers [5, 8, 10, 22] have used shock wave rise time for indirectly calculating the shock viscosity in solids. However, in this work, the focus is on the shock viscosity of the interfaces. As shown in Fig. 28, the interface particle velocity changes with the impact and so it is important to analyze the corresponding effect on the shock wave rise time. A representative interface particle velocity profile for a flyer plate impact on an HTPB-AP sample is shown in Fig. 29 (a) at different applied strain rate. The shock wave rise time is then calculated from this particle velocity profile. A corresponding interface shock wave rise time, Fig. 29 (b), shows a decrease with increasing applied strain rate.

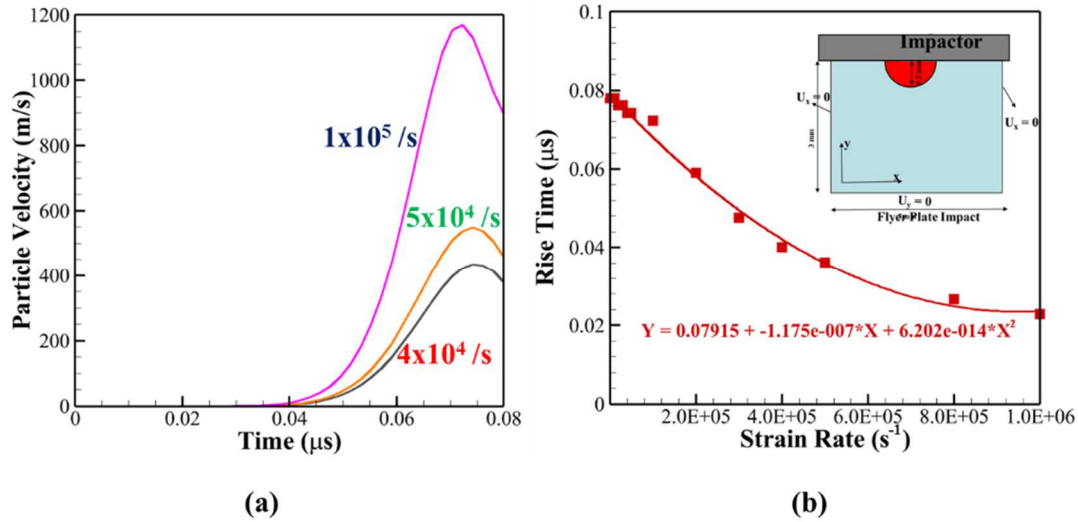


Figure 29 (a) A representative interface particle velocity at different applied strain rates and (b) shock wave rise time as a function of applied strain rate for flyer-plate impact on an HTPB-AP sample.

The shock Hugoniot relation is an important consideration as it provides a quantitative measurement of shock behavior, in the form of an equation of state. An equation of state with pressure (P) as a function of specific volume (v) in the form of $P=f(v)$ can be formed using the conservation of mass, energy and momentum principles to lead to a Hugoniot relation. The Hugoniot relation can be formed by relating any two of the following variables: Pressure (P), Shock velocity (U_s), Particle velocity (u_p) and the specific volume (v). In this work, the Hugoniot relation in the form of $P-u_p$ and U_s-u_p relation is used. Interface level Hugoniot curve for different impact positions, described and discussed earlier in Fig. 25, is shown in Fig. 30. A linear relation between U_s and u_p is found (see Figure 30 (a)) and P is a quadratic function of u_p as shown in Figure 30 (b). Since the pressure is a function of volumetric strain as well as of the strain energy, as can be seen in Fig. 30 (b), the difference in strain energy localization at the interface due to impact position changes the pressure. Similarly shock velocity also changes due to the limited shock wave transmitted at the interface. The pressure and shock velocity at the interface with the

impact velocity, see Fig. 30, indicates that the shock behavior of interface is dependent on the impact position.

In the previous Section 2.2 (TABLE 5), it was shown, that the interface chemical composition changes the interface strength. In the following, the influence of shock loading on shock wave rise time with interface strength varying in the range of 0.5 MPa to 100 MPa is analyzed using the CFEM incorporating equation of state described earlier.

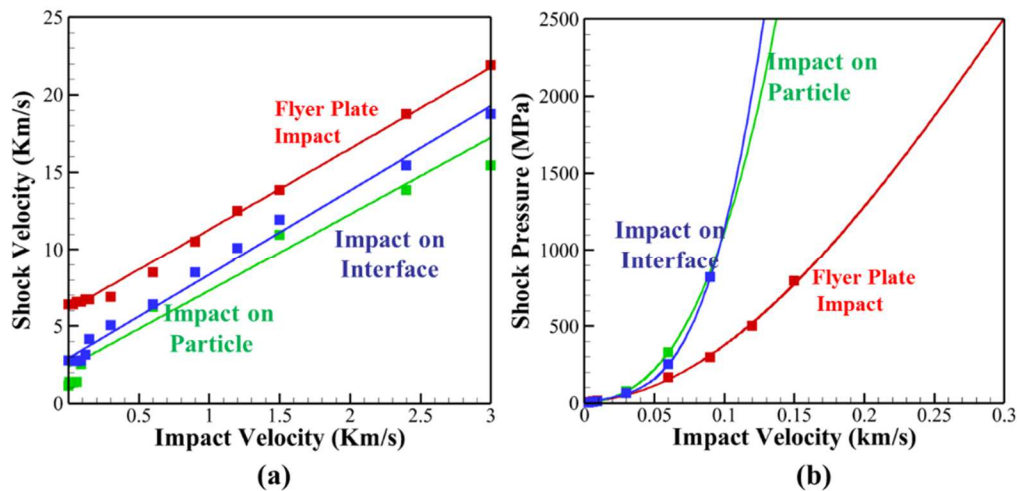


Figure 30 (a) Shock velocity as a function of the impact velocity and (b) shock pressure as a function of impact velocity as a function of impact position analyzed earlier in Fig. 4.

As shown in Figure 31, the shock wave rise time decreases with an increase in the strain rate as well as with an increase in the cohesive strength. A high cohesive strength increases the speed at which the shock wave passes through the interface and therefore decreases the shock viscosity. Figure 31 (a) shows that an increase in cohesive strength leads to a decrease in the shock wave rise time linearly. Clearly the higher interface strength decreases the time required for the shock induced interface level stress to reach the maximum value. This is due to the fact that a higher interface strength means a lower mismatch in the interface level impedance of the two material and therefore the shock wave can pass rapidly through the interface. Figure 31 (b) shows

the rise time as a function of applied strain rate which follows the same trend observed in bulk HMX by Sheffield et al. [9]. However, it is noted here that the impact position within the material changes the shock behavior at the interface. In case of a flyer plate impact the contribution of whole sample affects the shock behavior at the interface. Whereas, when impacted precisely at the interface, only the interface strength plays a role in the corresponding shock behavior.

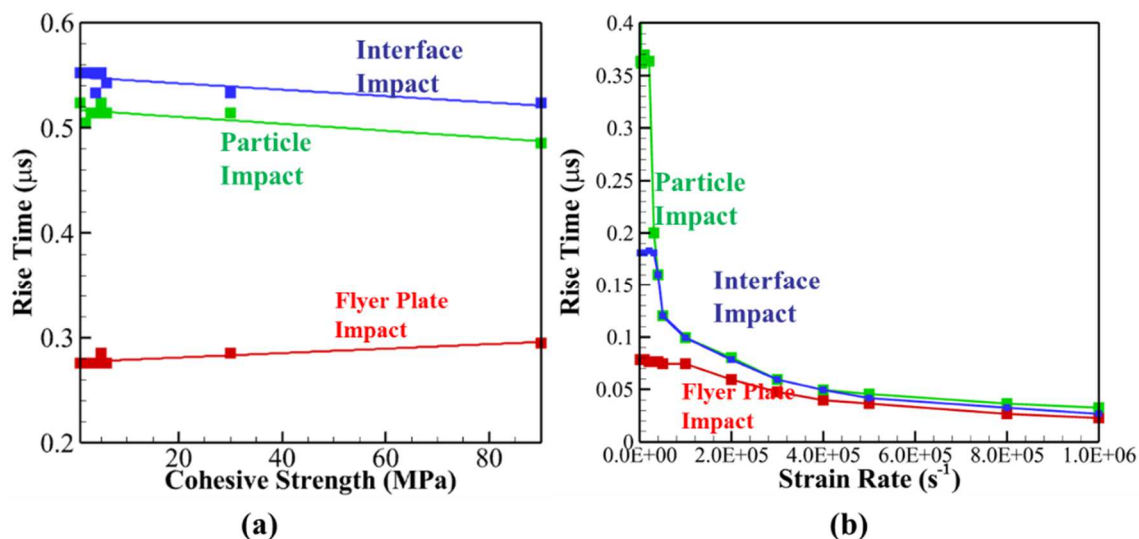


Figure 31 Shock wave rise time as a function of (a) cohesive strength and (b) strain rate as a function of impact position analyzed earlier in Fig. 4.

As discussed, the interface shock wave rise time depends on the mode of impact. The flyer plate impact and the particle impacts were found to give a lower shock wave rise time as compared to the direct interface impact. This means that the interface shock viscosity measured based on different impact modes will be different. What is important here is that most methods so far have not measured the stress required for interface viscosity measurements. Rather, the measurements have been indirect. Based on the observations made, it is clear that direct interface impact will lead to the highest impact energy localization at interface and the resulting dataset can be used for an

upper bound on the interface shock viscosity values. Therefore, in the next section a direct stress measurement based interface impact setup is described for measuring the shock viscosity.

2.5 Interface Shock Viscosity Measurement and its Effect on the Interface Rise time

2.5.1 Experimental Measurement of Interface Shock Viscosity

Shock viscosity is the ratio of the maximum stress to the applied strain rate [7]. In order to obtain the shock viscosity, direct measurements of localized stress and strain rate are required. In the previous section it was observed that for interface shock viscosity, a direct interface impact setup is required. In this section the required experimental setup and the measurement techniques are described.

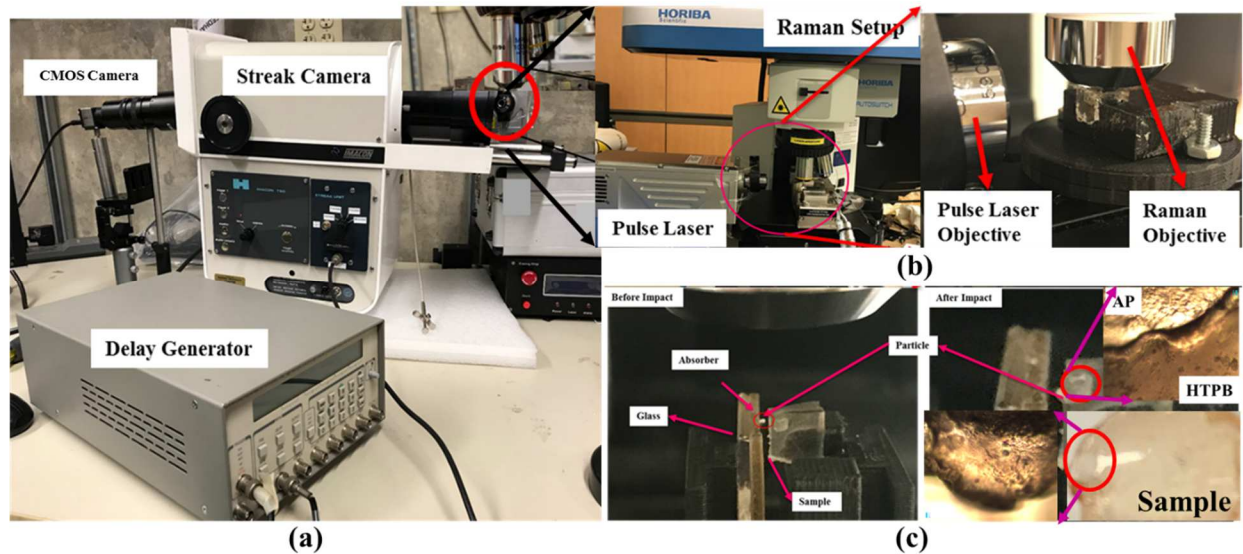


Figure 32 Experimental Setup for shock viscosity measurement. (a) Streak camera, delay generator and CMOS camera used for particle velocity measurement, (b) a combined pulse laser and MRS setup used for stress measurement and (c) a representative sample used in the particle impact experiment.

Shock viscosity, η , is given by [7],

$$\eta = \frac{\sigma}{\dot{\epsilon}} \quad (47)$$

where σ is the maximum stress that occurs in the material across the shock wave and $\dot{\epsilon}$ is the strain rate applied. The velocity of the accelerated particles, V , is measured using a streak camera and the strain rate is calculated as,

$$\dot{\epsilon} = \frac{V}{h}. \quad (48)$$

Here, h is the thickness of the sample. In the current experimental setup, a streak camera (IMACON 790), Fig. 32 (a), is used to measure the velocity of the particle used to impact the HTPB-AP interface. A pulse laser (1064 nm, 2.5 mJ pulse energy and 9 ns pulse width by Opto-engine LLC) setup is used to accelerate a Si particle that precisely impact HTPB-AP interfaces, Fig. 32 (c). Figure 33 (a) shows a schematic of the particle impact experiment. The pulse laser is focused on a glass substrate, on which an HTPB substrate is attached. A Si spherical particle of approximately $\sim 1 \mu\text{m}$ diameter (procured from Alfa Aesar) is placed on the HTPB substrate layer. When the laser is focused on the glass, the HTPB layer absorbs the energy and transfers it to the particle which then flies with a certain velocity (ranging from 1048 m/s to 1468 m/s) toward the sample. A local, *in-situ* stress at the interface where the impact occurs is measured using MRS as explained earlier in Section 2.

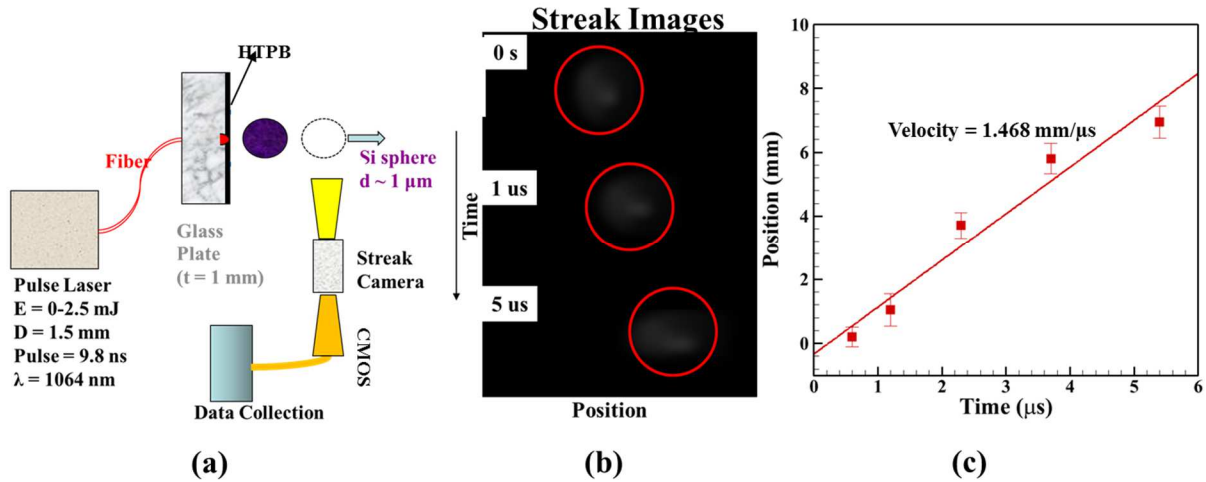


Figure 33 (a) Schematic of pulse laser induced particle impact and velocity measurement, (b) streak images and (c) velocity measurement from the streak images.

As shown in Fig. 33 (a), a high speed streak camera (IMACON 790) is used to collect the images of the particle flying towards the sample. The camera is continuously triggered by a delay generator (DG 535) and a CMOS camera attached with a zoom lens (Navitar 700). The images acquired by the CMOS camera is automatically saved on a computer using Thorcam software. Streak images of the particle, Fig. 33 (b), represents particle position as a function of time which is used to obtain the velocity V of the particle as the slope of the position vs. time line as shown in Fig. 33 (c). This procedure is repeated for different values of the laser pulse energy for the same size of particles in order to obtain different strain rates for precise impact of particles at HTPB-AP interfaces. Each experiment was repeated 5 times.

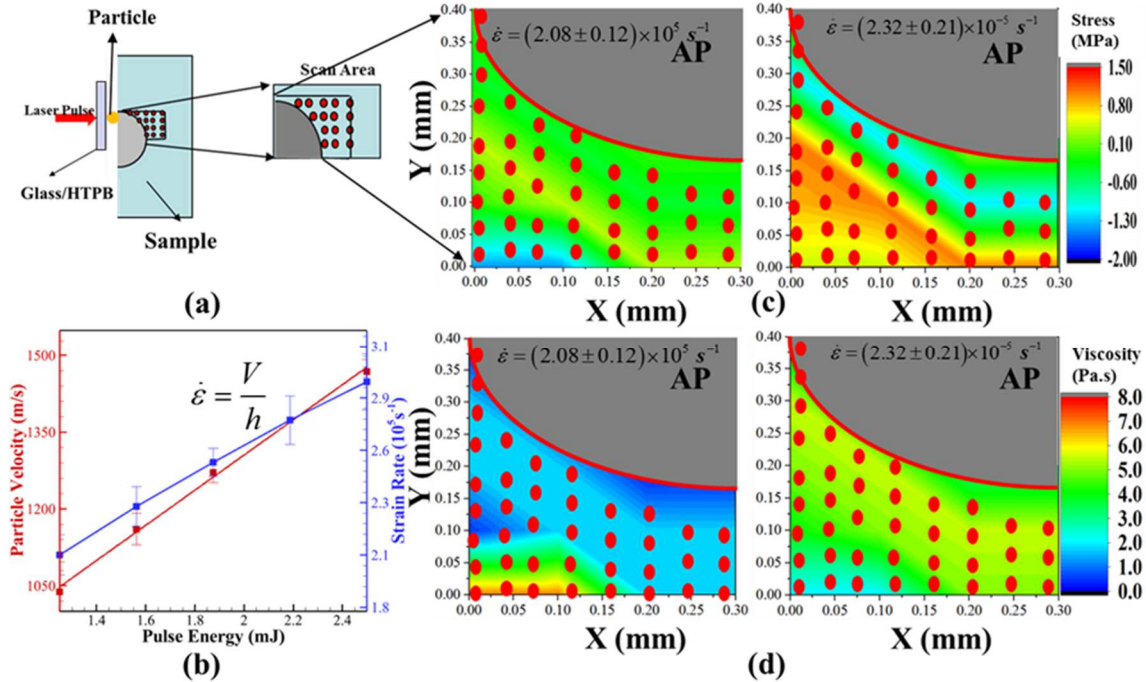


Figure 34 (a) Representative HTPB-AP impact sample, (b) particle velocity and strain rate at different pulse energy, (c) Stress obtained in the scan area using MRS and (d) shock viscosity in the scan area for HTPB-AP-Tepanol sample. Red dots are the positions where Raman spectra were recorded.

As shown in Fig. 32, the MRS setup is used in combination with the impact setup in order to measure stress *in-situ* at the HTPB-AP interfaces. Figure 34 (a) shows a representative interface impact setup of the HTPB-AP sample and the corresponding scan area near the interface. The velocity obtained from the streak camera images and the corresponding strain rates for increasing pulse energy used are shown in Fig. 34 (b). Figure 34 (c) shows the stress map obtained near the interface at two such strain rates. The interface shock viscosity is calculated using Eq. (47). It is to be noted here that the shock viscosity measured in this experiment is based on the stress measurement using an *in-situ* MRS setup, which is limited by the speed (1 ms/spectra) at which the Raman spectra is recorded whereas the shock period is only a few nanoseconds [65]. Within this time period, stress relaxation occurs and the measured stress will be lower than the value of

stress during shock. Because of this limitation the shock viscosity measured in this work will be a lower limit of the interface level shock viscosity. Shock viscosity measured in this work is also assumed to be independent of temperature. This is because the temperature increase due to Raman incident laser and that due to shock cannot be separated in the current experimental setup.

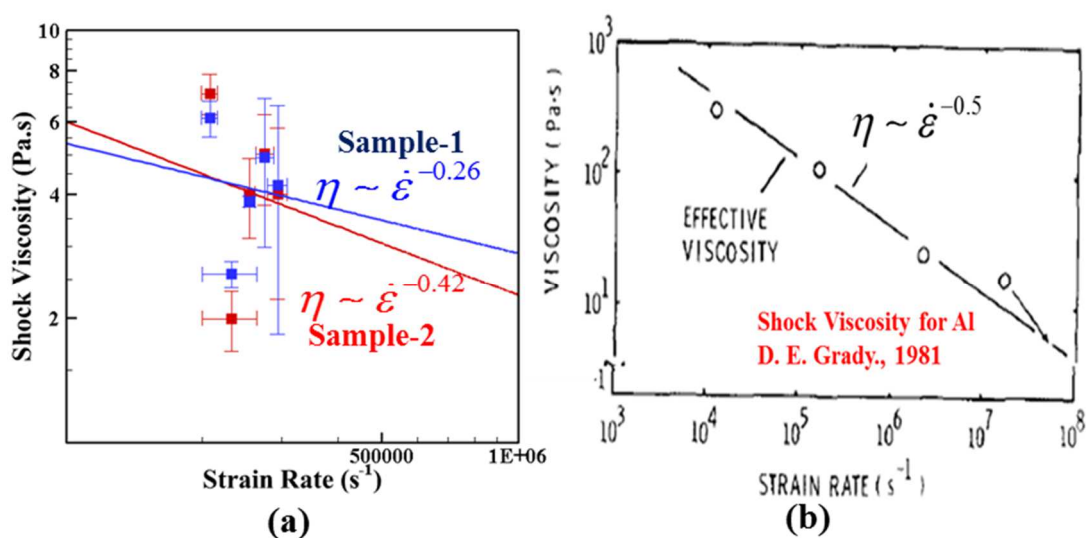


Figure 35 A qualitative comparison of (a) the interface shock viscosity measured using the current experimental setup for both samples (Sample 1 is without Tepanol and Sample 2 is with Tepanol) and (b) the shock viscosity for Al determined using the wave profile data obtained from VISAR (Reprinted with permission from [22]. Copyright (2018) AIP Publishing).

Based on the maximum stress obtained from the stress map in Fig. 34 (c) and the corresponding strain rate, a plot of the interface shock viscosity with respect to the applied strain rate is obtained, Fig. 35 (a). For both samples, with and without the binding agent, the shock viscosity is found to be in the range of 2 to 6 Pa.s. Since there is no available measured value of interface shock viscosity, a qualitative comparison of the current trend of shock viscosity as a function of strain rate is performed with that of the shock viscosity obtained for Al [22], as shown in Fig. 35 (b). The value for shock viscosity of HMX, as used by Benson et al. [61], is taken to be in the range of 0-30 Pa.s. However the shock viscosity values for metal are found in the range

of 0-500 Pa.s [65]. Kanel et al. [7] have also shown a similar trend of shock viscosity in Titanium with applied strain rate. The values for shock viscosity were observed to be in the range of 100-1000 Pa.s as a function of applied strain rate. D. E. Grady [10] has reviewed the shock behavior of several different materials, such as granular materials, composites, metals, etc., and have established an empirical power law relation between shock viscosity and the strain rate. However, the analysis used in these studies, to obtain shock viscosity, do not consider any local variation in the shock wave behavior because of the limitation in their experimental measurements. Also, in order to obtain shock viscosity, stress is calculated either from the shock Hugoniot relation or taken to be equal to the applied pressure [10]. These assumptions are not be valid in case of composite materials where impedance mismatch among constituent material will affect the shock wave propagation, as well as the local stress. The current work focuses on measuring the interface stress and the corresponding shock viscosity. As can be seen in Fig. 35 (a), interface shock viscosity shows a clear variation as a function of chemical composition. Next, the CFEM framework is used to predict effect of chemical composition dependent interface viscosity change on the resulting shock induced mechanical behavior of analyzed samples.

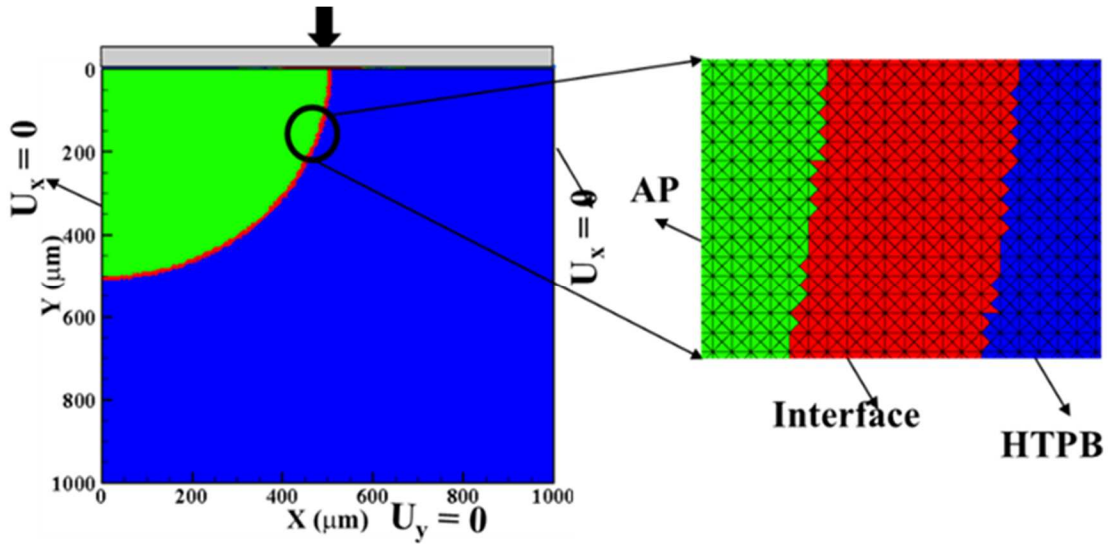


Figure 36 Single particle finite element model and corresponding mesh for the impact simulation.

2.5.2 Effect of Interface Shock Viscosity

The HTPB-AP model analyzed using the CFEM framework is shown in Fig. 36. The sample is impacted by a flyer plate and the interface shock wave is recorded as a function of time. The interface shock wave behavior is simulated using the viscoplastic constitutive model explained earlier in Section 2.1. However, now the total Kirchoff stress is modified to include viscous stress, as described earlier in the Eq. (40) as,

$$\boldsymbol{\tau} = \boldsymbol{\tau}' + \boldsymbol{\tau}^v - p\mathbf{I} \quad (49)$$

where, $\boldsymbol{\tau}_{ij}^v = \eta D_{ij}$ [61] and the pressure p is taken to be of the same form as shown earlier in Eq. (43). The interface shock viscosity was varied in the range from 0 Pa.s to 50 Pa.s [61], in order to understand the effect of shock viscosity term in the Eq. (49). The effect of strain rate variation on the interface shock behavior was also investigated by keeping the shock viscosity at a constant value equal to 6 Pa.s.

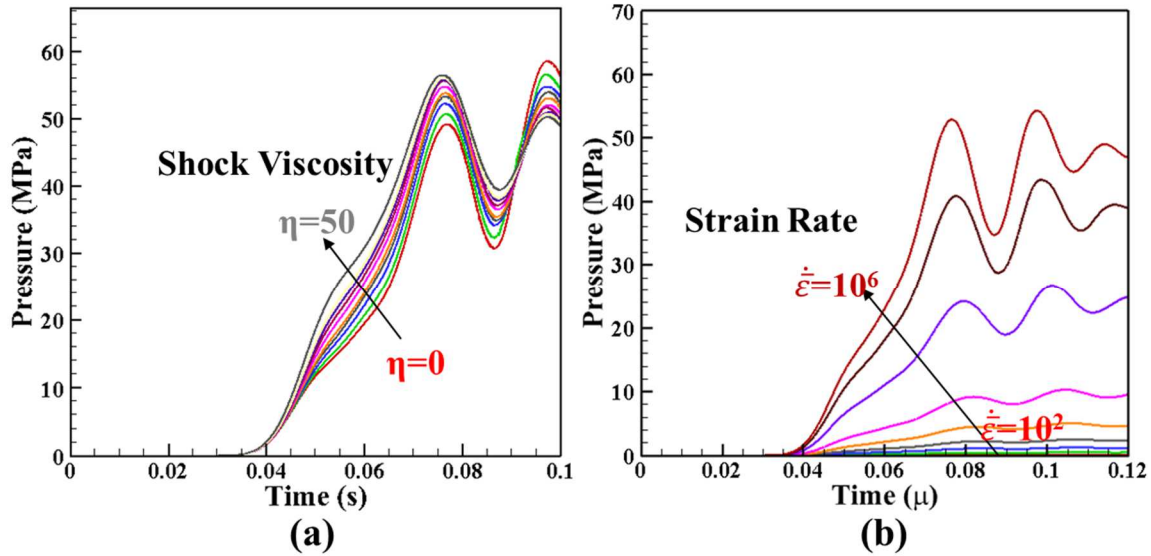


Figure 37 Shock pressure history at the interface as a function of (a) shock viscosity and (b) strain rate.

As shown in Fig. 37, the shock pressure recorded at a material point at the interface of HTPB-AP sample increases with increasing shock viscosity and strain rate. The material point, at which the pressure is plotted, is located at the left boundary ($X = 0 \mu\text{m}$) in the middle of the interface ($Y = 500.5 \mu\text{m}$). Pressure is a function of volumetric compression and the strain energy. An increase in strain rate increases the rate of compression which in turn increases the pressure. In the case of an increase in shock viscosity, the Kirchoff stress increases (Eq. (49)), which increases the strain energy at the interface as well as the pressure. The effect of interface shock viscosity and strain rate on the interface, shock wave rise time is shown in Fig. 38. The rise time increases with an increase in the interface shock viscosity (Fig. 38 (a)). For a given value of interface shock viscosity (6 Pa.s), the shock wave rise time at the interface shows a decrease with increasing strain rate (Fig. 38 (b)) as was observed in case of flyer plate impact without the viscous

stress model as well. However, the shock viscosity increases the rise time further as the shock stress becomes larger due to the increase shock front width.

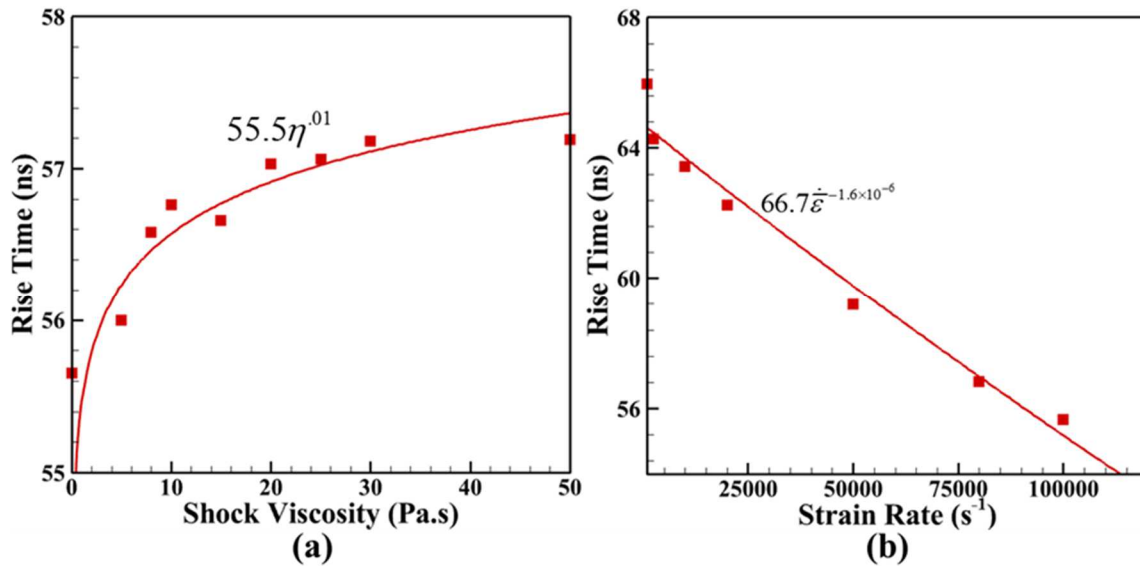


Figure 38 Shockwave rise time at the interface as a function of (a) shock viscosity at a constant strain rate of $100,000 \text{ s}^{-1}$ and (b) strain rate at a constant shock viscosity of 6 Pa.s .

2.6 Conclusions

This work establishes a novel experimental technique to measure interface shock viscosity in composite materials. Strain rate dependent viscoplastic power law model and the cohesive zone parameters obtained from the dynamic impact experiment and the in-situ MRS experiment, respectively, were used in a CFEM framework to simulate the shock loading. First the shock induced material behavior of interfaces under different impact conditions in a HTPB-AP EM is investigated. The interface shock wave rise time is obtained from the impact simulations at different strain rates. It was observed that a high cohesive strength leads to an increase in the speed at which the shock passes through the interface and a decrease in the shock wave rise time. It was also shown that the impact position changes the shock behavior of the interface and in order to obtain the interface shock viscosity, a standard flyer plate impact test may not be the best option.

Instead, a more suitable experiment would be to impact the interface directly and observe the interface level shock induced stress profile. Based on this observation, a pulse laser induced particle impact experiment was setup in combination to in-situ MRS measurements. A high-speed streak camera was used to measure the particle velocity as it impacts the sample interface and in-situ MRS was used to measure the stress at the material interface due to impact. A power law trend of the interface shock viscosity variation with strain rate was observed and a qualitative comparison with the shock viscosity of Al and other materials available in literature validated the experimental setup. A limitation of the current experimental setup is that the stress measurement is delayed due to the lower speed of Raman spectra being recorded by the spectrometer. This results in the measurement of only a lower limit of interface level shock viscosity. This limitation will be addressed in a future work. Next, a modified stress equation was used in order to include the effect of shock viscosity on the shock wave rise time and shock pressure in the CFEM framework. It was shown that increasing the interface shock viscosity increases the shock wave rise time at the interface.

Acknowledgements

The authors gratefully acknowledge the financial support from the Air Force Office of Scientific Research, Dynamic Materials and Interactions program (Grant No.: FA9550-15-1-0202, Program Manager: Dr. Martin Schmidt).

References

1. Bassett, Will P. and Dlott, Dana D., *Shock Initiation of Explosives: Temperature Spikes and Growth Spurts*. Applied Physics Letters, 2016. **109**(9): p. 091903.
2. Davidson, L. and Graham, R.A., *Shock Compression of Solids*. Physics Reports, 1979. **55**(4): p. 255-379.
3. Al Baida, Halim, Langlade, Cécile, Kermouche, Guillaume, and Ambriz, Ricardo Rafael, *Identifying The Stress–Strain Curve of Materials by Microimpact Testing. Application on Pure Copper, Pure Iron, and Aluminum Alloy 6061-T651*. Journal of Materials Research, 2015. **30**(14): p. 2222-2230.
4. Zel'dovich, Y B and Raizer, Y P, *Physics of Shock Waves and High-Temperature Hydrodynamic Phenomena*, Ed. Wallace Hayes. New York: Academic Press, 1967.
5. Chhabildas, Lalit C. and Asay, James R., *Rise-Time Measurements of Shock Transitions In Aluminum, Copper, and Steel*. Journal of Applied Physics, 1979. **50**(4): p. 2749-2756.
6. Stacer, R.G. and Husband, M., *Small Deformation Viscoelastic Response of Gum and Highly Filled Elastomers*. Rheologica Acta, 1990. **29**(2): p. 152-162.
7. Kanel, Gennady I., Savinykh, Andrey S., Garkushin, Gennady V., Pavlenko, Alexander V., and Razorenov, Sergey V., *Shock Wave Rise Time and The Viscosity of Liquids and Solids*. Mechanics for Materials and Technologies. Advanced Structured Materials, 2017. **46**: p. 257-263.
8. Swegle, J. W. and Grady, D. E. , *Shock Viscosity and The Prediction of Shock Wave Rise Times*. Journal of Applied Physics, 1985. **58**(2): p. 692-701.
9. Sheffield, S. A., Gustavsen, R. L., and Anderson, M. U., *Shock Loading of Porous High Explosives*. In High-Pressure Shock Compression of Solids IV: Response of Highly Porous Solids To Shock Loading, Lee Davison, Y. Horie, and Mohsen Shahinpoor, Editors. Springer New York: New York, NY, 1997. p. 23-61.
10. Grady, Dennis E., *Structured Shock Waves and The Fourth-Power Law*. Journal of Applied Physics, 2010. **107**(1): p. 013506.
11. Brown, J. L., Vogler, T. J., Grady, D. E., Reinhart, W. D., Chhabildas, L. C., Thornhill, T., *Dynamic Compaction Of Sand*. AIP Conference Proceedings, 2008. **955**(1): p. 1363-1366.
12. Zhuang, Shiming , Ravichandrana, Guruswami , and Grady, Dennis E. , *An Experimental Investigation of Shock Wave Propagation in Periodically Layered Composites*. Journal of The Mechanics and Physics of Solids, 2003. **51**(2): p. 245-265.
13. Grady, D. E., *Processes Occuring on Shock Wave Compression of Rocks and Minerals*, In High Pressure Research: Applications in Geophysics, M.H. Manghani and S. Akimoto, Editors. Academic Press: New York, 1977. p. 389-438.

14. Al'tshuler, L.V., *Use of Shock Waves in High-Pressure Physics*. Soviet Physics Uspekhi, 1965. **8**(1): p. 52-91.
15. Yakushev, V. V., *Electrical Measurement in a Dynamic Experiment*. Combustion, Explosion, and Shock Waves, 1978. **14**(2): p. 131-146.
16. Murri, W.J., Curran, D.R., Petersen, C.F., and Cewdson, R.C, *Response of Solids to Shock Waves*, In *Advances In High Pressure Research*. 1974, Academic Press: New York. p. 1-163.
17. Miller, G.H. and Arhens, T.J., *Shock Wave Viscosity Measurement*. Reviews of Modern Physics, 1991. **63**(4): p. 919-948.
18. Asay, J. R. and Lipkin, J., *A Self-Consistent Technique for Estimating the Dynamic Yield Strength of a Shock-Loaded Material*. Journal of Applied Physics, 1978. **49**(7): p. 4242-4247.
19. Barker, L. M. and Hollenbach, R. E., *Shock-Wave Studies of Pmma, Fused Silica, and Sapphire*. Journal of Applied Physics, 1970. **41**(10): p. 4208-4226.
20. Braisted, William and Brockman, Robert, *Finite Element Simulation of Laser Shock Peening*. International Journal of Fatigue, 1999. **21**(7): p. 719-724.
21. Clauer, Allan H., Holbrook, John H., and Fairand, Barry P., *Effects of Laser Induced Shock Waves on Metals*. In *Shock Waves and High-Strain-Rate Phenomena in Metals*, Marc A. Meyers and Lawrence E. Murr, Editors. 1981, Plenum Publishing Corporation: 233 Spring Street, New York, N.Y., 1981. p. 675-702.
22. Grady, D. E., *Strain-Rate Dependence of The Effective Viscosity Under Steady-Wave Shock Compression*. Applied Physics Letters, 1981. **38**(10): p. 825-826.
23. Graham, R.A., *Solids Under High Pressure Shock Compression*. High-Pressure Shock Compression of Condensed Matter, Ed. R.A. Graham. 1993, New York: Springer.
24. Bennett, Joel G., Haberman, Keith S., Johnson, James N., Asay, Blaine W., and Henson, Bryan F., *A Constitutive Model for The Non Shock Initiation and Mechanical Response of High Explosives*. Journal of Mechanics and Physics of Solids, 1998. **46**(12): p. 2303-2322.
25. Boteler, J. M. and Lindfors, A. J., *Shock Loading Studies of AP/AL/HTPB Based Propellants*. AIP Conference Proceedings, 1996. **370**(1): p. 767-770.
26. Khasainov, B.A., Ermolaev, B.S., Presles, H.N., and Vidal, P., *On The Effect of Grain Size on Shock Sensitivity of Heterogeneous High Explosives*. Shock Waves, 1997. **7**(2): p. 89-105.
27. Kimura, E. and Oyumi, Y., *Shock Instability Test for Azide Polymer Propellants*. Journal of Energetic Materials, 1998. **16**(2-3): p. 173-185.

28. Montross, Charles S., Wei, Tao, Ye, Lin, Clark, Graham, and Mai, Yiu-Wing, *Laser Shock Processing and Its Effects on Microstructure and Properties of Metal Alloys: A Review*. International Journal of Fatigue, 2002. **24**(10): p. 1021–1036.
29. Panchadhara, R. and Gonthier, K. A., *Mesoscale Analysis Of Volumetric and Surface Dissipation in Granular Explosive Induced by Uniaxial Deformation Waves*. Shock Waves, 2010. **21**(1): p. 43-61.
30. Schneider, Matthew S., Kad, Bimal, Kalantar, Daniel H., Remington, Bruce A., Kenik, Edward, Jarmakani, H., and Meyers, Marc A., *Laser Shock Compression of Copper and Copper–Aluminum Alloys*. International Journal of Impact Engineering, 2005. **32**(1-4): p. 473-507.
31. Reaugh, John E. and Lee, Edward L. *Shock Hugoniot Behavior of Mixed Phases With Widely Varying Shock Impedances*. In *Topical Conference on Shock Compression of Condensed Matter of The American Physical Society*. 1997. Amherst, MA.
32. Prakash, Chandra, Lee, Hongsook, Alucozai, Milad, and Tomar, Vikas, *An Analysis of The Influence of Grain Boundary Strength on Microstructure Dependent Fracture In Polycrystalline Tungsten*. International Journal Of Fracture, 2016. **199**(1): p. 1-20.
33. Qu, T., Prakash, C., and Tomar, V., *Relating Interface Properties With Crack Propagation in Composite Laminates*. International Journal of Materials and Metallurgical Engineering, 2016. **10**(6): p. 725-728.
34. Verma, Devendra, Prakash, Chandra, and Tomar, Vikas, *Properties of Material Interfaces: Dynamic Local Versus Nonlocal*, In *Handbook Of Nonlocal Continuum Mechanics For Materials and Structures*, Voyiadjis G., Editor, Springer, Cham, 2017.
35. Prakash, C., Gunduz , I. Emre, and Tomar, V. , *Effect of Strain Rate and Interface Chemistry on Failure in Energetic Materials*. Fracture, Fatigue, Failure and Damage Evolution, Conference Proceedings of The Society for Experimental Mechanics Series, 2018.
36. Prakash, Chandra, Gunduz, I. Emre, Oskay, Caglar, and Tomar, Vikas, *Effect of Interface Chemistry and Strain Rate on Particle-Matrix Delamination in an Energetic Material*. Engineering Fracture Mechanics, 2018. **191**: p. 46-64.
37. Prakash, Chandra, Verma, Devendra, Exner, Matthias, Gunduz, Emre, and Tomar, Vikas, *Strain Rate Dependent Failure of Interfaces Examined via Nanoimpact Experiments*. Challenges In Mechanics of Time Dependent Materials, **2**: Conference Proceedings of The Society For Experimental Mechanics Series, 2017.
38. Hu, Ruize, Prakash, Chandra, Tomar, Vikas, Harr, Michael, Gunduz, Ibrahim Emre, and Oskay, Caglar, *Experimentally-Validated Mesoscale Modeling of The Coupled Mechanical–Thermal Response of AP–HTPB Energetic Material Under Dynamic Loading*. International Journal of Fracture, 2016. **203**(1-2): p. 1-22.

39. Wang, Zhejun , Qiang, Hongfu , Wang, Guang , and Huang, Quanzhang, *Tensile Mechanical Properties and Constitutive Model for HTPB Propellant at Low Temperature and High Strain Rate*. Journal of Applied Polymer Science, 2015. **132**: p. 42104.
40. Renganathan, K., Sarma, B. S. V. Rama, Rao, B. Nageswara, and Jana, M. K., *Tensile Fracture of HTPB Based Propellant Specimens*. Materials Science and Technology, 2013. **18**(11): p. 1408-1412.
41. Xu, F., Aravas, N., and Sofronis, P., *Constitutive Modeling of Solid Propellant Materials With Evolving Microstructural Damage*. Journal of The Mechanics and Physics of Solids, 2008. **56**(5): p. 2050-2073.
42. Kalaycioglu, Baris, Dirikolu, M. Husnu, and Çelik, Veli, *An Elasto-Viscoplastic Analysis of Direct Extrusion of a Double Base Solid Propellant*. Advances In Engineering Software, 2010. **41**(9): p. 1110-1114.
43. Trumel, Harve, Dragon, Andre, Fanget, Alain, and Lambert, Philippe, *A Constitutive Model For The Dynamic and High-Pressure Behaviour of a Propellant-Like Material: Part Ii: Model Development and Applications*. International Journal For Numerical and Analytical Methods In Geomechanics, 2001. **25**(6): p. 581-603.
44. Trumel, Herve, Dragon, Andre, Fanget, Alain, and Lambert, Philippe, *A Constitutive Model For The Dynamic and High-Pressure Behaviour of a Propellant-Like Material: Part I: Experimental Background and General Structure of The Model*. International Journal For Numerical and Analytical Methods In Geomechanics, 2001. **25**(6): p. 551-579.
45. Trumel, H., Fanget, A., and Deragon, A., *A Finite Strain Elastic-Plastic Model For The Quasi-Static Behaviour of Particulate Composites*. International Journal of Engineering Sciences, 1996. **34**(6): p. 677-698.
46. Verma, Devendra, Prakash, Chandra, and Tomar, Vikas, *Interface Mechanics and Its Correlation With Plasticity In Polycrystalline Metals, Polymer Composites, and Natural Materials*. Procedia Engineering, 2017. **173**: p. 1266-1274.
47. Verma, D., Singh, J., Varma, A. H., and Tomar, V., *Evaluation of Incoherent Interface Strength of Solid-State-Bonded Ti64/Stainless Steel Under Dynamic Impact Loading*. The Journal of The Minerals, Metals & Materials Society (TMS), 2015. **67**(8): p. 1694-1703.
48. Verma, Devendra, Exner, Matthias, and Tomar, Vikas, *An Investigation Into Strain Rate Dependent Constitutive Properties of a Sandwiched Epoxy Interface*. Materials & Design, 2016. **112**: p. 345-356.
49. Wu, Xiaoming, Yu, Jianyuan, Ren, Tianling, and Liu, Litian, *Micro-Raman Spectroscopy Measurement of Stress In Silicon*. Microelectronics Journal, 2007. **38**(1): p. 87-90.

50. Prasad, CH Devi Vara, Arunachalam, V., and Ranganathan, V., *Effect of The Formulation of Ingredients and The Process Parameters on The Fracture Toughness of HTPB Based Composite Solid Propellant*. Journal of Energy and Chemical Engineering, 2014. **2**(3): p. 94-105.
51. Barenblatt, G.I., *The Formation of Equilibrium Crack During Brittle Fracture. General Ideas and Hypothesis. Axially Symmetric Cracks*. Applied Mathematics and Mechanics (PMM), 1959. **23**(3): p. 622-636.
52. Dugadale, D.S., *Yielding of Steel Sheets Containing Slits*. Journal of Mechanics and Physics Of Solids, 1960. **8**(2): p. 100-104.
53. Tomar, Vikas, Zhai, Jun, and Zhou, Min, *Bounds for Element Size in a Variable Stiffness Cohesive Finite Element Model*. International Journal for Numerical Methods in Engineering, 2004. **61**(11): p. 1894-1920.
54. Mcglaun, J. M. and Yarrington, P., *Large Deformation Wave Codes*, In High-Pressure Shock Compression Of Solids. High-Pressure Shock Compression Of Condensed Matter, J. R. Asay and M. Shahinpoor, Editors., Springer: New York, NY, 1993.
55. Barua, A., Horie, Y., and Zhou, M., *Microstructural Level Response of HMX-Estane Polymer-Bonded Explosive Under Effects of Transient Stress Waves*. Proceedings Of The Royal Society A: Mathematical, Physical and Engineering Sciences, 2012. **468**(2147): p. 3725-3744.
56. Tomar, Vikas, *Insights Into The Effects of Tensile and Compressive Loadings on Microstructure Dependent Fracture of Trabecular Bone*. Engineering Fracture Mechanics, 2009. **76**(7): P. 884-897.
57. Baek, Hyunil and Park, Kyoungsoo, *Cohesive Frictional-Contact Model For Dynamic Fracture Simulations Under Compression*. International Journal of Solids and Structures, 2018. **144-145**(1): p. 86-99.
58. Weber, G. G., Lush, A. M., Zavaliangos, A., and Anand, L., *An Objective Time-Integration Procedure For Isotropic Rate-Independent and Rate-Dependent Elastic-Plastic Constitutive Equations*. International Journal of Plasticity, 1990. **6**(6): p. 701-744.
59. Gurtin, Morton E. and Anand, Lallit, *The Decomposition $F=F^e F^p$, Material Symmetry, and Plastic Irrotationality For Solids That are Isotropic-Viscoplastic or Amorphous*. International Journal of Plasticity, 2005. **21**(9): p. 1686-1719.
60. Henann, David L. and Anand, Lallit, *A Large Deformation Theory For Rate-Dependent Elastic-Plastic Materials With Combined Isotropic and Kinematic Hardening*. International Journal of Plasticity, 2009. **25**(10): p. 1833-1878.
61. Benson, D. J. and Conley, P., *Eulerian Finite-Element Simulations of Experimentally Acquired Hmx Microstructures*. Modelling and Simulation in Materials Science and Engineering, 1999. **7**: p. 333-354.

62. Dafalias, Y. F., *Issues on The Constitutive Formulation at Large Elastoplastic Deformations, Part 1: Kinematics*. Acta Mechanica, 1987. **69**(1-4): p. 119-138.
63. Thiruppukuzhi, Srikanth V. and Sun, C. T., *Models For The Strain-Rate-Dependent Behavior Of Polymer Composites*. Composites Science and Technology, 2001. **61**(1): p. 1-12.
64. Boyce, Mary C., Weber, G. G., and Parks, D. M., *On The Kinematics of Finite Strain Plasticity*. Journal of Mechanics and Physics of Solids, 1989. **37**(5): p. 647-665.
65. Hambir, Selezion A., Franken, Jens, Hare, David E., Chronister, Eric L., Baer, Bruce J., and Dlott, Dana D., *Ultrahigh Time-Resolution Vibrational Spectroscopy of Shocked Molecular Solids*. Journal of Applied Physics, 1997. **81**(5): p. 2157-2166.

CHAPTER 3.
THE EFFECT OF INTERFACE SHOCK VISCOSITY ON THE STRAIN
RATE INDUCED TEMPERATURE RISE IN AN ENERGETIC
MATERIAL ANALYZED USING THE COHESIVE FINITE ELEMENT
METHOD

Chandra Prakash¹, I. Emre Gunduz², Vikas Tomar^{1*}

¹ School of Aeronautics and Astronautics, Purdue University-IN, 47907, USA

² School of Mechanical Engineering, Purdue University-IN, 47907, USA

*Corresponding author, Phone: (765)-494-3006 Fax: (765) 494-0307 Email: tomar@purdue.edu

Manuscript under Preparation.

ABSTRACT

In this work, shock induced failure and local temperature rise behavior of a hydroxyl-terminated polybutadiene (HTPB) - Ammonium Perchlorate (AP) energetic material is modeled using the cohesive finite element method (CFEM). Thermomechanical properties used in the model were obtained from four different experiments: (1) dynamic impact experimental measurements for fitting a viscoplastic constitutive model, (2) in-situ mechanical Raman spectroscopy (MRS) measurements of the separation properties for fitting a cohesive zone model, (3) pulse laser induced particle impact experiments combined with the MRS for measurement of the interface shock viscosity, and (4) Raman thermometry experiments for measurement of HTPB, AP, and HTPB-AP interface thermal conductivity. The increase in the interface shock viscosity lead to a decrease in both the viscoplastic and frictional dissipation. This resulted in a decrease in the maximum temperature and the density of local regions with maximum temperature rise within the HTPB-AP microstructure. HTPB-AP interface regions with a high density of particles were found to be more susceptible to local temperature rise due to the presence of viscoplastic dissipation as well as frictional heating. A power law relation for the decrease in viscoplastic energy dissipation, temperature rise, and the density of the local temperature rise with the interface shock viscosity was obtained.

KEYWORDS: Energetic Material, CFEM, Interface, Shock Viscosity

3.1 Introduction

Energetic materials are composites which consist of an oxidizer material embedded in a polymer binder. A mixture of Hydroxyl terminated polybutadiene (HTPB) and Ammonium Perchlorate (AP) is one example that is mostly used in solid rocket propellant [1]. These materials are susceptible to failure due to external impact or temperature change and thus, initiation and subsequent detonation can occur at unintended times. Energetic materials are known to initiate at regions of sufficient size and temperature that could cause detonation [2]. One key factor that may result in this type of mechanical and thermal behavior of is the heterogeneous nature of energetic material microstructure. In order to determine causes and possible prevention mechanisms, a proper understanding of the underlying mechanisms involved in hot-spot formation under high strain rate impact is necessary.

Several researchers have attempted to identify the critical size, temperature, and time span of hot spots necessary to cause initiation of detonation, which in many cases are found to occur due to cracks, voids or other mechanisms, [1, 3]. There have been attempts to identify different mechanisms for hot spot formation in microstructure, such as, the adiabatic compression of trapped gases, heating at crack tips, viscous heating of material between impacting surfaces, friction between sliding or impacting surfaces, and friction during mechanical failure [1]. Temperature increase due to frictional energy dissipation within the microstructure at contact between failed surfaces is an important consideration. A few of the several reasons of microstructural failure in energetic materials have been found to be; particle failure, particle-binder debonding, and cavitation and pore collapse [4]. However any combination of the three can be found to occur simultaneously. Among the above listed failure mechanisms, the most dominant failure has been found to be the particle-binder interface debonding [5] for hot spot formation as cracks have been

found to propagate mostly along such interfaces [6]. Subsequent studies have shown that the fracture resistance of these materials is highly dependent on the strength of the interfaces [7]. This strength, in turn, has been found to be dependent on the material constituents and their relative sizing. Drodge et al. [8], studied the effect of particle size on the mechanical behavior of energetic materials, which showed a decrease in yield strain caused by an increase in particle size. Experimental observations, by Rae et al. [6], also showed that the failures starts around larger particles with cracks preferentially propagating along interfaces.

A physical property that has been critical in predicting the influence of mechanical loading on the temperature rise in the energetic material microstructures is the shock viscosity [2]. Benson et al. [2] have shown that the temperature increase due to impact is higher in the inviscid case than when the shock viscosity is taken into account. The shock viscosity is responsible for the energy dissipation that accompanies the local rate of shear deformation and affects the temperature increase in the material undergoing shock loading. Many researchers have used experimental techniques such as VISAR, [9-12], for the shock wave rise time measurements in order to determine shock viscosity. Kanel et al. [10], have observed that the shock viscosity is significantly affected by applied strain rate. Several researchers [10, 13, 14] have shown the dependence of the exponent in the power law relation between strain rate and shock stress on material properties, such as density, viscosity etc., as well as microstructural parameters such as porosity, particle size [13], the material heterogeneity [15] and the interface impedance mismatch [16]. Recently Prakash et al., [17], have used a novel experimental approach based on particle impact and MRS to measure the interface shock viscosity for an HTPB-AP material interface and showed that the value of interface shock viscosity changes with the interface chemical composition.

In this work, the mechanical response of an HTPB-AP energetic material microstructure under shock loading for different interface chemical compositions of HTPB-AP interfaces is modeled using the cohesive finite element method (CFEM). The chemical composition of the HTPB-AP interface is altered by adding binding agents which has been shown to change the mechanical properties, such as stiffness, failure strength [18] , as well as the interface viscosity [17]. CFEM is based on the cohesive zone approach which uses a micro-scale level local failure behavior based damage model. This technique can be implemented to model fracture in individual components as well as the interface separation behavior of the microstructure. Cohesive zone models (CZMs) have been used by many researchers [19-22] to simulate the interface debonding. Barua et al. [19, 20, 23, 24] have studied the microstructural level response of various idealized PBXs under shock induced impact loading using CZM. However the numerical models used in the literature, [25-28], do not include shock viscosity, especially the interface shock viscosity, as well as the strain rate dependent interface constitutive model.

For the purposes of this work, cohesive parameters are obtained experimentally through in-situ mechanical Raman spectroscopy (MRS) measurements [18, 29, 30]. As high strain rates are used, the material is modeled using viscoplastic constitutive behavior, [17, 18, 30]. The remaining part of the paper is arranged as follows: Section 2 briefly describes the sample preparation and experimental procedures for measuring the material mechanical properties based on work in [18]. Section 3 describes the CFEM method used to simulate the impact behavior of the HTPB-AP samples. Section 4 presents the results obtained from experimental measurement of thermal conductivity along with the numerical simulation of the impact of EM composites. Section 5 presents summary and conclusions.

3.2 Experimental Methods

In this section, the experimental methods that were used to obtain mechanical properties are explained in brief. These methods have been explained in detail in earlier publications [18, 30, 31]. In order to create samples, AP particles were embedded manually into a HTPB binder. The HTPB binder was created by mixing R-45M liquid Polybutadiene and Isophorone Diisocyanate (IPDI) at an index ratio of 1.05. The mixture was then poured into a Teflon-plated mold. The AP particles were embedded with a structured and predetermined amount of spacing, and the samples were cured in a 60°C oven for 7 days. When fully cured, the sample is carefully cut down to an appropriate diameter and thickness. In order to study the effect of chemical composition, two types of samples were created: Sample 1 consisted of HTPB and AP without binding agent and Sample 2 consisted of HTPB, AP and a binding agent Tepanol.

Table 7 Constitutive model parameters for bulk and interface [18]

Parameter		χ (MPa) ⁻ⁿ	m	n
HTPB		0.54	-0.18	1.8
AP		3.7E10	-9.8	5.9
Interface	Sample-1	1.0E5	-5.0	2.5
	Sample-2	1.0E4	-4.2	2.0

3.2.1 Constitutive Model for HTPB, AP and Interface

The constitutive material model and the cohesive zone model parameters were obtained using a nanoscale dynamic impact experiment and in-situ mechanical Raman spectroscopy (MRS) experiment, respectively. A strain-rate dependent stress-strain law was obtained using a nanoscale dynamic impact experiment [18]. The stress-strain data obtained from the impact tests was fit to a

viscoplastic power law model to define the constitutive behavior of the material [31]. The viscoplastic model parameters for HTPB, AP and interface are shown in Table 7 [18].

3.2.2 Cohesive Zone Model Parameters for HTPB-AP Interface

In this work, in-situ mechanical Raman Spectroscopy tests, as proposed by Prakash et al. [18], were performed in order to obtain the cohesive zone parameters. Cohesive zone parameters for bulk HTPB, AP and different interfaces are given in Table 8 [18].

Table 8 Cohesive zone model parameters for bulk and interface [18]

Material/Interface		Cohesive Strength (MPa)	Critical Displacement (mm)	Cohesive Energy (N/mm)
HTPB		0.8	0.5	0.2
AP		2×10^3	5×10^{-3}	5.0
Interface	Sample 1	1.1	0.12	0.065
	Sample 2	2.91	0.11	0.16

3.2.3 Shock Viscosity for HTPB-AP Interface

Interface shock viscosity was obtained using a combined pulse laser induce impact experiment and MRS [17]. Table 9 lists the value of shock viscosity for HTPB, AP and the HTPB-AP interface used in this work.

Table 9 Shock viscosity of the HTPB, AP and HTPB-AP interface (Sample 1 is without Binding Agent and Sample 2 is with Binding Agent: Tepanol)

	HTPB [32]	AP [2]	Sample 1	Sample 2
Viscosity (Pa.s)	1.5	30	4.8	6

3.2.4 Thermal Conductivity for HTPB-AP Interface

In order to model the thermal behavior of the HTPB-AP energetic material, thermal conductivity values of the individual constituents are needed. For the HTPB and AP phases, thermal conductivity values are readily available in literature [33, 34]. However, there are no available thermal conductivity values for the HTPB-AP interface. In this work, an in-situ MRS method is used to experimentally measure the thermal conductivity at HTPB-AP interface. The experimental method has been explained elsewhere [35-40]. Here a brief summary is presented.

Perichon et al. [41] were among the first researchers who developed and explored the relation between Raman peak position and temperature change in order to measure temperature distribution and thermal conductivity measurements using Raman spectroscopy. Since then several researchers have shown this method to be an effective and accurate tool in the temperature distribution measurement as well as the thermal conductivity measurement [35, 37]. In order to measure the temperature distribution around an interface, first a correlation between the changes in Raman shift due to known externally applied temperature needs to be obtained. The experimental setup to obtain the calibration relation between Raman shift and the temperature change is shown in Fig. 39(a). The sample is mounted on a hot-stage where a temperature detector is attached to one end of the sample and the other end was heated using electric coils. An Ar+ laser beam (Modu-Laser Inc., UT) of wavelength 514.8 nm was directed at the sample as the sample was being heated. The backscattered laser beam was collected back by an objective and directed to a spectrometer (Acton SP2500; Princeton Instruments Inc., NJ). A low power laser beam (~5

mW) was used to measure the Raman shift so that the temperature change due to the laser beam remains less than 1 K [35]. In this work, a correlation between the Raman shift of the CH₂ asymmetric stretching mode (Fig. 39(b)) and the sample temperature was obtained. The Raman shifts at different temperatures were obtained as plotted in Fig. 39(c). A linear relationship between the Raman shift and the temperature change from the reference value of the sample was fitted to a linear relation, which is given by,

$$\Delta w = C\Delta T \quad (50)$$

where the value of C is obtained from the slope of the linear correlation curve in Fig. 39(c), which is equal to 0.121 cm⁻¹/K. This calibration constant is then used to calculate the temperature change of the samples by measuring the change in Raman shift values.

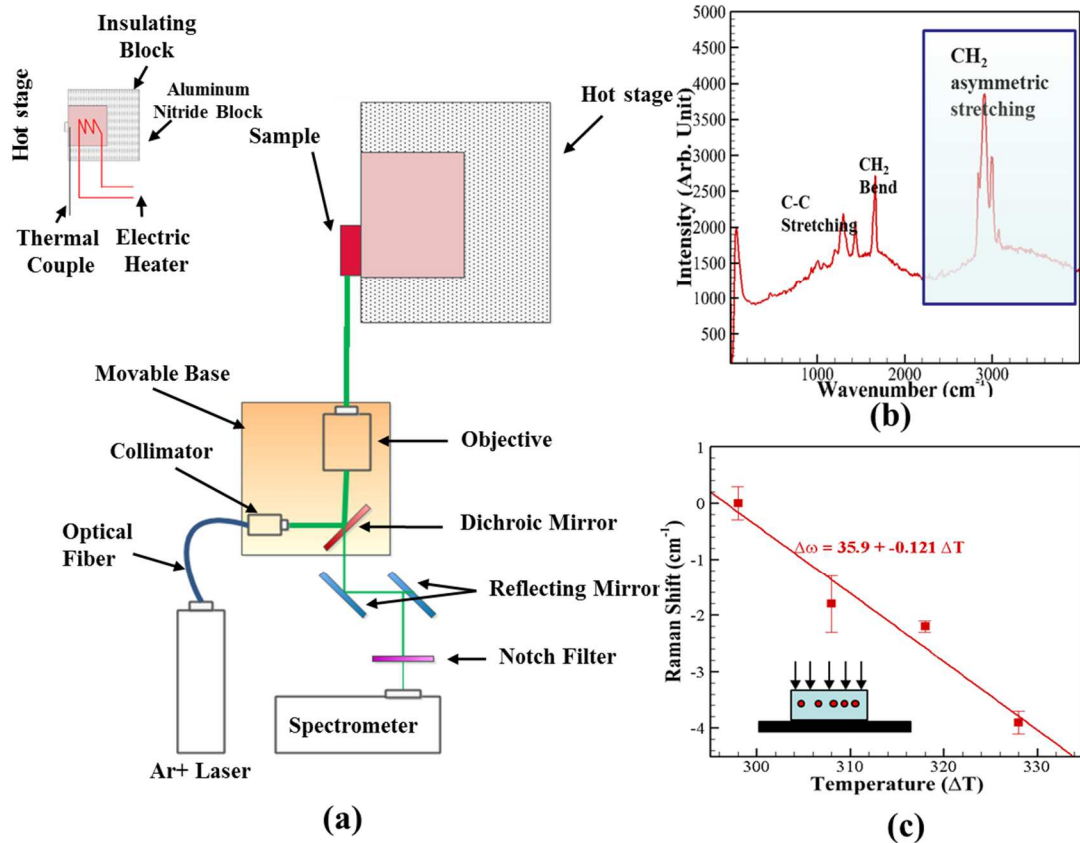


Figure 39 (a) Experimental set-up for Raman shift versus temperature change calibration, (b) a representative Raman spectra of HTPB and (c) calibration curve for Raman shift versus Temperature change.

3.3 Cohesive Finite Element Method Framework

CFEM has been used extensively for simulating the impact induced damage behavior of different composite materials [42, 43], including energetic materials [19-21, 44]. CFEM application to a material with unknown crack path can be approached in two ways; the first is to dynamically insert cohesive surfaces into the model as fracture develops and the second is to define all bulk element boundaries as cohesive surfaces. For the purposes of this work, the second approach is employed [17, 18, 45]. The finite element mesh for the modelled microstructure was generated with ‘cross triangle’ elements and cohesive surfaces at all element boundaries, as shown in Fig. 40. The rectangular mesh size for all of the models, which contains four ‘cross triangle’

elements each, was $1\ \mu\text{m}$, creating 250,000 elements in the domain. The mesh size was chosen based on the criterion outlined by Tomar et al. [46]. The interface was modeled as a $0.5\ \mu\text{m}$ thick bulk element.

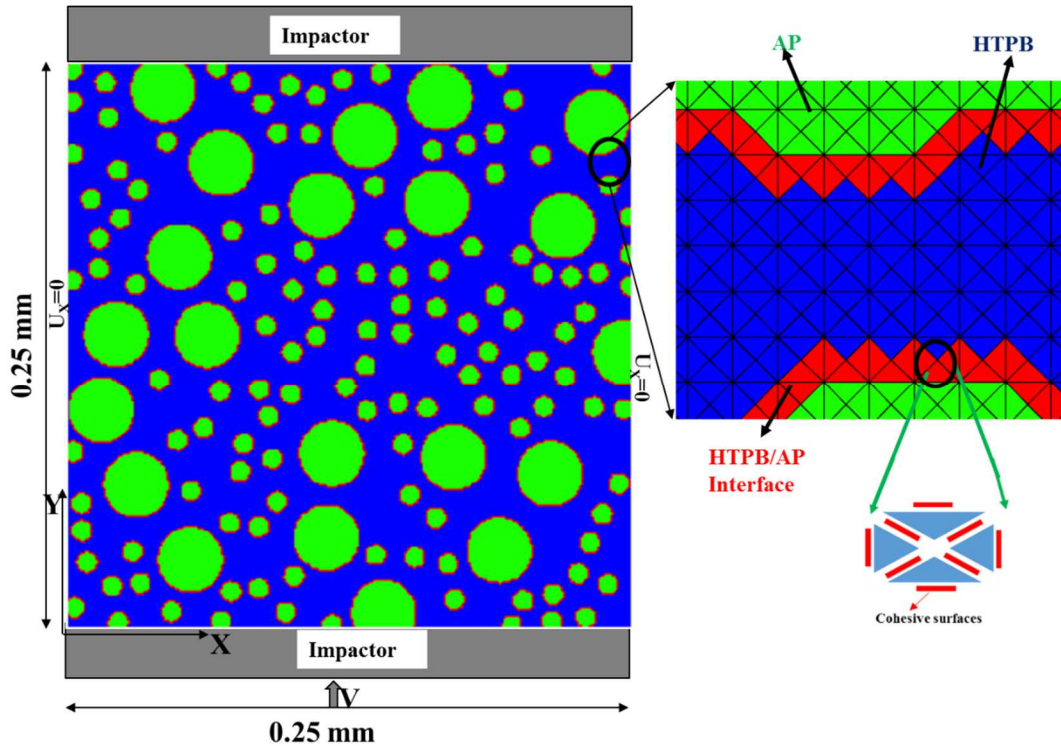


Figure 40 The finite element model of HTPB-AP microstructure (50% AP density) showing boundary conditions, and the mesh details as well as cohesive surfaces.

For the continuum elements, a viscoplastic constitutive model is used to govern the stress-strain relations while the irreversible bilinear cohesive law for tensile separation is used to govern the separation at the cohesive surfaces. The large deformation viscoplastic model has been described in an earlier work by the authors [17]. The pressure is calculated by a polynomial form of the Mie-Gruneisen equation of state for which the parameters are given in Table 10 for HTPB and AP [47]. The parameters in Table 10 are defined as follows: K is the Bulk Modulus, γ is the

Gruneisen parameter, A , and B are parameters obtained by fitting a Hugoniot curve, ρ_0 is the initial density, E is the Young's modulus and ν is the Poisson ratio.

Table 10 Mie-Gruneisen parameters for bulk HTPB and AP [47].

	K (10^5 MPa)	A (10^5 MPa)	B (10^5 MPa)	γ	ρ_0 g/cm ³	E (MPa)	ν
HTPB	0.02	0.294	0.0196	0.7	0.9	2.5	0.45
AP	0.15	0.225	0.1863	1.0	1.95	20000	0.23

In order to prevent the interpenetration of bulk elements, an acceleration correction term is used that is obtained based on a frictional cohesive contact model developed by Baek et al. [48] for large deformation impact simulation. As was shown in a previous work by the authors [17], the element penetration in this model is insignificant for the total time of the simulation.

In order to identify the local temperature rise within the microstructure, a threshold temperature increase from the reference temperature was chosen. Temperature increase, $\Delta T = T - T_{ref}$, was calculated from [2],

$$T = \frac{e + e_f - e_c}{\rho c_p} \quad (51)$$

where $T_{ref} = 298$ K, e is the internal energy density of the system, e_f is the frictional dissipation energy density, e_c is the cold compression energy density, ρ is the material density and c_p is the heat capacity at constant pressure. The cold compression energy density, e_c is given as [2],

$$e_c = \int_1^\phi \frac{p}{\phi^2} d\phi - \rho c_p T_{ref} e^{[a(1-1/\phi)]\phi^{1-a}} \quad (52)$$

$$\phi = \rho / \rho_0 = 1 / J = 1 / \det(\mathbf{F})$$

where F is the deformation gradient, p is the pressure and a is the first order volume correction factor for γ . In this work, the value of a is taken to be equal to zero for all of the materials [2]. The rate of heat generation (h) by the frictional forces at the bulk element interfaces were obtained from [42],

$$h = T \cdot \llbracket v \rrbracket \quad (53)$$

where T is the contact traction acting at the interface and $\llbracket v \rrbracket$ is the jump in velocity of the surfaces in contact. This frictional heat (h) is then distributed among the contacting bulk elements (element 1 and element 2) based on ratio of heat supply given by Camacho and Ortiz [42] as,

$$\begin{aligned} \frac{\dot{e}_f^1}{\dot{e}_f^2} &= \frac{\sqrt{\kappa_1 \rho_1 c_1}}{\sqrt{\kappa_2 \rho_2 c_2}} \\ h &= \dot{e}_f^1 + \dot{e}_f^2 \end{aligned} \quad (54)$$

where κ is the thermal conductivity and c is the specific heat at constant pressure of the bulk element involving the interface. The simulations were done for a very small period of time ($\sim 0.1 \mu\text{s}$) in order to avoid the element distortion.

3.4 Results and Analysis

3.4.1 Experimental Measurement of Thermal Conductivity

By measuring the laser energy absorbed by the sample and corresponding temperature increase of the laser spot on the sample, the thermal conductivity of the sample can be derived with a heat transfer model. It has been shown that the isothermal conditions can be assumed and the interface between sample and the substrate can be assumed to be hemispheric, if the thickness of the sample is more than one magnitude larger than the laser spot size [19]. In this work, a 1.2 mm thick HTPB-AP sample was loaded under tensile load. Since the thickness of the sample is much larger (1.2 mm) than the laser spot size ($\sim 1 \mu\text{m}$), a linear relation between thermal

conductivity and laser power is used as suggested by Nonnenmacher et al. [49]. A Horiba Xplora Plus Raman spectroscope was used to measure the Raman shift during loading. A 532 nm wavelength laser with a laser power of 20 mW was used and the laser spot size (d) was found to be of approximately 1 μm . By measuring the laser power (P) and corresponding temperature change (ΔT) thermal conductivity of the sample can also be calculated using [35],

$$\kappa = \frac{2P}{\pi d \Delta T} \quad (55)$$

Here, ΔT is the change in temperature of individual scan points, shown in Fig. 41(b), from the initial bulk temperature [41]. Then, Eq. (55) directly relates the thermal conductivity to the change in temperature of each individual scan points. In this work, since the laser diameter is $\sim 1 \mu\text{m}$, it is assumed that the heat generated by the laser source is responsible for the increase in the local temperature only, which when used in Eq. (55) results in the local thermal conductivity.

Using Eq. (53) for the temperature change in Eq. (54), the thermal conductivity can be written as,

$$\kappa = \frac{2PC}{\pi d \Delta \omega} \quad (56)$$

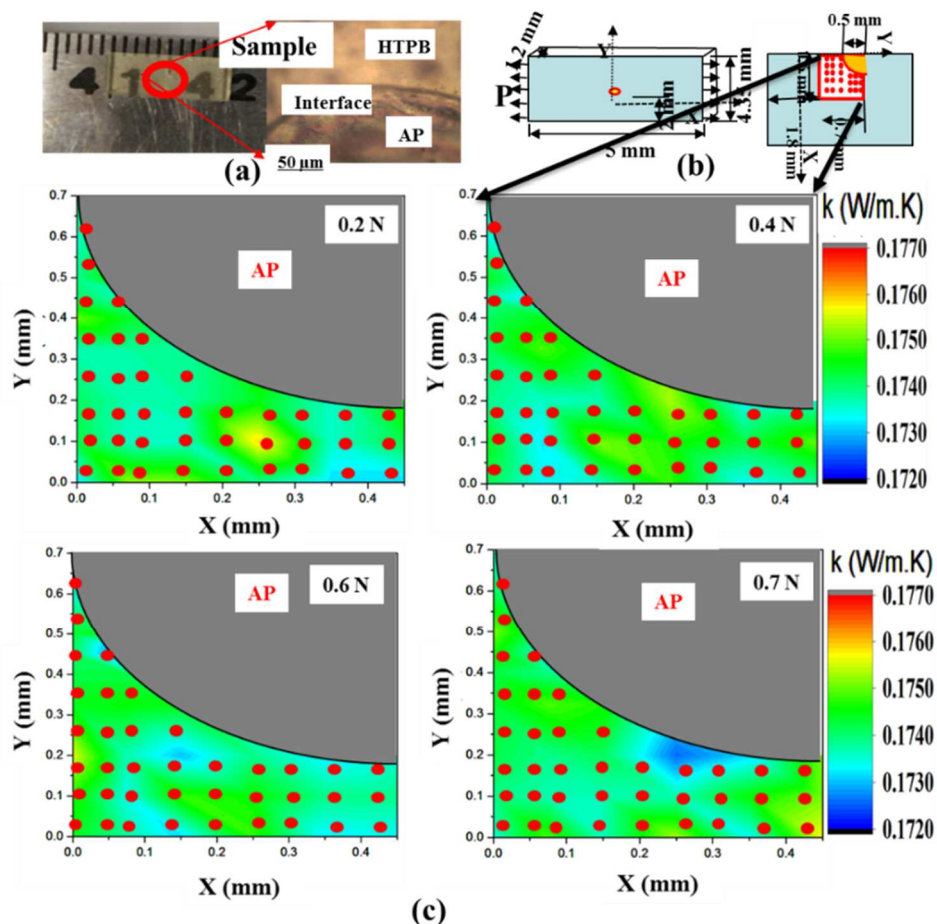


Figure 41 (a) HTPB-AP tensile sample, (b) sample dimensions, boundary conditions and the scan area and (c) thermal conductivity near the HTPB-AP-Tepanol interface. Red dots are the position where Raman spectra were recorded.

In this work, a tensile load is applied to a single particle HTPB-AP sample as shown in Fig. 41(a) and the change in Raman shift near the HTPB-AP interface in the scan area (see Fig. 41(b)) was obtained. Thereafter, Eq. (55) was used to calculate thermal conductivity of the scan area near the HTPB-AP interface. As can be seen from Fig. 41(c) for different tensile load, a slight decrease in the thermal conductivity is observed and an average value of 0.175 W/m.K was taken to be the interface thermal conductivity for HTPB-AP-Tepanol interface. Similarly, the value of thermal conductivity for HTPB-AP interface, without binding agent, was found to be equal to 0.16 W/m.K.

3.4.2 Numerical Simulation of Shock Behavior of HTPB-AP Energetic Material

The CFEM simulation model described in [17, 18], is used in predicting the effect of interface shock viscosity on the overall microstructure dependent impact behavior and temperature increase due to impact in multi-particle HTPB-AP sample (see Fig. 40). Strain rate dependent power law viscoplastic stress-strain model, as given in Table 7, was used for HTPB, AP and the HTPB-AP interface [18]. The cohesive zone model parameters, as given in Table 8, obtained experimentally through mechanical Raman spectroscopy, were used for modeling cohesive separation behavior [31]. The interface shock viscosity is shown in Table 9 [17]. Thermal conductivity and heat capacity of the HTPB, AP and the HTPB-AP interface used in the simulation are given in Table 11. The value of heat capacity for the HTPB-AP interface was obtained as the average value of AP and HTPB phase values as suggested by Hu et al. [49].

Table 11 Thermal properties of HTPB, AP and the HTPB-AP Interface.

	HTPB	AP	HTPB-AP Interface
Thermal Conductivity (W/m.K)	0.28 ^[50]	0.4 ^[50]	0.175 ^[17]
Heat Capacity (kJ/Kg.K)	2.5 ^[34]	1.1 ^[33]	1.8

The impact induced local temperature rise in an idealized HTPB-AP EM microstructure (see Fig. 40), with circular AP particles, were simulated. The circular AP particles had radii varying from 5 μm to 15 μm , [51], with 50% area fraction. In order to understand the effect of individual constituents (HTPB, AP and the HTPB-AP interface) of the microstructure, first the impact behavior of the microstructure was analyzed for a strain rate of 100,000 s^{-1} . The boundary conditions are shown in Fig. 40. Pressure waves passing through the microstructure is analyzed and the corresponding normal compressive and shear stresses are investigated at different time steps.

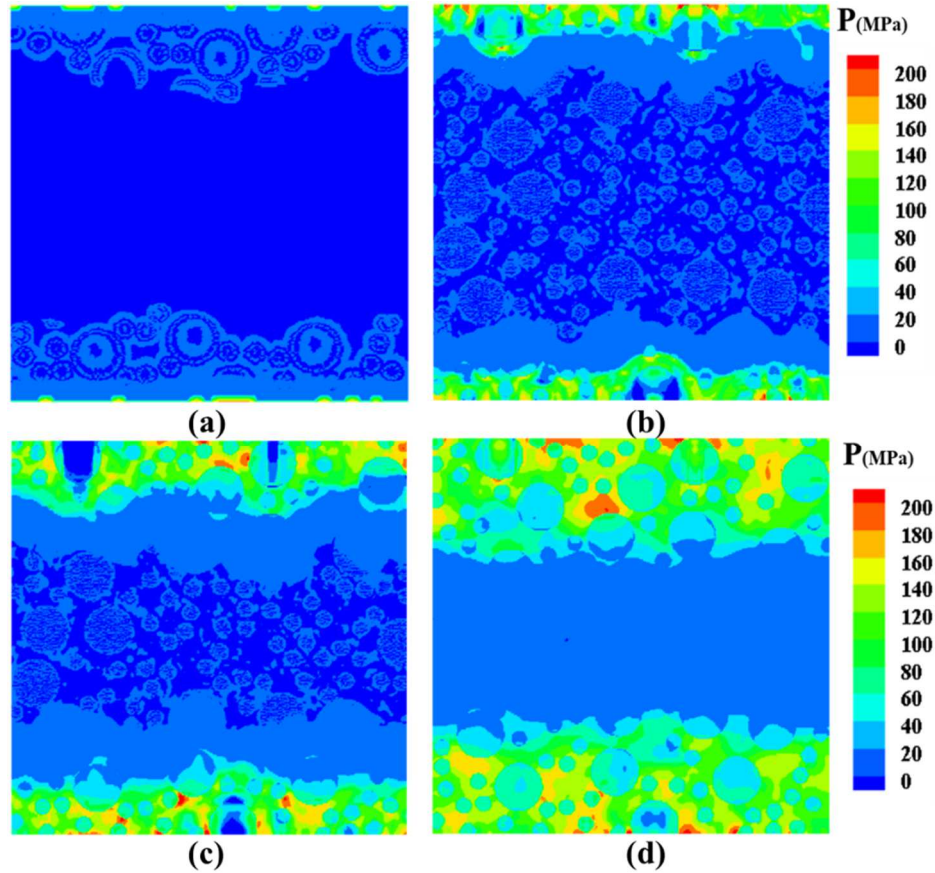


Figure 42 Pressure map in the HTPB-AP microstructure (for loading conditions shown in Fig. 2) at time (a) 0.001 μs , (b) 0.002 μs , (c) 0.004 μs and (d) 0.006 μs .

Figure 42 shows the pressure wave propagating through the microstructure at different time steps. As shown in Fig. 42(b), pressure distribution profile near top and bottom surfaces are different, under equal impact velocity of 250 m/s, due to the difference in the AP particle distribution. As the pressure wave propagates inwards, the interface phase between bulk AP and HTPB phase acts as a barrier and reflects the pressure wave. This creates a lower pressure in larger AP particles as shown in Fig. 42(c). However, the amount of pressure wave reflection, when propagating from bulk AP phase to HTPB-AP phase is lower than the reflection when propagating from HTPB-AP interface phase to bulk HTPB phase, Fig. 42(d). This creates a high stress concentration at the HTPB-AP interface phase which leads to deformation and energy localization.

The pressure waves are transmitted, without significant reflection, through the interface of HTPB and the AP particles when the particle density is high, i.e. when the amount of bulk HTPB phase separating the particles is small. This can be explained by observing the stress profile along a cross-section with varying AP particle distribution.

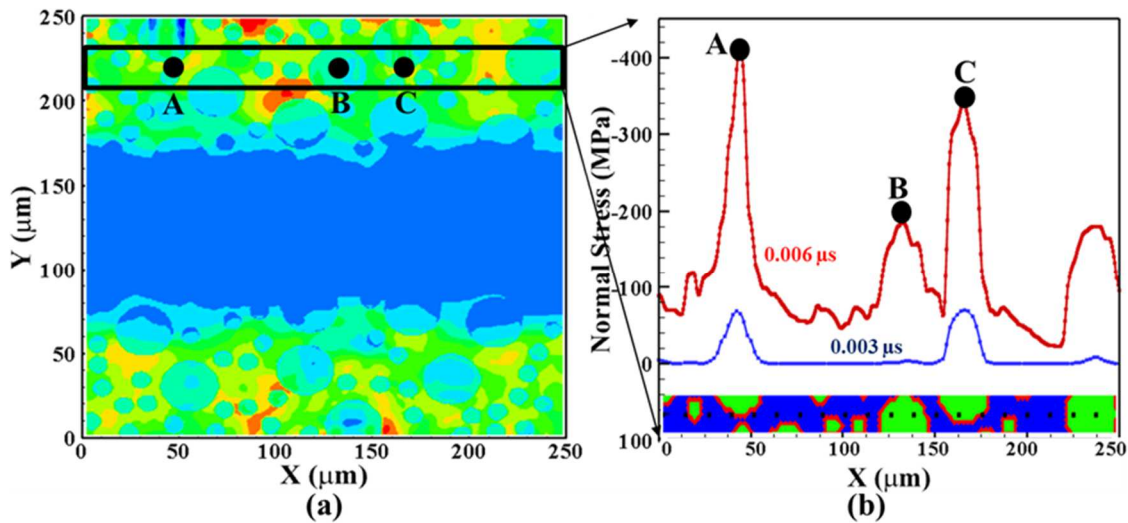


Figure 43 Normal stress profile in the microstructure along a selected cross-section at two different time steps.

The normal compressive stress distribution along a selected cross-section is shown in Fig. 43. The specific section, Fig. 43(a), is chosen because of the continuously varying local particle size and density distribution. The position marked A, corresponds to the position at the HTPB-AP interface phase where two particles are separated only by 2 μm which is covered by HTPB-AP interface phase. The position marked B, corresponds to the position inside an AP particle. The position marked C, corresponds to the position inside an AP particle but close to the HTPB-AP interface. As shown in Fig. 43(b), maximum stress occurs close to the HTPB-AP interfaces around larger AP particles (position A and C). It is observed that initially (at time 0.003 μs) only the interface around large AP particles where particles are closely packed, experiences a higher stress

concentration. This is due to the increase in the interaction between AP particles and the stress concentration at the HTPB-AP interfaces as was also reported earlier by authors [17] for a single particle HTPB-AP sample. As time progresses, the normal stress inside the particle (position B) increases but remains below the value at the HTPB-AP interface (position A or C).

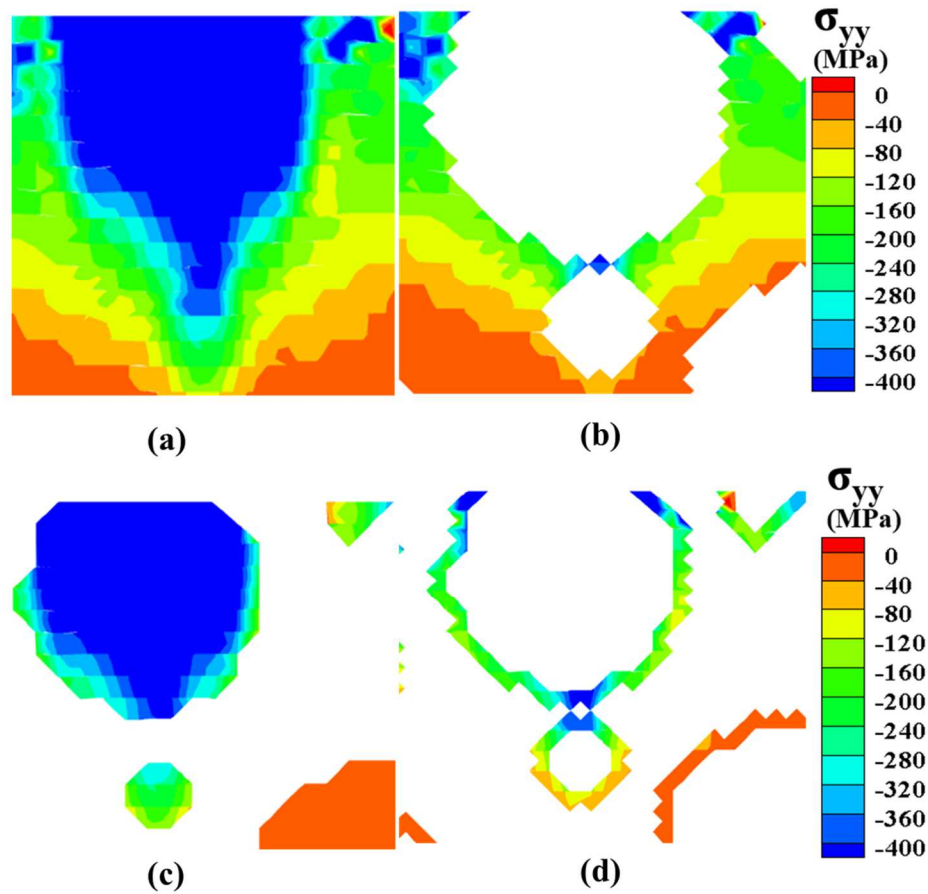


Figure 44 Normal stress distribution in the (a) microstructure at the HTPB-AP interface near position A shown in Fig. 5, (b) HTPB, (c) AP and (d) the HTPB-AP interface at $t = 0.006 \mu s$.

In order to understand the mechanism responsible for the maximum stress at the interface, the normal stress distribution near the HTPB-AP interface is plotted. Figure 44 shows a normal stress distribution, where AP particles are close to each other (near position A shown in Fig. 43), in individual constituents (HTPB, AP and HTPB-AP interface) of the microstructure. It is observed,

that the stress wave reflection is insignificant at interfaces where AP particles are separated only by the HTPB-AP interface phase and the stress wave gets transmitted further. This is because the reflection coefficient (calculated from the equation given by A. Garbacz [52]) of HTPB-AP interface phase with the AP phase is low ($R = 0.24$) as compared to that between HTPB and AP phase ($R = 0.98$) or between HTPB and HTPB-AP interface phase ($R = 0.97$).

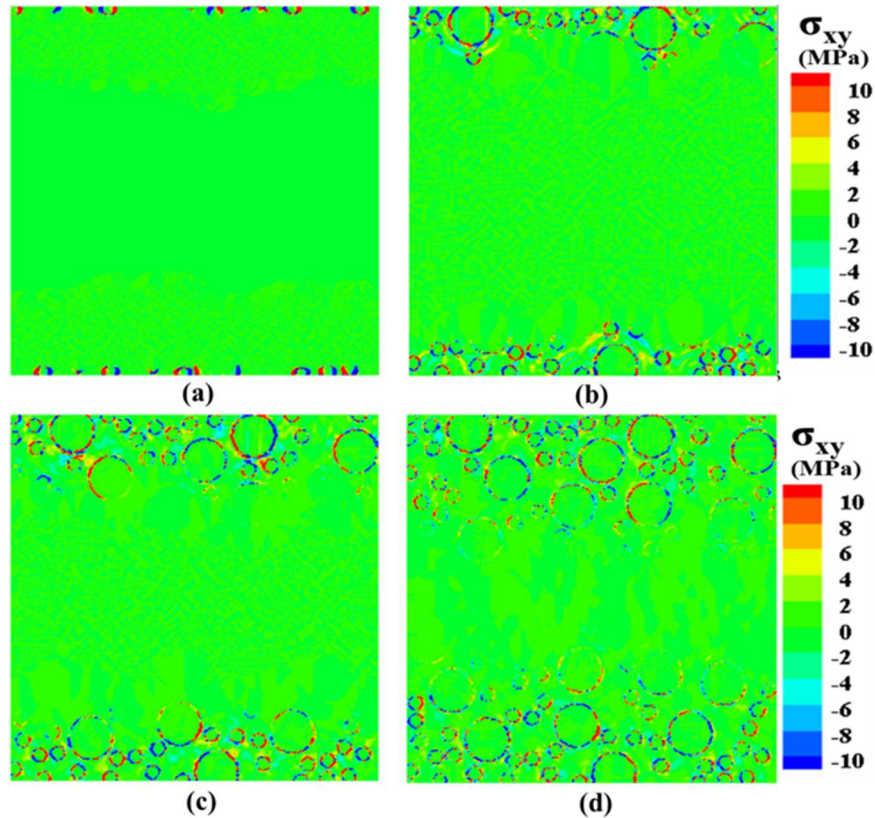


Figure 45 Shear stress distribution in the HTPB-AP microstructure at time (a) 0.001 μs , (b) 0.002 μs , (c) 0.004 μs and (d) 0.006 μs .

Shear stress plays a dominant role in determining the interface failure behavior in the material as well as the temperature rise due to frictional heat dissipation [53]. The shear stress distribution in the HTPB-AP microstructure is shown in Fig. 45. It is observed that the shear stress propagates along the HTPB-AP interface phase only. It can also be seen that the shear stress is

highly localized near the HTPB-AP interface and remains concentrated at these positions. This can be further analyzed by studying the shear stress localization in the interface region.

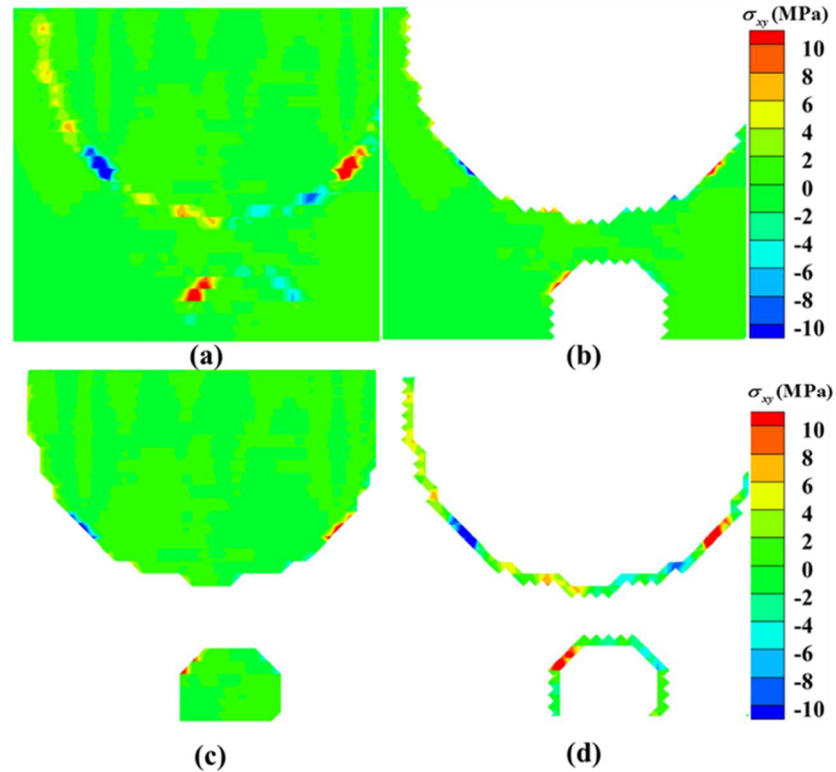


Figure 46 Shear stress distribution in the (a) microstructure at the HTPB-AP interface near position A shown in Fig. 43, (b) HTPB, (c) AP and (d) the HTPB-AP interface at $0.006 \mu\text{s}$.

The shear stresses distribution near a HTPB-AP interface region where particles are in close vicinity is shown in Fig. 46. Shear stress in the bulk HTPB (see Fig. 46(a)) and AP (see Fig. 46(b)) are negligible and are concentrated in the HTPB-AP interface phase only, see Fig. 46(c). This is because the interface boundaries can act as a source, as well as a barrier, to the shear wave [53], depending on where the shear localization starts. In this case, since the localization starts at the interface, as shown in Fig. 45(a), the shear stress remains concentrated along the interface itself and does not propagate further into the bulk, Fig. 45(b-d). This shear localization behavior then

results in an increased viscoplastic and frictional dissipation near the HTPB-AP interface region which leads to a local increase in the temperature.

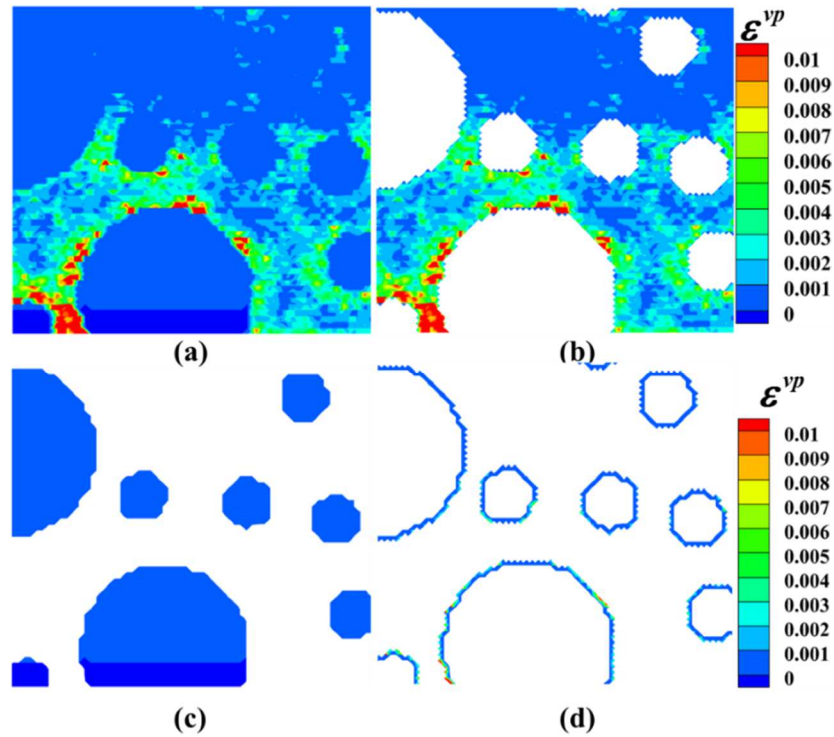


Figure 47 Effective viscoplastic strain distribution in the (a) microstructure at the HTPB-AP interface near position A shown in Fig. 43, (b) HTPB, (c) AP and (d) the HTPB-AP interface at $0.006 \mu\text{s}$.

Internal energy, in Eq. (51), consists of elastic strain energy and viscoplastic dissipation energy. Viscoplastic dissipation is directly proportional to the magnitude of viscoplastic strain and the stress. The distribution of effective viscoplastic strain within the HTPB-AP microstructure is plotted in Fig. 47 as shown at different time steps. It is observed that the effective viscoplastic strain in the HTPB-AP interface phase is higher than the AP particles. Similarly, the value of effective viscoplastic strain is higher in the HTPB near the HTPB-AP interface phase where the particle density is high. This occurs because of the higher stresses observed in the HTPB-AP interface phase, as shown earlier in Fig. 43 and Fig. 45, which leads to an increase in the

viscoplastic deformation. This results in a higher viscoplastic energy dissipation in the HTPB-AP interface phase, which leads to an increased temperature in this phase as shown next.

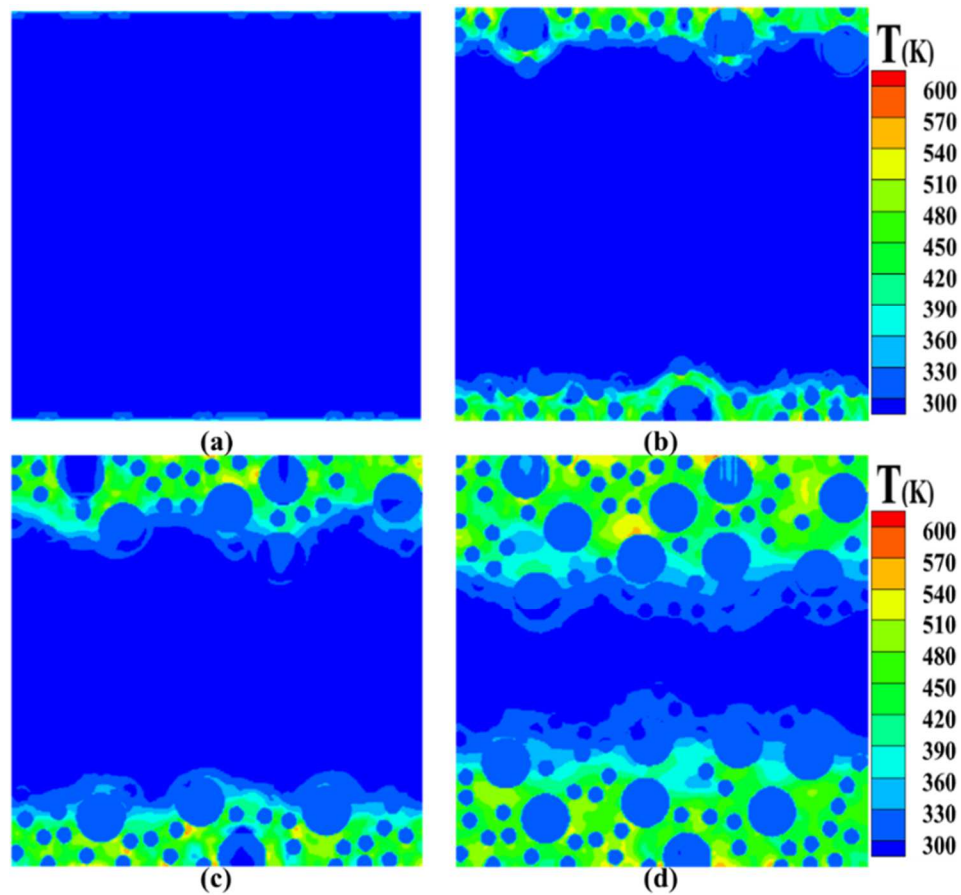


Figure 48 Temperature distribution in the HTPB-AP microstructure at (a) 0.001 μs , (b) 0.002 μs , (c) 0.004 μs and (d) 0.006 μs .

Figure 48 shows the temperature increase in the microstructure. Because of the high stress condition at the top boundary, which is under constant compression, a higher value of temperature is reached much earlier than the bulk. However, as the stress wave propagates further into the microstructure, due to the variation in the AP particle distribution, stress and strain inside the microstructure vary significantly which leads to significant variation in energy dissipation. Increase in temperature within the microstructure occurs due the energy dissipation in the form of

viscoplastic dissipation and the frictional heat dissipation as evident from Eq. (51). It is observed from Fig. 48, that the temperature increase is localized at the HTPB-AP interface phase. The temperature localization is greater at positions within the microstructure where particle density is high. This can be explained based on the stress and viscoplastic strain distribution shown earlier. As shown in Fig. 46 and Fig. 47, the shear stress and the viscoplastic strains are maximum in the HTPB-AP interface phase. This contributes to the higher viscoplastic dissipation at the HTPB-AP interface. Also, the normal stresses show a jump in the value near the position of high density AP particles. This stress concentration at the HTPB-AP interface phase, increases the strain energy density in this phase which results in the increase in temperature.

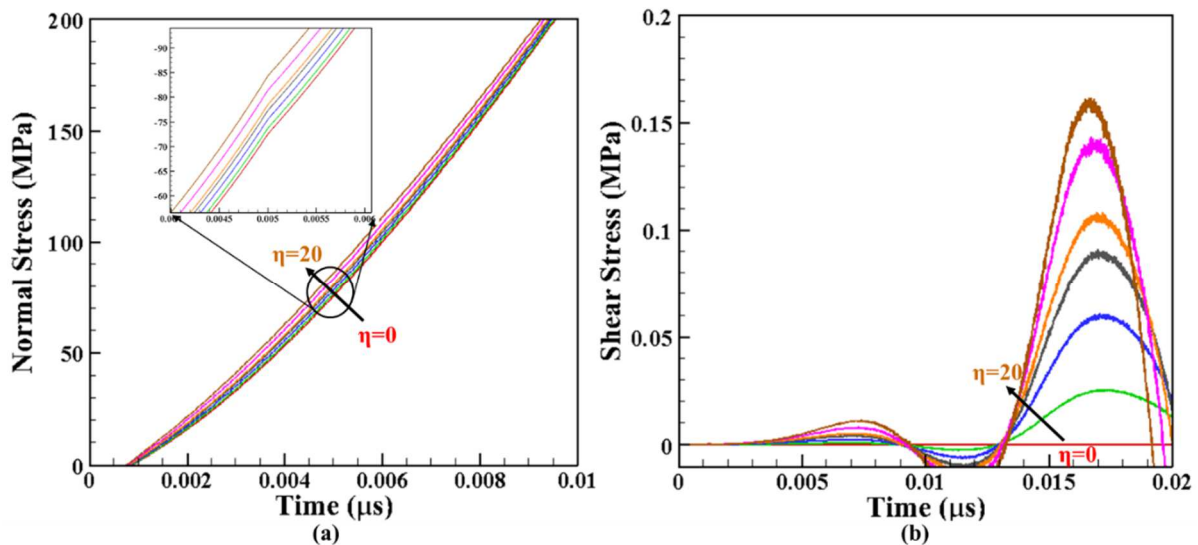


Figure 49 (a) Effective normal compressive stress and (b) effective shear stress history as a function of shock viscosity in the HTPB-AP microstructure.

The effect of interface shock viscosity on the impact behavior and the corresponding local temperature change in the HTPB-AP microstructure is studied next. First the deformation behavior and the effect of interface shock viscosity is studied. Figure 49 shows the values plotted for effective normal stress (see Fig. 49(a)) and effective shear stress (see Fig. 49(b)) history in the

HTPB-AP microstructure. As shown in Fig. 49 both the normal and shear stress increases with an increase in the shock viscosity. This is due to an increase in the shock stress within the microstructure that occurs due to increase in viscous effect within the microstructure, especially at the HTPB-AP interface phase. Shear stress shows a more significant effect of interface shock viscosity. This is because the shear stress, as was shown in Fig. 44, was found to be concentrated only at the HTPB-AP interface whereas all three phases (HTPB, AP and the HTPB-AP interface) show a significant contribution to the effective normal stress. This is illustrated next by plotting the normal and shear stress in all three phases separately, Fig. 50.

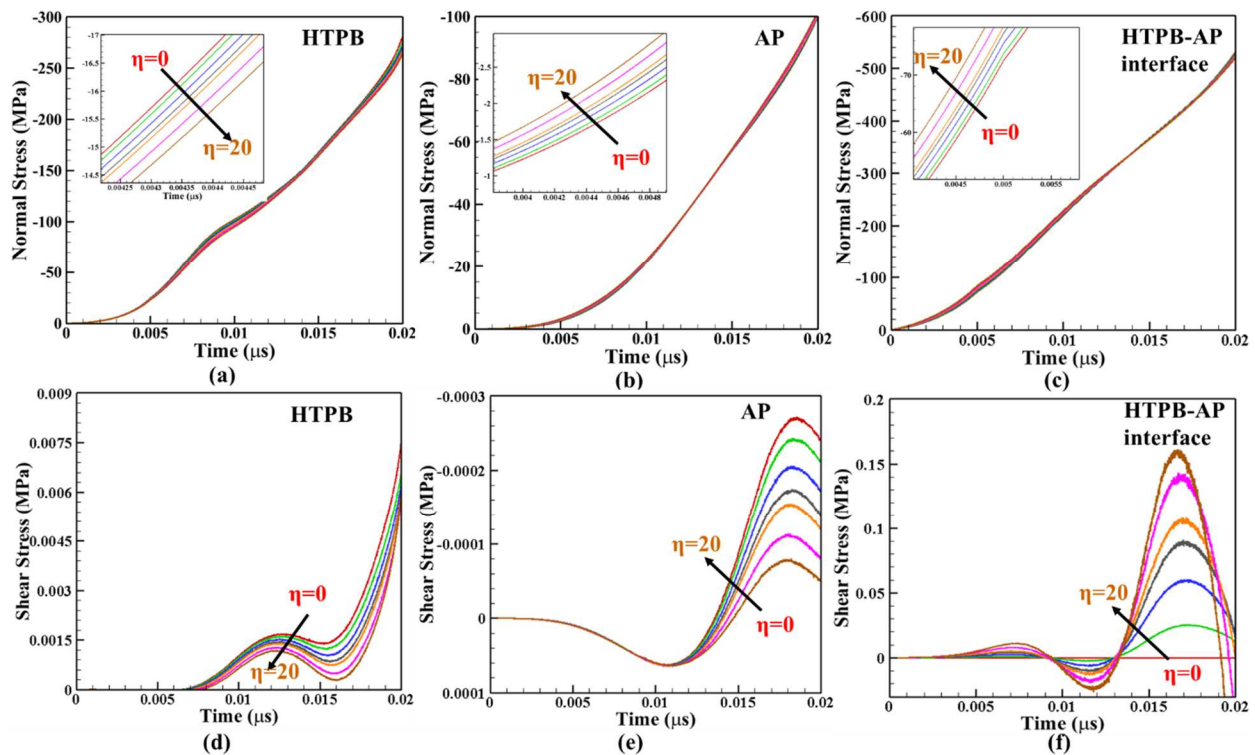


Figure 50 Normal stress (a, b, c) and shear stress (d, e, f) history in HTPB, AP and HTPB-AP interface phase as a function of interface shock viscosity.

Normal stress and shear stress in HTPB, AP and HTPB-AP interface phases are plotted in Fig. 50. Normal stress values are significant in all three phases; however, the HTPB-AP interface phase has the highest concentration as was observed in Fig. 43 as well. Normal stress concentration

in the HTPB-AP interface is twice of that in the HTPB phase. Similarly, shear stress is concentrated in the HTPB-AP interface phase and the other two HTPB and AP bulk phases have very low amount of shear stress present. The shear stress value in the HTPB-AP phase is 20 times greater than that in the HTPB phase. This trend was observed in the entire HTPB-AP microstructure, shown in Fig. 44 and Fig. 45 earlier. The interface shock viscosity affects both normal and shear stress and the most significant effect is observed on the shear stress value in the HTPB-AP interface phase. It can also be seen that the normal and shear stresses increases with the increase in interface shock viscosity in the HTPB-AP interface phase, whereas both stresses decrease in the HTPB phase. This is because, as the interface shock viscosity increases, the stress concentration in the HTPB-AP phase increases which results in a decrease in stress in the HTPB phase. Normal stress in the AP phase increases with increasing interface shock viscosity, but the increase is insignificant (~0.5 MPa increase) as compared to HTPB-AP interface phase (~50 MPa).

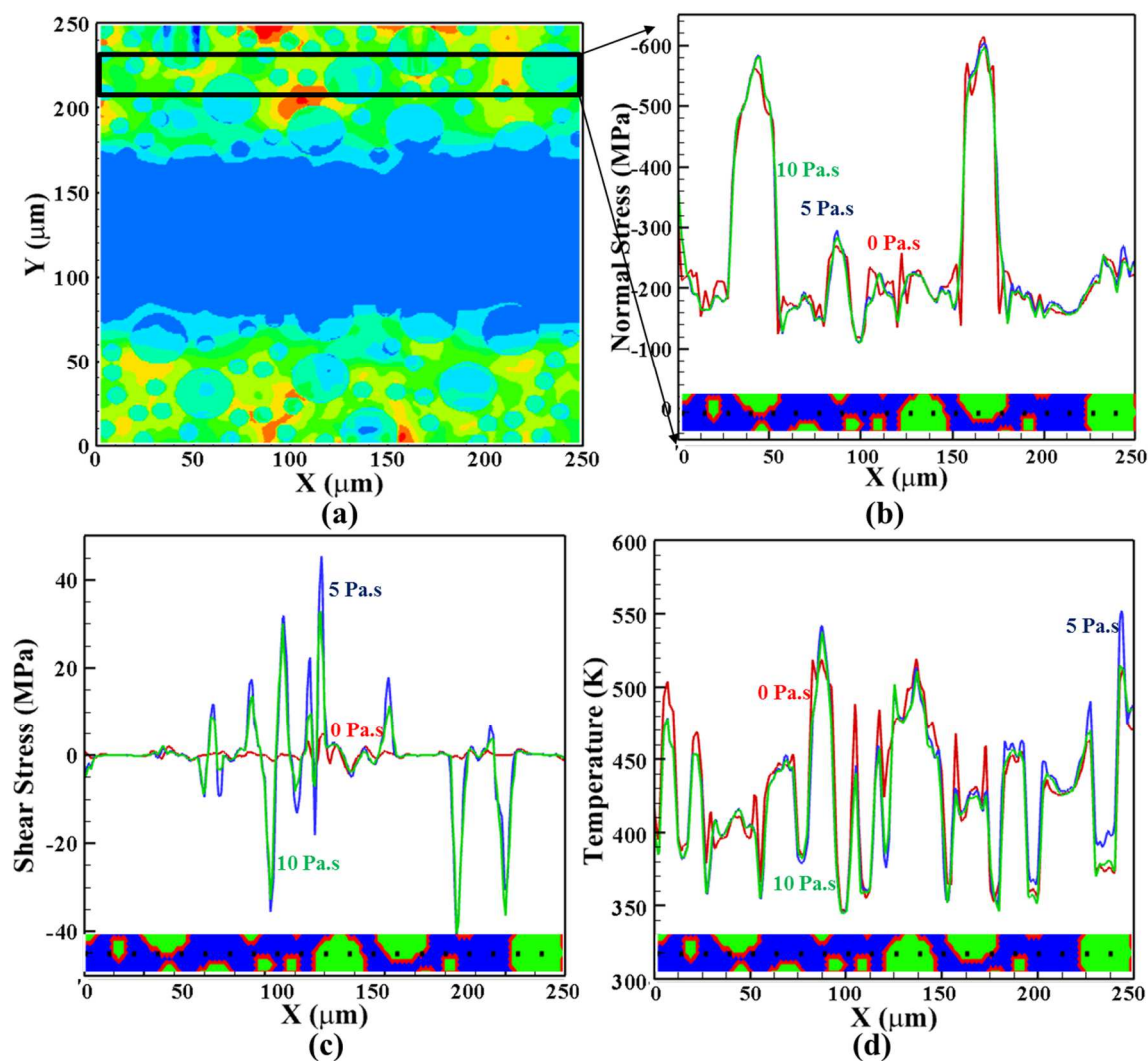


Figure 51 (a) HTPB-AP microstructure, (b) normal stress, (c) shear stress and (d) temperature profile as a function of interface shock viscosity along the selected cross-section at $t = 0.006 \mu\text{s}$.

The effect of interface shock viscosity on the local impact behavior and temperature change in an HTPB-AP microstructure along a horizontal cross-section (same cross-section as Fig. 43(a)), shown again in Fig. 51(a), is discussed next. This cross-section contains different sizes and density of AP particles as well as the HTPB and HTPB-AP interfaces. The distribution of normal stress (see Fig. 51(b)), shear stress (see Fig. 51(c)) and temperature (see Fig. 51(c)) as a function of interface shock viscosity is plotted. The variation in the stress profile of both normal and shear

shows the stress concentration in the HTPB-AP interface phase. The magnitude of the stress concentration however changes with the interface shock viscosity. The temperature profile, see Fig. 51(d), shows that the temperature jumps to a higher value in the HTPB-AP interface phase and drops again inside the HTPB and AP phase. Also, as the interface shock viscosity increases, the temperature decreases significantly at the HTPB-AP interface positions where particle density is low. However, near the HTPB-AP interface phase, where the particle interaction is high, the effect of interface shock viscosity is low. Also, as can be observed from Fig. 51(d), the temperature shows a decrease in the value with increasing interface shock viscosity when transitioning from HTPB to AP phase due to the presence of the HTPB-AP interface phase. This occurs due to the fact that the energy dissipation at the shock front increases with the interface shock viscosity which leads to a decrease in the temperature.

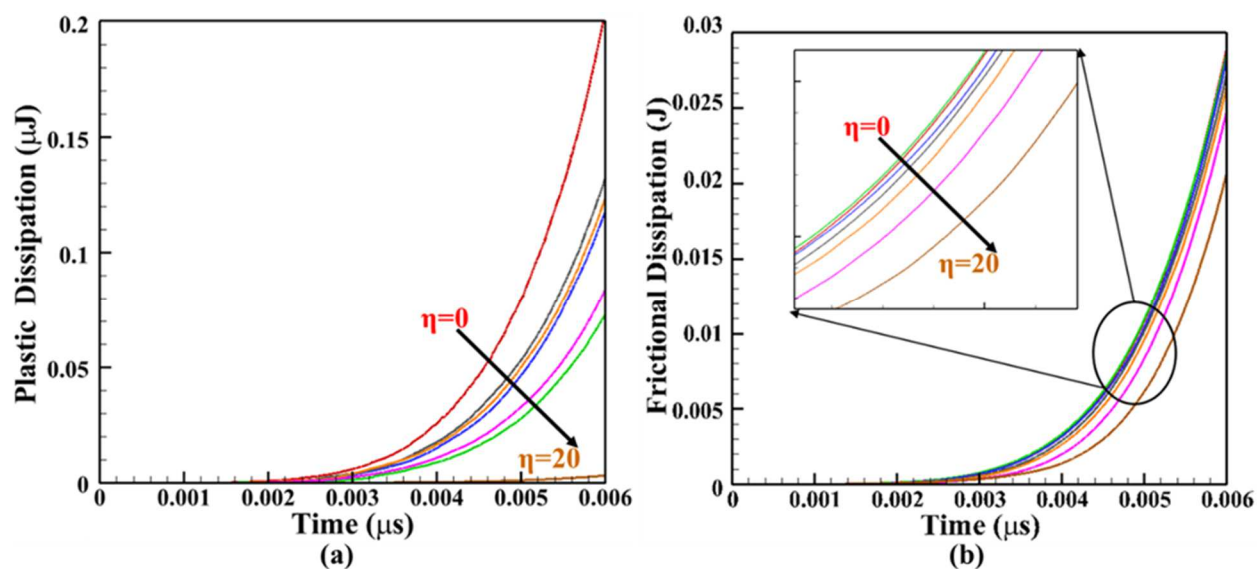


Figure 52 (a) Viscoplastic and (b) frictional energy dissipation history in the HTPB-AP microstructure as a function of interface shock viscosity.

The temperature change in the microstructure is a function of the plastic and frictional heat dissipation as given in Eq. (51). The viscoplastic deformation was observed to have a higher value within the HTPB-AP interface phase and the bulk HTPB near the interface than that in the AP, as was shown in Fig. 50. A plastic dissipation and frictional dissipation energy history as a function of interface shock viscosity is shown in Fig. 52(a) and Fig. 52(b) respectively. As shown in Fig. 52, both energy dissipation decreases with increase in interface viscosity. It has been discussed earlier, [17], that the interface shock viscosity leads to an increase the energy spent at widening the shock front, which leads to a decrease in the heat dissipation and the temperature near the interface.

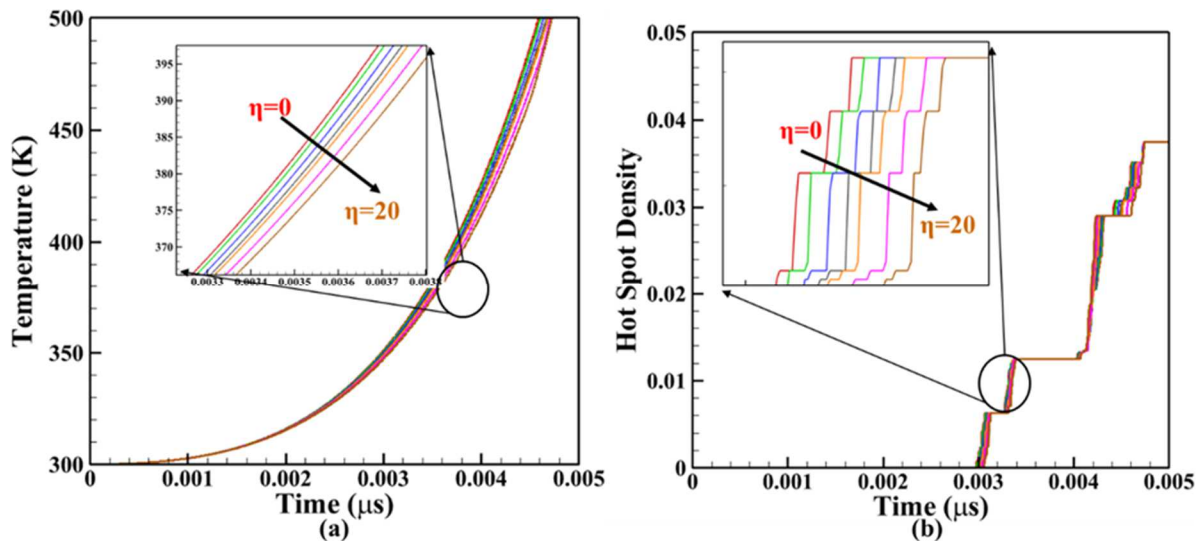


Figure 53 (a) Maximum temperature in the microstructure and (b) the hot-spot density history as a function of interface shock viscosity.

Impact induced temperature may increase to, or greater than, a certain threshold value, within the microstructure, at several position simultaneously. A measure of such local temperature rise can be taken to be equal to the number of elements per unit area within the HTPB-AP microstructure which rises above a threshold temperature value. In this work, this number density

is assumed to be the ‘hot-spot’ density. The maximum temperature that occurs in the HTPB-AP microstructure and the hot-spot density in the corresponding time interval is shown in Fig. 53(a) and Fig. 53(b) respectively. A cut-off temperature was selected for hot-spot density calculation based on the decomposition temperature of HTPB and AP. Decomposition of HTPB binder starts at around 673 K whereas at 513 K a phase change occurs in the AP crystals [55]. In this work the maximum temperature for comparison is taken to be 500 K, which is the temperature after which AP phase change starts to occur [55]. It is observed that the maximum temperature, within the microstructure, decreases by more than 20 K by adding interface shock viscosity in the model. This is in agreement with the effect of shock viscosity obtained by D. J. Benson [2] in a shocked granular HMX. Correspondingly, the hot-spot density in the microstructure also decreases. Fig. 54(a-c) shows the plastic dissipation, the maximum temperature in the microstructure and the hot-spot density as a function interface shock viscosity. It is to be noted that in the current work only 6% area fraction of the microstructure is modeled with HTPB-AP interface phase properties. The stress, dissipation energy and the temperature decrease in the microstructure was found to be significant and in order to predict the temperature increase accurately in EM composites, numerical simulation models should account for the shock viscosity and the effect of interfaces.

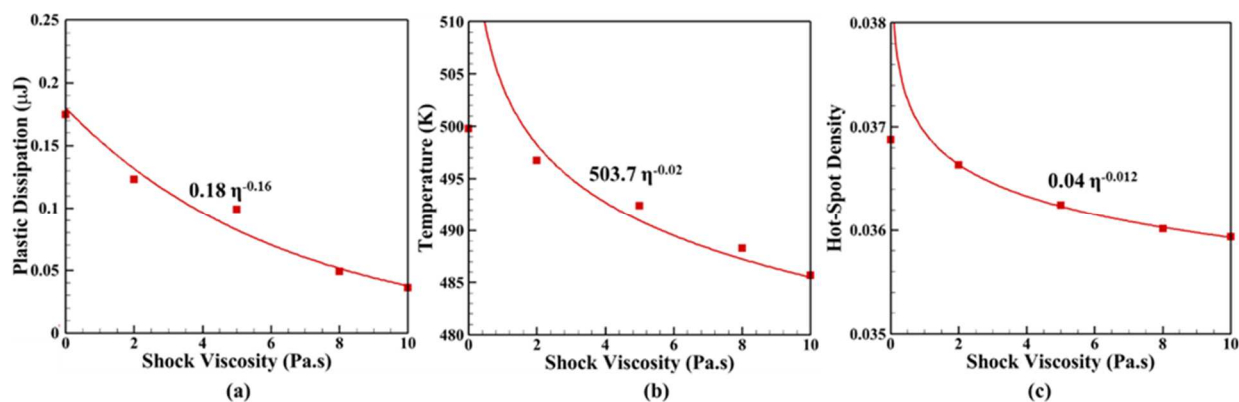


Figure 54 (a) Plastic dissipation energy, (b) maximum temperature and (b) the hot-spot density in the HTPB-AP microstructure at $t = 0.01 \mu\text{s}$ as a function of interface shock viscosity.

3.5 Conclusions

In this work, the effect of interface shock viscosity on the shock induced deformation and local temperature rise behavior of HTPB-AP EM microstructure were studied. It was shown that the interface shock viscosity plays an important role in determining the local temperature rise within the microstructure and should be included in the simulation models. Experimentally obtained mechanical properties such as the strain rate dependent constitutive model, irreversible bilinear cohesive model, interface thermal conductivity and interface shock viscosity were used to model the shock induced deformation behavior using CFEM. Temperature maps showed that the HTPB-AP interfaces, in the energetic material, are the critical positions where the local temperature rise is maximum and are the position where shock initiation may start. Regions with a high density of particles were found to be more susceptible to local temperature rise due to the presence of viscoplastic dissipation, as well as frictional heating. The viscoplastic dissipation were found to be most significant in the HTPB-AP interface phase. The bulk HTPB showed a lower viscoplastic dissipation than the HTPB-AP interface phase but is higher than that in the AP particle. The increase in the interface shock viscosity lead to a decrease in the viscoplastic and frictional dissipation which was caused by the increasing energy dissipation at the shock front. This resulted in a decrease in the maximum temperature achievable within the HTPB-AP microstructure. Finally, a power law relation between viscoplastic energy dissipation, temperature rise, and the density of the local temperature rise as a function of the interface shock viscosity was obtained. The microstructure in this work was idealized as having a 50% AP particles of circular shape having radius from 5 to 15 μm . For a more realistic model of the temperature rise and deformation, a varying shape and density of AP particles needs to be studied.

Acknowledgements

The authors gratefully acknowledge the financial support from the Air Force Office of Scientific Research, Dynamic Materials and Interactions program (Grant No.: FA9550-15-1-0202, Program Manager: Dr. Martin Schmidt).

References

1. Field, J.E., Bourne, N.K., Palmer, S.J.P., and Walley, S.M., *Hot Spot Ignition Mechanism For Explosives and Propellants*. Philosophical Transactions of The Royal Society A: Mathematical, Physical and Engineering Sciences, 1992. **339** (1654): p. 269-283.
2. Benson, D. J. and Conley, P., *Eulerian Finite-Element Simulations of Experimentally Acquired Hmx Microstructures*. Modelling and Simulations in Material Science and Engineering, 1999. **7** (3): P. 333-354.
3. Dienes, J. K., *Frictional Hotspots and Propellant Sensitivity*. Material Research Society Symposium Proceedings, 1984. **24**: p. 373-381.
4. Bennett, Joel G., Haberman, Keith S., Johnson, James N., Asay, Blaine W., and Henson, Bryan F., *A Constitutive Model for The Non Shock Initiation and Mechanical Response of High Explosives*. Journal of Mechanics and Physics of Solids, 1998. **46**(12): p. 2303-2322.
5. Palmer, S.J.P., Field, J.E., and Huntley, J.M., *Deformation, Strengths and Strains to Failure of Polymer Bonded Explosives*. Proceedings of The Royal Society A: Mathematical, Physical and Engineering Science, 1993. **440**(1909): p. 399-419.
6. Rae, P.J., Goldrein, H.T., Palmer, S.J.P., Field, J.E., and Lewis, A.L., *Quasi-Static Studies of The Deformation and Failure of β -HMX Based Polymer Bonded Explosives*. Proceedings of The Royal Society A: Mathematical, Physical and Engineering Science, 2002. **458**(2019): p. 743-762.
7. Prakash C., Verma D., Exner M., Gunduz E., Tomar V., *Strain Rate Dependent Failure of Interfaces Examined via Nanoimpact Experiments*. In: Antoun B. et al. (eds) Challenges in Mechanics of Time Dependent Materials, Volume 2. Conference Proceedings of the Society for Experimental Mechanics Series. Springer, Cham, 2017.
8. Drodge, Daniel R., Proud, William G., Elert, Mark, Furnish, Michael D., Anderson, William W., Proud, William G., and Butler, William T., *The Effects of Particle Size and Separation on PBX Deformation*. Shock Compression of Condensed Matter, 2009. 1195: p. 1381-1384.
9. Prieto, F. E. and Renero, C., *Steady Shock Profile in Solids*. Journal of Applied Physics, 1973. **44**(9): p. 4013-4016.
10. Kanel G.I., Savinykh A.S., Garkushin G.V., Pavlenko A.V., Razorenov S.V., *Shock Wave Rise Time and the Viscosity of Liquids and Solids*. In: Altenbach H., Goldstein R., Murashkin E. (eds) Mechanics for Materials and Technologies. Advanced Structured Materials, Springer, Cham, 2017.
11. Chhabildas, Lalit C. and Asay, James R., *Rise-Time Measurements of Shock Transitions in Aluminum, Copper, and Steel*. Journal Of Applied Physics, 1979. **50**(4): p. 2749-2756.

12. Swegle, J. W. and Grady, D. E. , *Shock Viscosity and The Prediction Of Shock Wave Rise Times*. Journal Of Applied Physics, 1985. **58**(2): p. 692-701.
13. Sheffield, S. A., Gustavsen, R. L., and Anderson, M. U., *Shock Loading Of Porous High Explosives*. In High-Pressure Shock Compression Of Solids IV: Response Of Highly Porous Solids To Shock Loading, Lee Davison, Y. Horie, and Mohsen Shahinpoor, Editors., Springer New York: New York, NY. 1997.
14. Grady, Dennis E., *Structured Shock Waves and The Fourth-Power Law*. Journal of Applied Physics, 2010. **107**(1): p. 013506.
15. Brown, J. L., Vogler, T. J., Grady, D. E., Reinhart, W. D., Chhabildas, L. C., Thornhill, T. F., Elert, Mark, Furnish, Michael D., Chau, Ricky, Holmes, Neil, and Nguyen, Jeffrey, *Dynamic Compaction of Sand*. AIP Conference Proceedings, 2008. 955: p. 1363-1366.
16. Zhuang, Shiming , Ravichandrana, Guruswami , and Grady, Dennis E. , *An Experimental Investigation of Shock Wave Propagation in Periodically Layered Composites*. Journal of The Mechanics and Physics of Solids, 2003. **51**: p. 245-265.
17. Prakash, C., Gunduz , I. Emre, and Tomar, V., *Experimental Interface Shock Viscosity Measurement In An Energetic Material Using Pulse Laser Induced Particle Impact Loading Combined With Mechanical Raman Spectroscopy*. Manuscript Under Preparation, 2018.
18. Prakash, Chandra, Gunduz, I. Emre, Oskay, Caglar, and Tomar, Vikas, *Effect Of Interface Chemistry and Strain Rate on Particle-Matrix Delamination in an Energetic Material*. Engineering Fracture Mechanics, 2018. **191**: p. 46-64.
19. Barua, Ananda and Zhou, Min, *A Lagrangian Framework for Analyzing Microstructural Level Response of Polymer-Bonded Explosives*. Modelling and Simulation in Materials Science and Engineering, 2011. **19**(5): p. 055001.
20. Barua, A., Horie, Y., and Zhou, M., *Microstructural Level Response of Hmx-Estane Polymer-Bonded Explosive Under Effects of Transient Stress Waves*. Proceedings of The Royal Society A: Mathematical, Physical and Engineering Sciences, 2012. **468**(2147): p. 3725-3744.
21. Tan, H., *The Cohesive Law Of Particle/Binder Interfaces in Solid Propellants*. Progress on Propulsion Physics, 2012. **2**: p. 59-66.
22. Tan, H., Liu, C., Huang, Y., and Geubelle, P., *The Cohesive Law for The Particle/Matrix Interfaces in High Explosives*. Journal of The Mechanics and Physics of Solids, 2005. **53**(8): p. 1892-1917.
23. Barua, A., Horie, Y., and Zhou, M., *Energy Localization In Hmx-Estane Polymer-Bonded Explosives During Impact Loading*. Journal of Applied Physics, 2012. **111**(5): o. 054902.

24. Barua, Ananda, Kim, Seok Pum, Horie, Yasuyuki, and Zhou, Min, *Computational Analysis Of Ignition In Heterogeneous Energetic Materials*. Materials Science Forum, 2013. **767**: p. 13-21.
25. Koohbor, B., Ravindran, S., and Kidane, A., *Experimental Study of The Meso-Scale Heterogeneous Deformation Response Of Polymer Composites*. In American Society of Composites-30th Technical Conference, 2015.
26. Ravindran S., Kidane A., *Meso-Scale Deformation Behavior of Polymer Bonded Energetic Material Under Quasi-Static Compression*. In: Ralph C., Silberstein M., Thakre P., Singh R. (eds) Mechanics of Composite and Multi-functional Materials, Volume 7. Conference Proceedings of the Society for Experimental Mechanics Series. Springer, Cham, 2016.
27. Ravindran S., Koohbor B., Kidane A., *Experimental Investigation of Compaction Wave Propagation in Cellular Polymers*. In: Sutton M., Reu P. (eds) International Digital Imaging Correlation Society. Conference Proceedings of the Society for Experimental Mechanics Series. Springer, Cham, 2017.
28. Ravindran S., Tessema A., Kidane A., *Effect of Crystal Density on Dynamic Deformation Behavior of PBX*. In: Antoun B. et al. (eds) Challenges in Mechanics of Time Dependent Materials, Volume 2. Conference Proceedings of the Society for Experimental Mechanics Series. Springer, Cham, 2017.
29. Verma, Devendra, Prakash, Chandra, and Tomar, Vikas, *Interface Mechanics and Its Correlation With Plasticity In Polycrystalline Metals, Polymer Composites, and Natural Materials*. Procedia Engineering, 2017. **173**: p. 1266-1274.
30. Prakash, C., Olokun, Ayotomi M., Gunduz , I. Emre, and Tomar, V., *Interface Mechanical Properties In Energetic Materials Using Nano-Scale Impact Experiment and Nano-Mechanical Raman Spectroscopy*. In Nano-Energetic Materials, Shantanu Bhattacharya, A. K. Aggarwal, T. Rajagopalan, and V. K. Patel, Editors., Springer: Singapore, 2019.
31. Olokun A., Prakash C., Emre Gunduz I., Tomar V., *Interface Chemistry Dependent Mechanical Properties In Energetic Materials Using Nano-Scale Impact Experiment*. In: Kimberley J., Lamberson L., Mates S. (Eds) Dynamic Behavior Of Materials, Volume 1. Conference Proceedings Of The Society For Experimental Mechanics Series. Springer, Cham, 2019.
32. Florczak, Bogdan, *Viscosity Testing Of Htpb Rubber Based Pre-Binders*. Central European Journal Of Energetic Materials, 2014. **11**(4): p. 625-637.
33. Baer, A. D., Keller, J. A., and Ryan, N. W., *Ignition of Ammonium Perchlorate Composite Propellants by Convective heating*. AIAA Journal, 1966. **4**(8): p. 1358-1365.
34. Chaves, Flávio Rodrigues and Góis, José Carlos, *Research on The Specific Heat Capacity of PBX Formulations Based on RDX*. Journal of Aerospace Technology and Management, 2016. **8**(3): p. 352-356.

35. Zhang, Yang, Gan, Ming, and Tomar, Vikas, *Raman Thermometry Based Thermal Conductivity Measurement of Bovine Cortical Bone as a Function of Compressive Stress*. Journal of Nanotechnology in Engineering and Medicine, 2014. **5**(2): p. 021003-021003.
36. Gan, Ming and Tomar, V., *An in Situ Platform for The Investigation of Raman Shift in Micro-Scale Silicon Structures as a Function of Mechanical Stress and Temperature Increase*. Review of Scientific Instruments, 2014. **85**(1): p. 139021-10.
37. Gan, Ming, Samvedi, Vikas, and Tomar, Vikas, *Raman Spectroscopy-Based Investigation of Thermal Conductivity of Stressed Silicon Microcantilevers*. Journal of Thermophysics and Heat Transfer, 2014. **29**(4): p. 845-857.
38. Gan, Ming and Tomar, Vikas, *Surface Stress Variation as a Function Of Applied Compressive Stress and Temperature in Microscale Silicon*. Journal of Applied Physics, 2014. **116**(7): p. 073502.
39. Zhang, Yang, Gan, Ming, and Tomar, Vikas, *Small Scale Thermomechanics in Si With an Account of Surface Stress Measurements*. Mechanics of Composite and Multi-Functional Materials, 2016. **7**(1): p. 247-250.
40. Zhang, Yang, Gan, Ming, and Tomar, V., *In-Situ Combined Sensing of Uniaxial Nanomechanical and Micromechanical Stress With Simultaneous Measurement of Surface Temperature Profiles By Raman Shift in Nanoscale and Microscale Structures*. 2016, Purdue Research Foundation: West Lafayette, IN, US.
41. Périchon, S., Lysenko, V., Remaki, B., Barbier, D., and Champagnon, B., *Measurement of Porous Silicon Thermal Conductivity by Micro-Raman Scattering*. Journal of Applied Physics, 1999. **86**(8): p. 4700-4702.
42. Camacho, G.T. and Ortiz, M., *Computational Modeling of Impact Damage in Brittle Materials*. International Journal of Solids and Structures, 1996. **33**(20-22): p. 2899-2938.
43. Ortiz, M. and Pandolfi, A., *Finite-Deformation Irreversible Cohesive Elements for Three-Dimensional Crack-Propagation Analysis*. International Journal for Numerical Methods in Engineering, 1999. **44**(9): p. 1267-1282.
44. Tan, H., Huang, Y., and Geubelle, P. *An Energy Approach to a Micromechanics Model Accounting for Nonlinear Interface Debonding*. In 41st AIAA/ASME/SAE/ASEE Joint Propulsion Conference & Exhibit. 2005. Tucson, Arizona.
45. Prakash, Chandra, Gunduz, Ibrahim E., and Tomar, Vikas, *Interface Shock Viscosity In Energetic Material Using Cohesive Finite Element Method*. In 2018 AIAA/ASCE/AHS/ASC Structures, Structural Dynamics, and Materials Conference. 2018, American Institute of Aeronautics and Astronautics.
46. Tomar, Vikas, Zhai, Jun, and Zhou, Min, *Bounds for Element Size in a Variable Stiffness Cohesive Finite Element Model*. International Journal for Numerical Methods in Engineering, 2004. **61**(11): p. 1894-1920.

47. Reaugh, John E. and Lee, Edward L., *Shock Hugoniot Behavior Of Mixed Phases With Widely Varying Shock Impedances*. Topical Conference on Shock Compression of Condensed Matter of the American Physical Society 1997.
48. Baek, Hyunil and Park, Kyoungsoo, *Cohesive Frictional-Contact Model for Dynamic Fracture Simulations Under Compression*. International Journal of Solids and Structures, 2018. **144-145**: p. 86-99.
49. Nonnenmacher, M. and Wickramasinghe, H. K., *Scanning Probe Microscopy of Thermal Conductivity and Subsurface Properties*. Applied Physics Letters, 1992. **61**(2): p. 168-170.
50. Hu, Ruize, Prakash, Chandra, Tomar, Vikas, Harr, Michael, Gunduz, Ibrahim Emre, and Oskay, Caglar, *Experimentally-Validated Mesoscale Modeling of The Coupled Mechanical–Thermal Response of AP–HTPB Energetic Material Under Dynamic Loading*. International Journal of Fracture, 2016. **203**(1-2): p. 1-22.
51. Zhang, Jianwei, Zhi, Shijun, and Sun, Bing, *Estimation Of Thermophysical Properties of Solid Propellants Based on Particle Packing Model*. Science China Technological Sciences, 2013. **56**(12): p. 3055-3069.
52. Kubota, N. and Miyazaki, S., *Temperature Sensitivity Of Burning Rate of Ammonium Perchlorate Propellants*. Propellants, Explosives, Pyrotechnics, 1987. **12**: p. 183-187.
53. Garbacz, Andrzej, *Stress Wave Propagation Throughout an Interface: PCC Composites – Concrete Substrate in Repair System*. Architecture Civil Engineering Environment, 2010. **3**(3): p. 35-44.
54. Needleman, A. and Ortiz, M., *Effect of Boundaries and Interfaces on Shear-Band Localization*. International Journal Of Solids and Structures, 1991. **28**(7): p. 859-877.
55. Zhang, Ling-Ke and Zheng, Xiang-Yang, *Experimental Study on Thermal Decomposition Kinetics of Natural Ageing AP/HTPB Base Bleed Composite Propellant*. Defence Technology, 2018. **14**(5): p. 422-425.

CHAPTER 4. CONCLUSION

The main objective of this work has been to perform a combined experimental and computational investigation to study the effect of interface chemical composition on the high strain rate impact induced temperature rise in energetic materials, especially HTPB-AP material. A cohesive finite element method was used to simulate the high strain rate impact behavior of the HTPB-AP EM microstructure. Four different experimental methods were used to measure thermomechanical properties: (1) dynamic impact experimental measurements for fitting a viscoplastic constitutive model of HTPB, AP, and the HTPB-AP interface, (2) in-situ mechanical Raman spectroscopy (MRS) measurements of separation properties for fitting a cohesive zone model, (3) a pulse laser induced particle impact experiment combined with the MRS for measurement of interface shock viscosity, and (4) Raman thermometry experiments for measurement of HTPB, AP, and the HTPB-AP interface thermal conductivity. Two different interface chemical compositions, one with a binding agent Tepanol and other without binding agent, of an HTPB-AP material was used to investigate the mechanical behavior under dynamic loading conditions. The key findings from the present study are summarized below.

1. A nanoscale dynamic impact experiment was used to obtain the constitutive model for bulk HTPB, AP as well as the HTPB-AP interface. A strain rate dependent power law viscoplastic model was fitted to the measured stress, strain and strain rate. It was observed that the interface constitutive behavior can be altered by adding a binding agent. Heat dissipation during impact has a significant effect on material constitutive behavior. However the current experimental setup cannot measure heat dissipation

- directly or indirectly. In this work, effect of heat dissipation on the high-strain rate constitutive model is neglected.
2. The interface delamination experiment under a quasi-static tensile loading combined with an *in-situ* MRS technique was used to obtain a cohesive zone model parameters for the HTPB-AP interface. A tensile test was performed on a single particle edge crack sample with and without binding agent until failure. Crack propagation along the interface was monitored and the corresponding interface cohesive energy was obtained from the load displacement curve.
 3. Local stress near the interface during loading was obtained from MRS. It was observed that the stress near the interface increased by adding a binding agent. The maximum stress at the onset of interface failure was taken to be the interface cohesive strength. It was observed that the interface strength increases with the addition of a binding agent. The cohesive zone model used in this work was assumed to be independent of strain rates. This is because the interface level stress during applied loading is measured using an *in-situ* MRS. The applicability of the current MRS setup is limited by the speed (1 ms/spectra) at which Raman spectra is recorded.
 4. In order to simulate the impact induced temperature rise in an energetic material, a shock viscosity is required in order to take into consideration of all dissipation mechanisms involved. For composites, there are no experimental technique available which can resolve the interface shock behavior explicitly. In this research a novel experimental setup was proposed based on impact simulations done for a single particle HTPB-AP sample. It was found that in order to measure interface level shock initiation,

- a direct interface impact set up was most appropriate. Also, an in-situ stress measurement was required.
5. A laser induced particle impact combined with MRS was used to measure the shock viscosity at an interface. It was shown to be effective in measuring the interface level shock viscosity for both type of samples. Interface shock viscosity of the HTPB-AP interface was observed to be in the range of 2 to 6 Pa.s. A limitation of this experimental setup is that the stress measurement is delayed due to the lower speed of Raman spectra being recorded by the spectrometer, which gives a lower value of stress than the value during shock due to stress relaxation. This results in the measurement of a lower limit of the interface level shock viscosity. However, the interface shock viscosity as a function of strain rate obtained from the current experiment was found to be qualitatively comparable with shock viscosity of different materials found in literature. This information was then used to modify the shock model and was observed that the interface shock wave rise time, which is associated with the dissipation in the material under shock, increases with increasing the shock viscosity.
 6. Thermal conductivity of HTPB-AP interface was obtained using Raman thermometry and was used for the evaluation of temperature change in the overall microstructure. Thermal conductivity for the HTPB-AP interface was found to be equal to 0.16 W/m.K and that for HTPB-AP-Tepanol was equal to 0.175 W.m.K. The thermal conductivity used in this work was assumed to be independent of temperature because the Raman shift vs temperature calibration could not be successfully identified in the higher temperature region. This is due to extremely low signal-to-noise ratio in the recorded Raman spectra for HTPB/AP interface at temperature greater than 75 °C.

7. The experimentally obtained material properties were then used in a cohesive finite element method framework and the model was validated against experimental observation available in literature. A few material model parameters, such as, equation of state, Gruneissen coefficient, heat capacity etc were not available for the HTPB-AP interface phase and were assumed to be an average of the values for HTPB and AP phase. These parameters affect the stress condition, energy dissipation and consequently the temperature rise behavior of the interfaces.
8. Impact induced temperature rise, for an idealized HTPB-AP EM microstructure consisting of circular AP particles, was simulated considering viscoplastic, frictional and shock viscosity induced dissipation. It was observed that the interface shock viscosity leads to a decrease in the viscoplastic dissipation and the maximum temperature within the microstructure. With a 6% area modeled as HTPB-AP interface phase, a decrease of 20 K in the maximum temperature was observed. It was also observed that the hot-spot density decreases with increasing shock viscosity.
9. It was proposed that in order to predict the impact induced deformation behavior and the corresponding temperature rise in an EM microstructure, interface level properties should be considered in the model. Interface shock viscosity was found to be an important parameter that influences the temperature prediction. Interface chemical composition was found to have significant impact on the overall deformation and temperature rise in the EM.
10. The microstructure in this work was a 2-dimensional model and idealized as having a 50% AP particles of circular shape. This presents a few limitation in the prediction of local deformation and temperature rise behavior. One of the main factor that affects the

prediction is the accurate representation of the contact conditions near the interfaces. Particle of different shapes and sizes have different contact force distribution at the surface. This will lead to a stress distribution in and around the particle that is quite different than the one simulated here. This will affect the local deformation and subsequent temperature change behavior around the particle. Shape of the particle also determines the interaction behavior among particles which will generate a local as well as non-local deformation and stress distribution which are significantly different than the one presented in this work. For a more realistic model of the temperature rise and deformation, a varying shape and density of AP particles needs to be studied using a 3-dimensional model.

CHAPTER 5. FUTURE WORK

The present research has brought forth a better understanding of the importance of interfaces in energetic materials. It underscores the importance of special characterization techniques needed for interface level properties measurement. A key finding of the current work has been that the local *in-situ* stress measurement techniques are vastly helpful in understanding the dynamic deformation behavior of composite materials. Some proposed future research is summarized below:

1. A more comprehensive study with several different types of binding agent in varying amount will be undertaken in order to properly quantify the effect of chemical composition.
2. As mentioned in the previous chapter, one of the limitation with the experimentally obtained parameters were that the stress using MRS was not measured in shock duration. In order to understand the mechanisms responsible in high-speed dynamic deformation of composite materials, a local *in-situ* stress measurement technique at high velocity impacts are required. This can be achieved by using a high speed Raman spectroscopy combined with high speed imaging in order to have both stress and deformation data to obtain a more detailed material models.
3. The temperature effect on the material constitutive behavior, specially in the shock induced deformation regime, is important and needs to be included in the constitutive model.
4. The equation of state for the interface phase (e.g. HTPB-AP interface) and the effect of chemical composition needs to be experimentally measured and included in the computational model.

5. A more realistic 3-dimensional microstructure with a varying concentration of different oxidizers and metal particles of varying shape, size and density need to be studied for accurate prediction of deformation and temperature rise.
6. Numerical method based on arbitrary Lagrangian and Eulerian technique should be used to simulate large deformation problems without worrying about the element distortion.

PUBLICATIONS

Book Chapters:

1. **Prakash, C.**, Olokun A., Emre Gunduz I., Tomar V., *Interface Mechanical Properties in Energetic Materials Using Nanoscale Impact Experiment and Nanomechanical Raman Spectroscopy*. In: Bhattacharya S., Agarwal A., Rajagopalan T., Patel V. (eds) Nano-Energetic Materials. Energy, Environment, and Sustainability. Springer, Singapore, 2019.
2. **Prakash, C.**, Verma, D., and Tomar, V., *Dynamic Local vs. Non-Local Properties of Material Interfaces*. Handbook of Nonlocal Continuum Mechanics for Materials and Structures, Springer, 2017.

Refereed International Journal Publications:

1. **Prakash, C.**, Gunduz, I. E., and Tomar, V., (Under preparation), *Effect of Interface Shock Viscosity on the High Strain Rate Induced Temperature Rise in an Energetic Material Analyzed using the Cohesive Finite Element Method*.
2. **Prakash, C.**, Gunduz, I. E., and Tomar, V., (Under preparation), *Experimental Interface Shock Viscosity Measurement in an Energetic Material Using Pulse Laser Induced Particle Impact Loading Combined With Mechanical Raman Spectroscopy*.
3. Olokun, A. M., **Prakash, C.**, Gunduz, I. E., and Tomar, V., (Under preparation), *Microstructure Dependent Failure due to Impact in HTPB/HMX Based Energetic Materials using Cohesive Finite Element Method*.
4. **Prakash, C.**, Gunduz, I. E., Oskay, C., and Tomar, V., *Effect of Interface Chemistry and Strain Rate on Particle-Matrix Delamination in an Energetic Material*. Engineering Fracture Mechanics, 2018. 191: p. 46-64.
5. Verma, D., Biswas, S., **Prakash, C.**, and Tomar, V., *Relating Interface Evolution to Interface Mechanics Based on Interface Properties*. Journal of Materials: The journal of the Minerals, Metals & Materials Society, 2017. 69 (1): p. 30–38.
6. Ruiz, H., **Prakash, C.**, Tomar, V., Harr, M., Gunduz, I. E., and Oskay, C., 2017, *Experimentally-Validated Mesoscale Modeling of The Coupled Mechanical–Thermal Response of AP–HTPB Energetic Material Under Dynamic Loading*. International Journal of Fracture, Vol. 203 (2), p. 277-298.
7. **Prakash, C.**, Lee, H., Alucozai, M., and Tomar, V., 2016, *An Analysis of The Influence of Grain Boundary Strength on Microstructure Dependent Fracture in Polycrystalline Tungsten*. International Journal of Fracture, 2016. 199(1): p. 1-20.

Peer Reviewed Articles In Conference Proceedings:

1. Olokun, A. M., **Prakash, C.**, Gunduz, I. E., and Tomar, V., *Interface Chemistry Dependent Mechanical Properties in Energetic Material using Nano-scale Impact Experiment*. Dynamic Behavior of Materials, 2019. 1: p. 147-152.
2. Zhang, Y., **Prakash, C.**, and Tomar, V. , *Crack Tip Stress Measurement at High Temperature in IN-617 Using Nano-indentation and Nano-mechanical Raman Spectroscopy*. Fracture, Fatigue, Failure and Damage Evolution, 2019. 6: p. 51-56.
3. **Prakash, C.**, Gunduz, I. E., and Tomar, V., *Uncertainty Quantification in Nano-scale Impact in Energetic Materials*. Model Validation and Uncertainty Quantification, 2019. 3: p. 257-263.
4. **Prakash, C.**, Gunduz, I. E., and Tomar, V., *Interface Shock Viscosity in Energetic material using Cohesive Finite Element Method*. 2018 AIAA/ASCE/AHS/ASC Structures, Structural Dynamics, and Materials Conference, AIAA SciTech Forum, (AIAA 2018-1158).
5. **Prakash, C.**, Gunduz, I. E., and Tomar, V., *Effect of Strain Rate and Interface Chemistry on Failure in Energetic Materials*. Fracture, Fatigue, Failure and Damage Evolution, 2017. 7: p. 7-12.
6. **Prakash, C.**, Verma, D., and Tomar, V., *Strain Rate Dependent Failure of Interfaces Examined via Nanoimpact Experiments*. Challenges in Mechanics of Time Dependent Materials, 2017. 2: p. 93-102.
7. Verma, D., **Prakash, C.**, and Tomar, V., *Interface Mechanics and its Correlation with Plasticity in Polycrystalline Metals, Polymer Composites, and Natural Materials*. Procedia Engineering, 2016. 173: p. 1266-1274.

Conference Presentations (Excluding Peer Reviewed Proceedings):

1. Dhiman, A., **Prakash, C.**, and Tomar, V., *Machine Learning Approach For Parameter Identification and Uncertainty Quantification In The Modeling Of Impact Behavior Of Ceramic/Epoxy Composites*. IMAC-XXXVII Conference & Exposition, Orlando, FL, January 28-31, 2019.
2. Olokun, A. M., **Prakash, C.**, Gunduz, I. E., and Tomar, V., *Impact Induced Mechanical Behavior of HTPB/HMX Based Energetic Materials using Cohesive Finite Element Method*. ASME's International Mechanical Engineering Congress and Exposition (IMECE), Pittsburgh, PA, November 9-15, 2018.
3. **Prakash, C.**, Gunduz, I. E., and Tomar, V., *Effect of Interface Chemistry and Interface Thickness on shock behaviour in Energetic Material using Cohesive Finite Element Method*. 13th World Congress on Computational Mechanics, New York City, July 22-27, 2018.
4. **Prakash, C.**, Gunduz, I. E., and Tomar, V., *Effect of Interface Thickness on Impact Induced Delamination Failure in Energetic Material using Cohesive Finite Element Method*. 18th U.S. National Congress for Theoretical and Applied Mechanics, Chicago, Illinois, June 4-9, 2018.

5. **Prakash, C.**, Zhang, X., Olokun, A. M., Gunduz, I. E., Oskay, C., and Tomar, V., *Experimental and Computational Investigations of Interface Chemistry Dependence and Parameter Sensitivity of Dynamic Response and Fracture in Energetic Materials*. Energetic Materials Gordon Research Conference, June 03-June 08, Newry ME, USA, 2018.
6. **Prakash, C.**, Gunduz, I. E., and Tomar, V., *Interface Chemistry and Strain Rate Effect on Fracture in Energetic Material Interfaces*. BSSM 12th International Conference on Advances in Experimental Mechanics, University of Sheffield, Sheffield, UK, 2017.
7. **Prakash, C.**, and Tomar, V., *Interface Chemistry and Strain Rate Effect on Fracture in Energetic Material Interfaces*, MS&T17, Pittsburgh, Pennsylvania, USA, 2017 (**Invited**).
8. Zhang, Y., **Prakash, C.**, and Tomar, V., *In-situ Crack Tip Stress Measurement at High Temperature in IN-617 Using Combined Nano-indentation and Nano-mechanical Raman Spectroscopy*. SEM Annual Conference on Experimental and Applied Mechanics, June 12-15, Indianapolis, IN, 2017.
9. Verma, D., **Prakash, C.**, and Tomar, V., *Interface Mechanical Strength and Elastic Constants Calculations via Nano Impact and Nanomechanical Raman Spectroscopy*. SEM Annual Conference on Experimental and Applied Mechanics, June 12-15, Indianapolis, IN, paper no. 13, 2017.
10. Biswas, S., **Prakash, C.**, and Tomar, V., *Microstructure Evolution and Deformation Behavior of Powder Materials during Field Assisted Sintering Technique*. International Mechanical Engineering Congress and Exposition (IMECE) in Phoenix, Arizona, USA, 2016 (**Invited**).
11. **Prakash, C.**, Gunduz, I. E., and Tomar, V., *Effect of Interface Chemistry on Failure of Energetic Material Examined via Nano-Mechanical Raman Spectroscopy and Cohesive Finite Element Method*. International Mechanical Engineering Congress and Exposition (IMECE) in Phoenix, Arizona, USA, 2016.
12. Verma, D., **Prakash, C.**, and Tomar, V., *Strain Rate Dependent Failure of Interfaces in Glass/Epoxy and Energetic Materials at Nano-Microscale*. International Mechanical Engineering Congress and Exposition (IMECE) in Phoenix, Arizona, USA, 2016.
13. Verma, D., **Prakash, C.**, and Tomar, V., *Interface Impact Experiments and Derivation of Rate Dependent Cohesive Separation Laws*. In Proceedings of ICCM20, July 19-24, Copenhagen, Denmark, 2015 (**Invited**).